Solidification of Al-Cu Eutectic Alloy during Laser Powder Bed Fusion-Learning from and Controlling the Microstructure

---

A Dissertation

Presented to the Faculty of the School of Engineering and Applied Science
University of Virginia

In Partial Fulfillment of the
Requirements for the Degree of
Doctor of Philosophy in Materials Science and Engineering

By

Jonathan M. Skelton
Dec. 7th, 2021

APPROVAL SHEET

This Dissertation is submitted in partial fulfillment of the requirements for the degree of Doctor of Philosophy

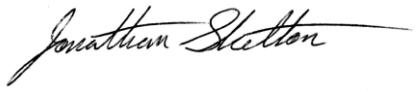

Author

The dissertation has been read and approved by the examining committee:

James M. Fitz-Gerald

Jerrold A. Floro

Xiaodong Li

James M. Howe

Ji Ma

Leonid V. Zhigilei

Accepted for the School of Engineering and Applied Science:

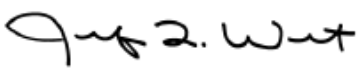

Jennifer L. West, School of Engineering and Applied Science

December 2021

Abstract

The solidification of Al-Cu eutectic alloys can produce a two-phase lamellar microstructure that strongly correlates to the solidification velocity, direction, and composition of the precursor melt. These relationships allow certain manufacturing techniques to control the resulting microstructure, and thus properties, of the Al-Cu system directly from the liquid phase without post processing. For example, at high solidification rates, such as those achieved through laser melting, the eutectic interlamellar spacing can be driven down to sub-micron length scales, increasing the strength of the material by impeding dislocation movement through a high density of interphase interfaces. In terms of processing techniques, laser powder bed fusion (LPBF), a form of additive manufacturing (AM), is perhaps the best positioned to not only control the length scale and orientation of eutectic microstructures, but to also vary these microstructures anywhere *within* the volume of a built part. Furthermore, the eutectic microstructure can be used to elucidate specific solidification phenomena relevant to LPBF, and thus allow for improvements to the processing method. In this dissertation, the processing of the Al-Cu system through LPBF is investigated with a focus around two main ideas: the use of the Al-Cu eutectic microstructure as a recording device for solidification phenomena that occur within the LPBF process, and the use of the LPBF processing parameters to control the eutectic microstructure and mechanical properties of the Al-Cu system.

In the first half of this work, the Al-Cu eutectic microstructure is leveraged to explain certain solidification events that occur in separate aspects of LPBF including: morphology changes within recycled powder feedstock, in situ alloying of elemental particles during laser

melting, and melt pool fluctuations caused by internal and external sources. Through these studies, a mechanism by which laser irradiated powder deforms within LPBF was deduced, with possible applications to improving recycled feedstock powder. It is shown here, through characterization of individual particles both before and after laser irradiation, how dent and rift morphologies develop from buckling that occurs in the oxide shell as particle melt, cool and re-solidify. The eutectic microstructure was utilized to record the thermal history of the particles, as well as the solidification direction, both of which were correlated to the changes in morphology. Elemental mixing during in situ alloying was also studied here, with the eutectic microstructure being used to measure the degree of mixing that occurred between different elemental powder blends. The degree of mixing during the LPBF process was measured qualitatively by Z-contrast from backscatter electron microscopy (BSE) of hypo- and hypereutectic microstructures which formed in regions that where fluctuations in the eutectic composition occurred within the melt. The percentage of these off eutectic regions were then compared to both the laser parameters and the size distribution of the elemental components of the powder blends used to make the samples. This study aided in the development of in situ alloying during LPBF which could help greatly expand the number of alloys used within this processing technique.

In the second half of this work, relationships between the processing parameters, microstructure, and mechanical properties of this eutectic system were studied. A clear correlation between the laser scan velocity and the hardness of the system was shown, even after the lamellar microstructure began to break down at rapid solidification velocities to a fine dendritic microstructure, and eventually to a metastable solid-solution phase. A peak hardness was found at a scan velocity of 200 mm/s which produced a fine lamellar microstructure with an estimated flow strength of 1.27 GPa, as compared with the coarsest lamellar microstructure (scan

velocity of 5 mm/s) which gave an estimated flow strength of 0.83 GPa. Dendritic microstructures (scan velocities from 300-1100 mm/s) and the metastable solid-solution phase (2000 to 3000 mm/s) gave estimated flow strength values of 1.19- 1.01 GPa and 0.93 to 0.9 GPa respectively. Melt pool boundaries were also characterized in terms of hardness and microstructure and were found to have a lower estimated flow strength by up to 160 MPa. An investigation was made focused on how coupled growth occurs at the melt pool boundaries within LPBF, and a solidification mechanism for the two-phase system that produced the specific microstructure observed at the interface was proposed. Samples were analyzed in this work through an array of characterization techniques including Vickers hardness, optical and scanning electron microscopy (SEM), energy dispersive spectroscopy (EDS), TKD, X-ray fluorescence (XRF), dual-beam focused ion beam (DB-FIB) sectioning, transmission electron microscopy (TEM), and scanning transmission electron microscopy (STEM). The results of this work demonstrate how multiple microstructures with controlled mechanical properties can be printed by LPBF processing, setting the groundwork for a rational design of gradient or hierarchical microstructures.

It is the glory of God to conceal a thing: but the honor of kings *is* to search out a matter.

-Proverbs 25:2

Acknowledgements

When I think about all of the many things that had to take place for this work to be accomplished, I am humbled, and give glory to God for orchestrating the events that led me here, for providing me with the opportunity to perform research, and most of all for bringing the many people into my life that have helped every step along the way. To begin, I could not have asked for better advisers during my time here, nor men more patient and considerate to work for. Both Prof. Jim Fitz-Gerald and Prof. Jerry Floro have shown me what it looks like to be a world class researcher, a devoted and caring teacher, and a citizen leader, each in their own unique way. I have seen firsthand how Prof. Jim Fitz-Gerald has opened his office door to any student who needs to talk about classes or life, all the while building an undergraduate MSE program, managing research projects, teaching classes, and running into burning buildings as a volunteer fire fighter. Similarly, I have witnessed Prof. Jerry Floro's genuine enthusiasm for science and teaching, and how this has motivated the time and effort he pours into his classes, as well as the outreach to local schools that he spearheads through Nanodays, and even the long scientific discussions he enthusiastically participates in when his graduate students present him with random natural phenomena. Observing these actions have left lasting impressions on me and I hope to emulate them in my own way as I leave here. I owe both of these men a great deal and have a deep gratitude for all of the time and effort they have spent helping me become a better researcher, writer, and teacher.

Beyond my advisers, I would like to thank some of the other professors in the department that I've had the privilege to take a class from, including: Prof. Opila, Prof. Agnew, Prof. Howe, Prof. Reinke, and Prof. Sofa. I have seen the devotion to pedagogy each one of these professors have displayed in the classroom, and I am grateful to have been one of their students. I would here also like to thank Prof. Ma, for allowing me to co-teach a class with him and to learn about

everything that goes into course design and lesson preparation. The experience has given me even more appreciation for professors, and has helped fueled my desire teach in the future.

In terms of the work performed here, it would not have been possible without funding from the National Science Foundation. The NSF, through the tax payers of our country, have paid for all the research I've had the honor to perform, and for my degree as a whole. I recognize some of the responsibility that comes with this and hope to use my degree wisely and for the betterment of others.

I would like to thank my committee members, Prof. Howe, Prof. Zhigilei, Prof. Ma, and Prof. Li, for being quick to answer any question I had on my research, and for taking the time to examine my work and providing feedback from their wealth of expertise. I would also like to thank both the past and present admin of the MSE department, for all of the help with receipts, flights, paperwork, payment, and random questions they have helped me with through the years. A special thanks Barry Baber, Jerry Weaver and Ig Jakovac for helping me overcome many technical road blocks. The staff at the NMCF have been vital to the work performed here and I am very grateful for all of the training, discussions, and technical support they have provided. Specifically I would like to thank Cathy Dukes, for all of her help attempting to resurrect our XPS, to Helge Heinrich, for training me on the FIB and TEM, and to Richard White for helping out every time I knocked on his office door with a new problem.

For those who have had a direct hand in this work, I would like to thank Wenhao Lin for all of the many hours he has volunteered towards this project, and for always being willing to help with experiments, even the random ones that did not always work. I would like to thank Eli Sullivan for our discussions about eutectic solidification, both at the office and at Starbucks. Connor Headley helped with this project substantially in its early stages, in the construction of

"spike", and "the ring of fire", and I am grateful to have worked with him and been around long enough to see him begin his own project (thankfully not with magnets). Alex Wang and Gabe Lu have also contributed significantly to this project, Alex with the eutectic banding work, and Gabe with the work on the bulk line scans. They are the second wave of undergraduate researchers I have had the privilege to work with and are both well on their way to becoming great engineers and scientists. I would here also like to thank Qiyuan Lin for the great conversations, about Socrates, Quantum mechanics, and our actual research projects.

I would like to thank the many people I have met in Charlottesville who have helped me in different ways during my time here, and thus indirectly with this project. This include the members of my community group and my church family at CCC who have reminded me where my hope lies, even in times of stress. I would like to thank my neighbors, Ghassan and Rahmah, for making me a part of their family and for keeping me well fed throughout the past few years, and my neighbor Tony, for his good advice. I would like to thank Torrance for the many chess games, cups of tea and beers I owe him, and the whole Wirt family, and their long history of opening their home up to me.

I have been greatly helped by all of my lab mates, both new and old, through long conversations about research questions, providing help with experiments, and having my back in more ways than I can count. Specifically I would like to thank past members, Dr. Mike Melia, John Xia, Bryan Koscielny, and Libby Urig, as well as Dr. Naiming Liu and Dr. Wade Jensen, for helping me in the early stages of this research. I am grateful to the present members Adrian Savovici, Eli Sullivan for always being willing to let me bounce ideas off of them, and to the new members Hossain Sonjib and Haobo Wang, for taking over many of the lab tasks. I especially

would like to thank Cecilia Mulvaney for all of the edifying discussions and freshly baked pastries, and Will Moffat for always being around through thick and thin.

I am grateful to all of my peers and friends I have had the honor to know and work with. There are too many to name, but all of those who I've talked with through the years, sat around bonfires with, and even quarantined with; I am deeply grateful for your friendship and encouragement through the years. Lastly, I have been blessed with an incredible family, without whom I would not be where I am today. Their love and support have been continuous throughout many highs and lows in my life and it is the foundation on which any accomplishment I may achieve is built.

List of Figures

List of Terms and Symbols

AM: Additive manufacturing

LPBF: Laser powder bed fusion

JH: Jackson and Hunt model

λ: Interlamellar spacing

ΔT_o: Undercooling

ΔH: Change in enthalpy

v_s: Solidification velocity

D: Diffusion constant

k_n: nth constant

TMK: Trivedi, Magnin and Kurz model

P: Peclet number

P_{eff}: Effective laser power

v_b: Scan velocity

σ_b: Beam width

d: Powder thickness

VED: Volume energy density

DED: Directed energy deposition

ITO: Indium Tin Oxide

SEM: Scanning electron microscope

EDS: Energy dispersive X-ray spectroscopy

XRF: X-ray fluorescence

HWHM: Half width half max

SE: Secondary electrons

BSE: Backscattered electrons

EBSD: Electron backscattered diffraction

FIB: Focused ion beam

ETD: Everhart-Thornley detector

CBS: Concentric backscatter detector

ICE: Ion conversion and electron detector

TKD: Transmission kikuchi diffraction

d_{avg}: Average diagonal length of Vickers hardness indent

HV: Vickers hardness number

F: Applied force

A_s: Surface area of Vickers indent

TEM: Transmission electron microscope

STEM: Scanning transmission electron microscope

HAADF: High angle annular dark-field

P_c: Critical buckling pressure

E: Young's modulus

v: Poisson's number

r_s: Radius of shell

ε_{rr}: Radial strain

ΔP: Change in pressure

$\Delta\alpha$: Change in coefficient of thermal expansion

ΔT: Change in temperature

COTS: Commercial off the shelf

FF: Flow factor

MPS: Major principle stress

UYS: Unconfined yield strength

ρ: Density

R: Solidification rate (same as v_s)

G: Thermal gradient

BD: Build direction

SD: Scan direction

TD: Translation direction

HAZ: Heat affected zone

MP: Melt pool

MPB: Melt pool boundary

SAD: Selected area diffraction

SAA: Selected area aperture

Table of Contents

Significant Results

- A mechanism of powder deformation not previously discussed in the literature was observed within Al and Al-Cu powder after laser irradiation during the LPBF process and was shown to be the result of particles melting and resolidifying within their respective oxide shells
- Particle size distribution and laser processing parameters are directly related to the degree of mixing that occurs during in situ alloying of elemental Al and Cu powder blends
- Eutectic banding was observed in laser processed sample made at slower scan velocities (<130 mm/s), and was shown to correspond with ripple formations and to fluctuations in the melt pool dimensions
- Laser scan velocity was shown to correlate directly with the solidification velocity, and thus the interlamellar spacing, of the LPBF processed Al-Cu eutectic samples according to the Jackson and Hunt model, while laser power had no effect on the interlamellar spacing
- The width of eutectic colonies in LPBF processed samples were shown to have no correlation with either the laser velocity or the laser power, varying between 1-3 μm in size
- A peak hardness was shown to occur at a scan velocity of 200 mm/s in laser processed eutectic samples with an approximate flow strength of 1.27 GPa due to a fine lamellar spacing, while higher scan velocities showed a trend in decreasing hardness similar to an inverse Hall-Petch relationship
- Epitaxial growth of the θ-phase was shown to occur at the melt pool boundary of LPBF processed samples, while the α-phase spherical micron size particles of various orientations directly above the solid-liquid interface before returning to a regular lamellar microstructure outside of the MP coarse region

Chapter 1 : Introduction

1.1: Motivation

Eutectic alloys have a wide variety of applications in industry due to their low melting point, high density of interfaces, and ability to self-organize through coupled growth directly from the liquid. These unique traits have been used in functional materials ranging from enhanced phonon scattering in thermoelectrics, to creating nanostructured motifs as templates for metamaterials [1,2,3,4,5]. By decreasing the interlamellar spacing to nanoscale dimensions, a higher density of these interfaces may be achieved, and drastic enhancements in the desired properties stand to be gained [6]. Thus many, technologies are positioned to benefit from nanostructured eutectic materials, but obstacles must be overcome to create a bulk component with nanoscale eutectic microstructure, the most prominent being the fast cooling that is required. Laser irradiation has been employed to create localized melting in eutectic samples which then rapidly solidify due to high thermal conductivity of the surrounding bulk, but this process remains only a surface treatment due to limitations of the melt pool depth [7,8]. With the advent of additive manufacturing (AM), specifically laser powder-bed fusion (LPBF), bulk materials can be processed at rapid solidification rates by melting layers of powder through a laser scanned at high velocities [9,10]. Through this process it has been shown that nanoscale microstructures can be achieved as a result of laser induced rapid solidification, yet little work has been published focused on utilizing LPBF as a way to decrease the interlamllar spacing of eutectic alloys [11,12,13].

Perhaps the most direct application of bulk materials with nanoscale lamellar microstructures may be found within the industry of high strength alloys. It has been shown that there is a direct correlation between the width of the lamellar spacing of eutectic alloys and their

mechanical properties due to the increase in the density of two-phase interfaces that impede dislocation motion [14,15]. Yet, apart from steel, precipitate hardening has become the dominating strengthening mechanism for most high strength alloys due to the degree of control over which secondary, often metastable, phases can be nucleated and grown using heat treatments [16,17]. Although the length scale of precipitates in these alloys can be tailored to maximize dislocation impediment, the nucleation process will remain stochastic, causing an even distribution of precipitates within the matrix. Thus, any anisotropy in the mechanical properties of precipitate hardened alloys that occurs as a result of the nucleated secondary phases will be determined by the preferred crystallographic planes on which these precipitates grow [18,19]. In contrast, microstructures formed in eutectic alloys are grown directly from the liquid phase, causing systems that form lamellar microstructures to be oriented in the direction of the solidification front [20]. This ability to control the direction, and thus the anisotropy, of lamellar eutectic alloys provides an advantage over precipitate hardened alloys, especially in processing methods such as LPBF which provides in-plane control of the solidification direction within each layer of a build. The implementation of eutectic alloys as a high strength material thus hinges on the development and understanding of processing techniques that can both directionally solidify and minimize the lamellar spacing of these alloys so that their mechanical properties rival those of modern precipitate hardened alloys.

1.2: Background

1.2.1: Eutectic Solidification

The study of eutectic solidification can be said to have first began with the work of Fredrick Guthrie who noted in 1875 that certain compositions of alloys had a depression in their melting

points, and thus later named them "eutaxia" from the Greek "to melt well" [21]. Since then a thorough understanding of how these alloys solidify has slowly developed, revealing other characteristic traits besides just a low melting point [22]. It was found through highly controlled processing methods such as the Bridgman-Stockbarger technique that the various two-phase eutectic microstructures could be modified by adjusting the solidification rate and the temperature gradient at the solid-liquid interface [23]. Through the research of Winegard, et al., it was shown that the interlamellar spacing of the Pb-Sn eutectic system decreased as the solidification velocity increased [24]. Impurity concentration was also found to strongly influence the microstructure of these alloys, with higher impurity concentrations causing the solid-liquid interface to become unstable and form cell like colonies of eutectic structures [25,26]. Zimmermann, et al., later showed through the use of rapid laser scanning techniques, that the interlamellar spacing of the Al-Cu eutectic alloy could be reduced to the nanoscale, and that at higher scan speeds, the microstructure could be changed completely to a dendritic or metastable solid solution [8].

The modern understanding of directional eutectic solidification, based on the model created by Jackson and Hunt (JH), describes the interlamellar spacing as being dependent on the interfacial energy produced by the coupled growth of the two-phase system, and the diffusion rate of the solute in liquid near the solid-liquid interface [27,28]. The first part of this relation can be described by the following

$$\lambda = \frac{2\gamma_{\alpha\beta} V_m T_E}{\Delta H \, \Delta T_0},$$

Eq. 1-1

where the minimum interlamellar spacing (λ) is determined by how much the liquid of the system has been undercooled (ΔT_0), along with other properties of the system such as the interfacial energy produced by the two-phase growth ($\gamma_{\alpha\beta}$), the molar volume of the eutectic (V_m), the eutectic temperature (T_E), and the change in enthalpy due to solidification (ΔH). The second part of the relation, giving the dependence of the interlamellar spacing on the diffusion rate of the solute near the solidification front, is shown by

$$v_0 = \frac{kD\Delta T_0}{2\lambda}$$

Eq. 1-2

This relationship shows how the solidification velocity (v_0) is related to the undercooling and interlamellar spacing, along with the diffusion constant of the system (D) and a proportionality constant (k). Through these two equations it can be shown that

$$v_0\lambda^2 = k_1,$$

Eq. 1-3

and,

$$\frac{v_0}{\Delta T_0} = k_2,$$

Eq. 1-4

where k_1 and k_2 are constants dependent on the material system. Thus, the solidification velocity and the undercooling can be determined from the observed interlamellar spacing of a eutectic system. This has been shown repeatedly through experiments with both lamellar and rod eutectic growth during directional solidification of systems with non-faceting interfaces [8,29]. Strictly speaking, this analysis applies to steady-state directional solidification only. The JH model begins to break down though at higher solidification velocities, where the diffusion distance of the solute is shortened due to the rapidly moving solidification front, and a much higher undercooling occurs in the liquid [30,31].

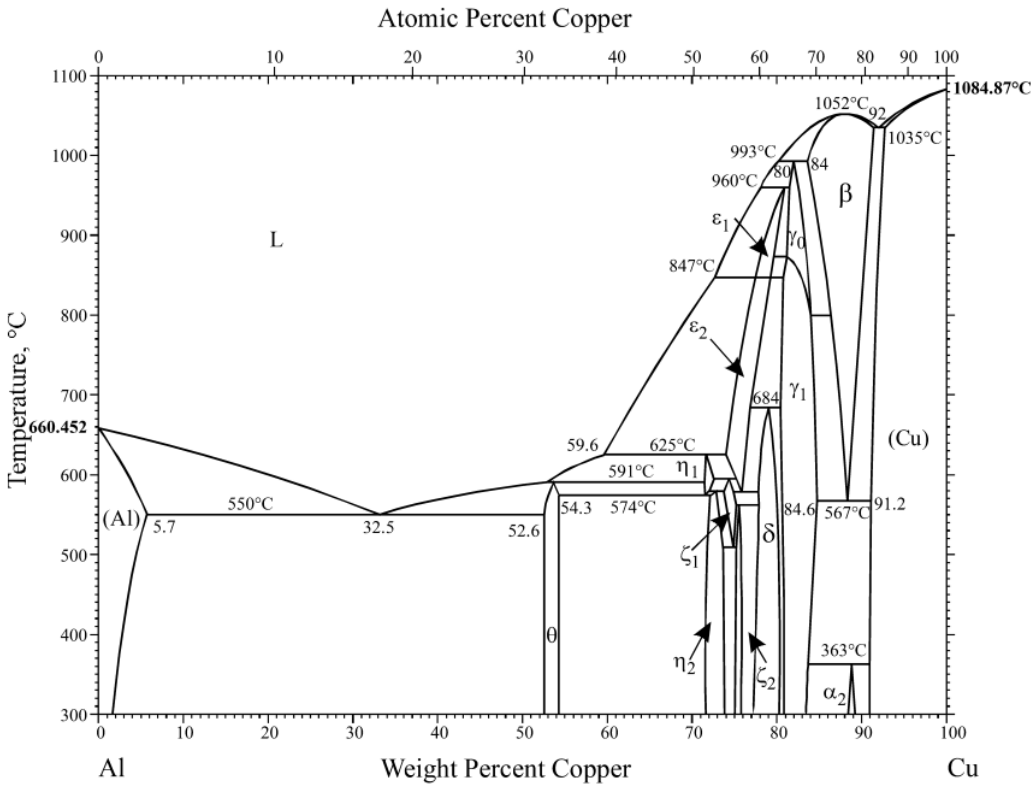

Figure 1-1: Al-Cu phase diagram with the eutectic point at 32.5wt%Cu 32.

The Al-Cu eutectic system has been particularly well studied in the field of solidification as a model eutectic due to the regular lamellar microstructure that forms at moderate solidification velocities [23]. The phase diagram of Al-Cu can be seen below in ***Figure 1-1*** as it exists in thermodynamic equilibrium [32]. Yet while this phase diagram shows what phases should be present at a given composition and temperature, it does not provide any information of how the microstructure will form during solidification. The coupled growth of this system produces 57% θ-phase and 43% α-phase at temperatures close to equilibrium, while at higher solidification velocities the solubility of Cu in the α-phase increases, causing a shift in the phase fraction [33]. The θ-phase (Al_2Cu) consists of a tetragonal crystal structure in the I4/mcm space group, while the α-phase is the Al FCC solid solution phase [34]. Because of the difference in crystal structures, this

system is often categorized as a faceted/non-faceted eutectic or as a ductile matrix-brittle lamellae [35].

1.2.2: Rapid Solidification of Eutectic Alloys

Through the work of Trivedi, Magnin and Kurz (TMK), it was shown that the Jackson and Hunt model deviated from experimental results when

$$p = \frac{v_0 \lambda}{2D} \geq 1,$$

Eq. 1-5

where (p) is defined as the Peclet number [36]. The ensuing TMK model thus predicted that at Peclet numbers greater than 1 the relation between the interlamellar spacing and undercooling of the system is influenced by factors such as the slope of the liquidus lines of the system, the interfacial energies of the liquid and solid phases, and the shape of those interfaces. Thus, each system diverges differently from the JH model at rapid solidification velocities, with predicted physical limits to the length scale capable in many systems existing in the tens of nanometers range. The range of solidification velocities that transition from the JH model to the TMK model have been explored experimentally in the Al-Cu system by Gill and Kurz [37]. As the lamellar spacing in this system was driven to its minimum through rapid solidification, it was shown that instabilities occur in the lamellar microstructure, which eventually would lead to a dendritic microstructure, and at even higher solidification rates, a metastable solid solution [31].

Thus a variety of microstructures can be achieved at various solidification rates even at a constant composition. ***Figure 1-2*** shows the experimentally determined boundaries of these microstructural transitions, and how they change with both composition and solidification rate. Microstructure maps such as this are necessary to understand the general processing parameters

needed to achieve certain microstructures within a material, specifically in the case of eutectic systems where the two-phase microstructure grows directly from the liquid.

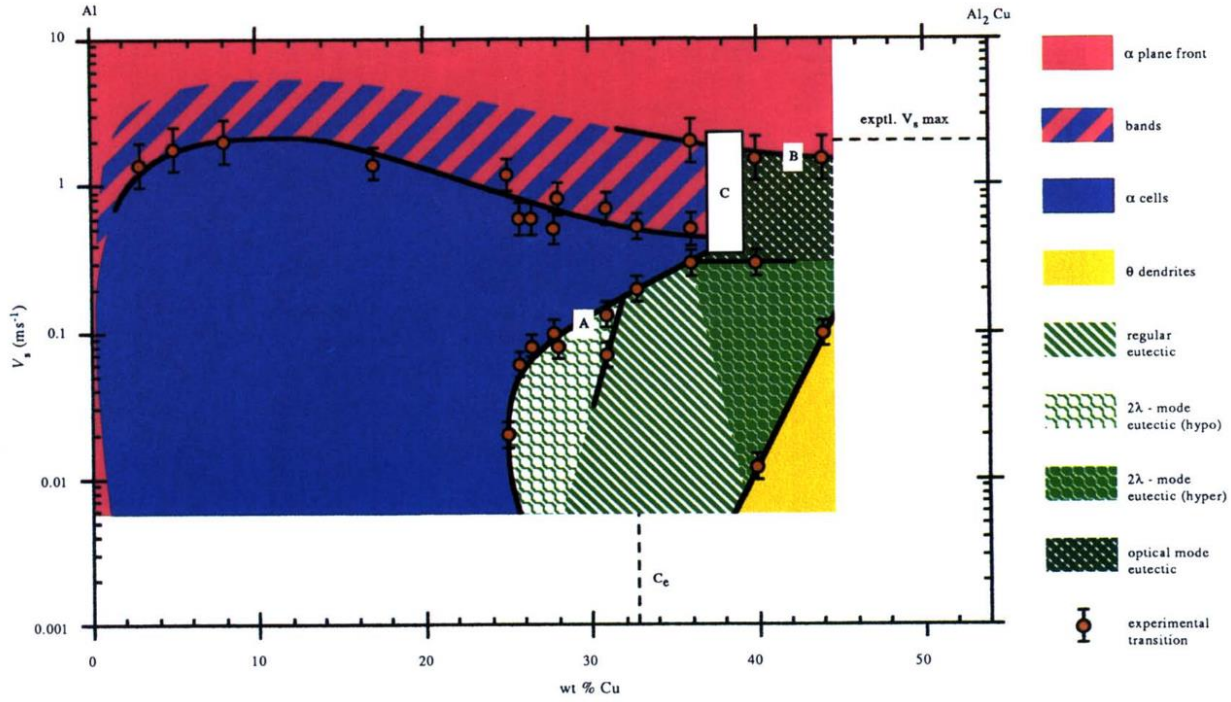

Figure 1-2: Microstructure selection map of the Al-Cu system showing the various microstructures that can form depending on the Cu concentration and the solidification rate [37].

1.2.3: Laser powder bed fusion

Any form of bottom up design where a component is built through sequentially added layers of material can be described as being built through an AM process. Within this field, LPBF has been found to be one of the more versatile techniques, being able to build parts out of a wide range of materials [38,39,40]. Spears, et al., define 50 key parameters in the LPBF method that will determine the outcome of the build, with many being controllable by the user, and the rest being predefined by the selected material properties or machine capabilities.[41] The most influential parameters on the microstructure as well as overall density of the build are those that control the thermal input to the material. Many studies thus use an energy density equation as given below

$$VED = \frac{P_{eff}}{v_b \cdot \sigma_b \cdot d},$$

Eq. 1-6

where the effective laser power (P_{eff}), the laser scan velocity (v_b), the beam width (σ_b), and the powder thickness (d) are related to give the total volumetric energy density of the build (VED) in J/mm^3 [42]. This equation gives a working understanding on how to maintain a constant energy input in a build while varying other parameters. This value cannot be used alone though, as parameters with the same VED may give very different microstructures of a material depending on what the specific values of the laser power and scan velocity are used [43]. Even the melt pool geometry or the melt depth cannot be estimated by the VED alone as the laser power is often the dominate factor that changes these properties, and this too depends on the absorption of the powder feedstock [44]. Increase in the laser power will often not give linear relationships to the melt pool dimensions, especially as the melt pool transitions from conduction to keyholing modes, where the depth of the melt pool drastically increases. Along with this, increases in velocity will give drastically different microstructures as discussed above, even if the power is varied to keep the same total volume energy density [45]. Thus, while VED can be used as a general guide, each individual parameter should also be carefully considered and reported so that information is not lost.

The LPBF technique is specifically well suited to process materials at a variety of solidification rates due to both the large range of power and scan velocities that are available within this method. Because of this, precise control over the microstructure and properties of a built part can be gained through careful selection of processing parameters. This is specifically true when the material being processed does not need to undergo post heat treatments to achieve

the desired microstructure and properties. For example, while precipitant hardened alloys would need post processing after LPBF to form the desired microstructure, eutectic alloys could theoretically be processed directly from the additive process. With this, scan strategies could also be used to control the directional solidification of the eutectic microstructure, allowing anisotropic properties to be engineered within the built material much in the same way crystal texture is currently being controlled within LPBF[46]. In comparison, other techniques such as direct energy deposition (DED) could also control the direction of the solidification through control of the melt pool, but because of the average size of the melt pool in this process, it would be more likely that nucleation events would occur and produce grains with randomly oriented microstructures. On the other hand, because LPBF creates a smaller melt pool, this in turn causes there to be more melt pool boundaries with the built material, making the need to characterize and understand these interfaces even more important.

1.3: Overview of work

The solidification of Al-Cu eutectic alloy through LPBF processing is studied in this dissertation with a specific focus on the relation between the laser parameters used and the microstructures formed. This work can be divided into two main sections:

1) The use of the Al-Cu eutectic microstructure as a recording device for solidification events that occur during the LPBF process.
2) The use of the LPBF processing parameters to control the eutectic microstructure and mechanical properties of the Al-Cu system.

Thus the well-studied relationship between the eutectic microstructure and the solidification velocity of this system is used here as a two edge sword, both providing information about the LPBF process, and allowing the microstructure to be fine-tuned by the laser parameters. The first part of the work will discuss three main aspects of the LPBF process where the eutectic microstructure was used to better understand what was occurring in the system. These include: morphology changes in recycled powder feed stock; variations in composition that occur when samples are processed through in situ alloying; and the effects of melt pool motion on the solidification velocity.

The second half of this work then discusses the relationship between the processing parameters and the various eutectic microstructures formed, as well as the hardness values obtained from these microstructures. The decrease in the mechanical properties is shown as the lamellar microstructure breaks down at rapid solidification velocities to a dendritic microstructure and eventually a solid-solution phase. The mechanical properties at the melt pool boundaries were also characterized and compared to the properties of the bulk at various laser scan velocities. Finally, an investigation of how the lamellar eutectic microstructure forms across the melt pool boundaries during LPBF processing is investigated, and from the results a mechanism is proposed.

The last chapter of this work gives a summation of the contributions that have been made as well as provides a brief discussion on where future work may be pursued. Specifically, the ability to produce a range of microstructures and mechanical properties within a single eutectic composition is discussed in terms of creating functional gradient materials, as well as internal geometries and hierarchical structures.

Chapter 2 : Experimental and Characterization Methods

2.1: Processing Methods

In general, the experiments performed in this work can be broken into three categories: laser irradiation of single powder layers, line scans performed in bulk samples, and irradiation of multiple powder layers consolidated into a bulk material through LPBF. The first two types of experiments helped provide a simplified system so that the process and the samples produced by LPBF can be better understood, and could be compared and contrasted with samples built through the actual LPBF process. The preparation and the material used for each of these experiments are discussed below.

2.1.1: Powder processing

2.1.1.1: Powder morphology experiments

Gas-atomized Al-33wt%Cu and elemental Al (99.8 wt%) powders were obtained from Valimet Inc. with a mean particle diameter of d_{50} = 20 µm and d_{50} = 9 µm, respectively. Powder samples were prepared by drop casting a 0.5wt% solution of particles in aqueous solution onto a substrate and then dried within a desiccator for over 24 hrs. Substrates used for these experiments included sapphire slides as well as glass slides, with particles being stamped onto carbon tape after laser irradiation for scanning electron microscopy (SEM) characterization. Glass slides coated with indium tin oxide (ITO) were also used to promote electrical conductivity for improved SEM imaging in experiments that characterized specific particles both before and after laser irradiation. To better observe changes in laser irradiated particles, the Al-Cu eutectic powder was annealed in a box furnace (Thermolyne 48000) at 450 °C for 2 hours in order to obtain a uniformly coarse, two-phase microstructure (Figure 3.1). Samples in these experiments

were irradiated with all three laser systems (as discussed in section 2.1.4) to better understand how the morphology of the particles changed with different irradiation sources and at what power or fluence the oxide shell ruptured. A select few of these experiments were performed within an Ar environment to reduce the rate at which the oxide shell reformed on the particles during thermal expansion. For the Excimer system, this included setting the sample within a vacuum chamber, pumping down to 10^{-4} Torr and then backfilling with Ar to a pressure of 1 Torr, before irradiating the sample through a UV transparent window. For powder samples irradiated within LPBF system, Ar was flushed into the chamber to achieve oxygen concentration of less than 1000 ppm. For all other experiments, powder samples were irradiated in an air ambient.

2.1.1.2: Powder blend preparation

To create powder blends, additional Al and Cu gas atomized powders were purchased from Valimet Inc. (Cu-1, Al-1, and Al-2 as shown in **Table 2-1**) and Thermo Scientific (Cu-2) at four different size distributions. A pre-alloyed Al-33wt%Cu powder, also obtained from Valimet, was used as a control, providing the best-case scenario of mixing in built samples. The elemental feedstock powders were characterized using an FEI Quanta 650 field emission SEM and the composition of the elemental particles were confirmed using energy-dispersive X-ray spectroscopy (EDS). Size distributions were calculated using ImageJ software to detect and measure the areas of the particles within the micrographs. Over 3,000 particles from each of the four elemental feedstock powders were imaged and measured, in accordance with other studies that used this same particle analysis approach [47,48]. Feedstock powders were then combined in four different binary blends, with both Al and Cu powder being weighed out at the eutectic ratio,

and then mechanically mixed for two hours. Dry mixing was performed within a stainless-steel container using a SPEX 8000M mill in ambient atmosphere and pressure. No balls were used during the mixing process to avoid deformation of the powder. **Table 2-1** shows the four different blends of powders and the d_{50} of the elemental feedstock powders. Rheology data of the powder blends was obtained from a Freeman FT4 powder rheometer directly after drying under Ar for over 24 hours to reduce humidity.

Table 2-1: All four combinations of the elemental feed stock powder, where each blend made Al-33wt%Cu.

Elemental Powder (d_{50})	**Cu-1 (2 µm)**	**Cu-2 (6 µm)**
Al-1 (9 µm)	Blend 1	Blend 2
Al-2 (30 µm)	Blend 3	Blend 4

2.1.2: Bulk Sample

Al and Cu shot were purchased from Thermo Fisher Scientific both at a purity greater than 99.9wt% and weighed out to the eutectic composition. The Al and Cu shot were then placed in an alumina crucible and heated with an oxy-hydrogen torch in ambient air. Sample was stirred in between heating with a graphite rod to ensure mixing of the elemental components. After heating three times, molten metal was poured into a graphite mold and allowed to air cool. Bulk sample was then characterized using X-ray fluorescence (XRF) to ensure the composition was at the eutectic ratio after casting. The surface of the bulk sample was then mechanically ground and polished to 600 grit. Line scans were performed within LPBF system under an inert Ar environment, with the direction of the polish on the bulk sample running perpendicular to the scan direction of the laser. Bulk sample was then sectioned into smaller pieces using a Mager BR220 precision cut-off saw. The line scans in these samples were then cross-sectioned and polished using 600, 800, 1200 grit silicon carbide paper, then 3 µm and 1 µm diamond polishing solution on a felt pad, followed by 0.05 µm colloidal silica. The final step in the sample

preparation provided a fine etch of the microstructure as the colloidal silica preferentially etched the aluminum rich α-phase.

Line scans performed in the bulk sample were made either as a single pass, multiple adjacent passes, or as multiple passes over the same line. Single passes were performed so that the depth and width the melt pools within a parameter range could be determined through transverse cross-sections of the line scans. Multiple adjacent line scans were performed on the bulk sample so that the melt pool boundaries could be investigated. Within these line scans, the hatch distance was adjusted so that an approximate 25% overlap was given between each pass. Along with this, perpendicular scans were made across the parallel line scans, providing melt pool boundaries at different orientations to be characterized and contrasted. Finally, line scans that were performed over the same track were used to simulate multiple layers within the LPBF process. Longitudinal cross-sections of these lines scans were performed to see how the microstructure grew between layers in a simplified system. Power of these line scans were adjusted so that the first line had the largest melt depth, while the power for sequential lines was decreased to allow for a layer like effect.

2.1.3: LPBF processed samples

Samples made through the LPBF process were done so with a SLM 125 from SLM Solutions. **Figure 2-1** shows a simple schematic of how an object is built within the LPBF process by first coating a build plate with powder and then melting a 2D geometry in that powder layer through a scanning laser. Before each new layer is added, the build plate is lowered a specific amount, thus determining the thickness of the powder layer. Powder is continually fed to the recoater through a hopper, and excess powder is pushed into overflow shoots on either side

of the build plate. All of this is performed within an inert atmosphere of Ar, with a partial O_2 pressure below 1000 ppm.

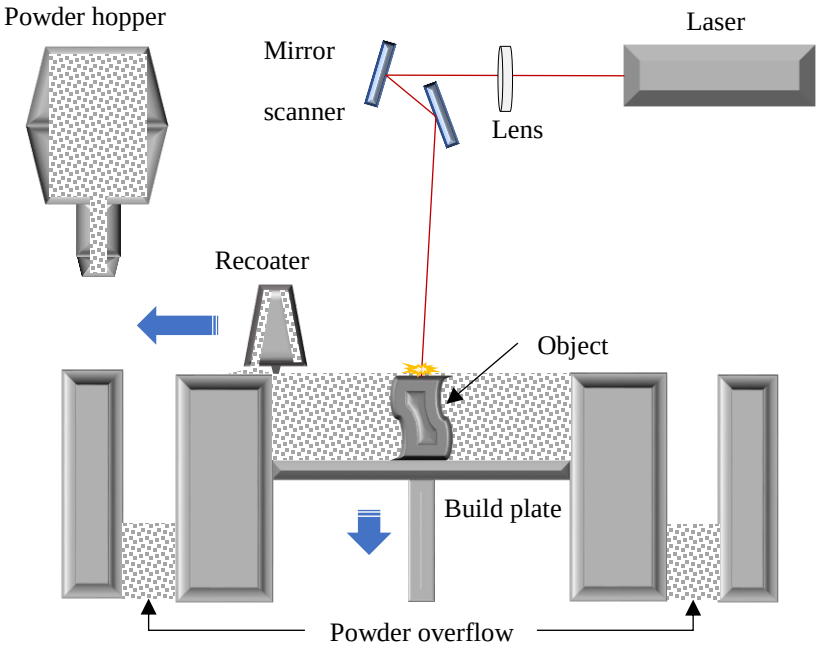

Figure 2-1: Schematic of the laser powder bed fusion process showing the fundamental components.

For smaller samples built with this system, a manual recoating method was used instead of the traditional automated set up to decrease the required quantity of the powder blend needed for the experiment. To perform the manual recoating, an aluminum container with approximately 1 mm holes on the bottom was used to evenly disperse powder blends onto the build substrate via sifting. A stainless-steel straight edge was then used to remove any excess powder, ensuring a powder layer as controlled by the precise lowering of the build plate. Following the manual powder coating, laser melting was performed and the recoating process was repeated. Samples made using this method consisted of both 5 mm x 5 mm x 2.5 mm coupons, as well as single track walls that were 5 mm in length and 2.5 mm in the build direction (typical around 50

layers). The hatch spacing was kept constant for all coupon builds at 100 µm, while all builds had a powder layer thickness of 50 µm and laser beam width 100 µm. The build plate used for these samples was a 6061-aluminum alloy, 12.7 mm thick plate that was later cross-sectioned with the samples.

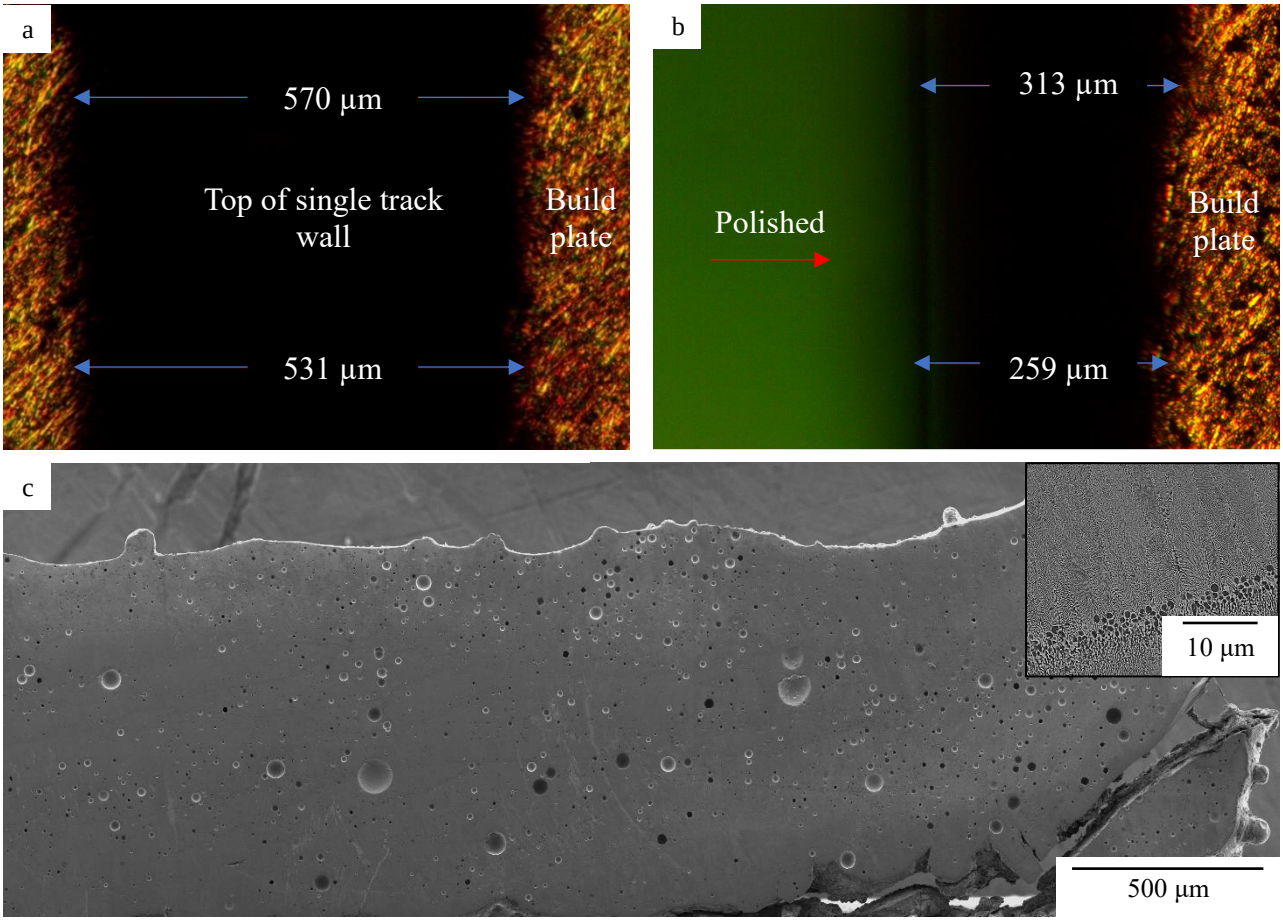

Figure 2-2: Example of preparation of longitudnal cross-section of single track wall samples. Optical microscopy was used to gauge how far into the sample to polish, with (a) showing the outline of the sample before polishing, and (b) showing the the sample after polishing. SEM image of longitudinal cross-section of single track wall (c) where microstructure at the center of the line scan can be clearly seen after polishing (inset).

Dilution from the base plate was observed in all samples to some degree, particularly evident in samples processed at higher laser powers. However, the dilution was confined to the first ten layers of the build. Samples were cut while still attached to the base plate and processed in both

transverse and longitudinal cross-sections to the scan direction. Longitudinal cross-sections of the 100-200 µm wide single track walls were achieved by carefully cutting the sample parallel to the line scan and then slowly grinding and polishing into the sample. Optical images were taken of the surface of the line scans before and during polishing to measure what percentage of the line scan was left in the cross-section, with a goal of removing approximately 50% of the width of the line scan so that the central longitudinal plane of the line scan could be viewed. An example of this process and the resulting sample are shown in **Figure 2-2.**

2.2: Laser systems

Three different laser systems were used to irradiate different powder samples including an Excimer pulsed laser system (wavelength = 248 nm; HWHM = 25 ns, spot diameter = 3-5 mm), a 6.5 W solid-state laser diode (wavelength = 450 nm, beam width = 200 µm) from Endurance Lasers, and a 400 W Yb-doped fiber optic laser (wavelength = 1070 nm, beam width = 100 µm) within an SLM 125 from SLM Solutions Group AG. The experimental set up and procedure performed during the use of each of these laser systems is discussed in detail below.

2.2.1: Excimer laser system

Experiments performed with the excimer laser system were primarily centered on better understanding the morphology changes in irradiated Al-Cu powder, and played a supporting role in elucidating the mechanism by which the collapse morphologies occur in the particles. Because of the high energy and short pulse duration, irradiation from the excimer laser often produces a shockwave, or piston like effect, that exerts a force on the sample. This force caused particles to be pushed away from the center of where the laser pulse hit the powder on the substrate, making

it impossible to know the local environment the particle was irradiated in during post-experiment characterization. The piston effect was also shown to break apart the oxide shell on the larger (>10 μm) Al-Cu eutectic particles when irradiated in atmosphere, and the smaller particles when irradiated under an inert Ar environment, causing particles to lose their spherical shape and or coalesce with neighboring particles. The wattage of the laser was measured before each experiment with a Newport power meter model 1918-C while pulsing at 5 Hz, and the spot size of the laser was recorded using burn paper. From the spot size and the energy of the laser, the fluence could be calculated using **Eq. 2-1** shown below.

$$Fluence\left(\frac{J}{cm^2}\right) = \frac{\left(\frac{Power\,(W)}{frequency\left(\frac{1}{s}\right)}\right)}{\left(\frac{1}{2}\,diameter\,(cm)\right)^2 \pi} * (1 - \%optical\ loss),$$

Eq. 2-1

Optical loss for the set up shown in **Figure 2-3** was approximately 20% (~10% per optic used). Thus a range of fluences could be reached by varying the focal point and thus spot size used. For these experiments samples were irradiated at fluences from 1 J/cm^2 to 3 J/cm^2.

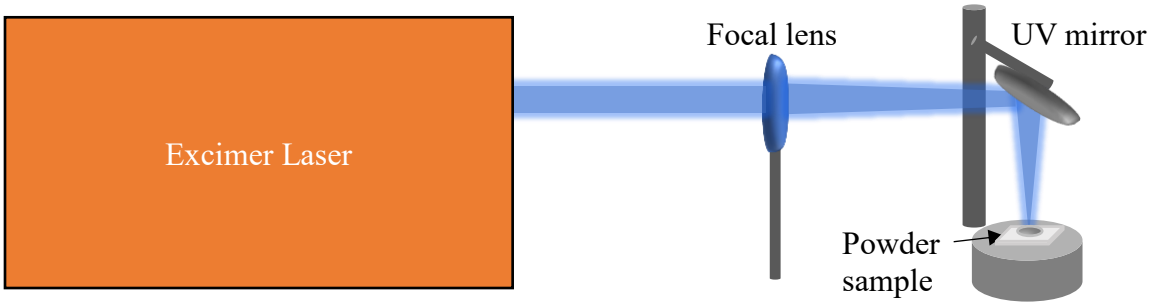

Figure 2-3: Optical set up for powder experiments performed with the excimer laser system.

2.2.2: Solid state laser diode system

The solid state laser diode system provided a steady and lower impact irradiation source with which experiments could be performed that allowed the particles to retain their same spatial orientations both before and after being irradiated. This was critical when trying to understand how the microstructure and morphology of specific particles changed after laser irradiation and what effect their local environment (i.e. neighboring particles) had on this change. These experiments were carried out using conductive ITO coated glass substrates that enabled SEM characterization before irradiation and also was transparent to the wavelength of the irradiation source, keeping the substrate from heating up and thus influencing the heating or cooling of the particles. The power of this laser system was measured to be approximately 6.5 Watts, and the beam could be focused to a spot of approximately 200 μm in diameter. A Newport ILS linear actuator stage was used to translate samples under the focused laser beam at approximately 10 mm/s, providing a line scan across the powder sample. The experimental set up of this system can be seen in **Figure 2-4**. It should be noted that other experiments with this laser system showed that slight power fluctuations were occurring on the order of 60 Hz most likely due to the alternating current of the power source. No periodic fluctuations were observed within the line scans performed within these experiments, although this would have been difficult to discern due to the sparse and stochastic arrangement of the particles in these samples.

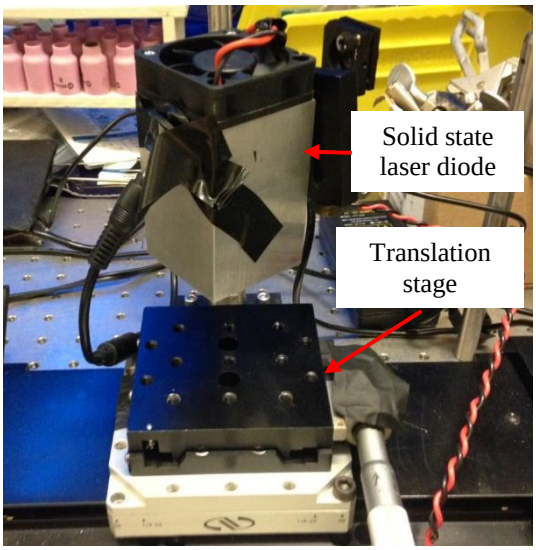

Figure 2-4: Solid state laser diode experimental set up.

2.2.3: Fiber optic laser system

The Yb-doped fiber optic laser system within the SLM 125 machine was used to process the majority of the samples in this work, including the powder, bulk and LPBF built samples. This laser system was integrated within the SLM 125 machine but could be controlled by selecting the preferred laser parameters within the Materialise software used to create SLM files that the machine could read. This laser could be scanned from 1 mm/s up to 4 m/s using a gyrating mirror system as shown in the schematic in Figure 2.1. The power of this laser system could be varied from 20 W to 400 W, and this could further be modified by defocusing the laser beam and widening the spot size. Scan direction and scan patterns for bulk samples could also be controlled within the Materialise software with the software and both unidirectional and bidirectional scan strategies could be designed. SLM files could also be made to where different laser parameters were given to specific regions within a bulk build, i.e. border scans, up skin and

down skin, etc. These features were not used within these experiments though in order to keep variation within the samples to a minimum.

2.3: Characterization techniques

2.3.1: SEM characterization

An FEI Helios G4 DualBeam and FEI LV650 SEM were used to carry out the majority of sample characterization in this work by acquiring secondary electron (SE) and backscattered electron (BSE) images, performing EDS chemical analysis, gathering crystallographic information through electron backscattered diffraction (EBSD), and by taking cross-sections through focused ion beam (FIB) milling. An Everhart-Thornley detector (ETD) and a concentric backscatter detector (CBS) were used to take the SE and BSE images of the samples, with the CBS detector being positioned at the polepiece and the ETD being positioned at approximately a 45° angle to the surface of the sample. These two detectors were used extensively within this work, with the ETD providing surface sensitive information due to the shallow interaction volume of the secondary electrons, and the CBS detector giving higher Z-contrast due to the differences in signal intensities of backscattered electrons that occur between elements of different atomic masses. The difference of the interaction volume, i.e. the depth at which the signal is detected, changes depending on the type of signal. Secondary electrons are produced through inelastic scattering within the material and are detected near the surface due to their lower energy, causing them to have mean free path in metals on the order of nanometers [49]. The detection depth of backscattered electrons on other hand is much greater due to the higher energy elastic scattering within the material. Similarly, X-rays produced within the material from the electron source will be detected from even deeper within the material, reducing the overall

resolution that is associated with the signal. A schematic of the interaction volume of different signals in a material as well as the detector orientation used in this work is illustrated in **Figure 2-5**.

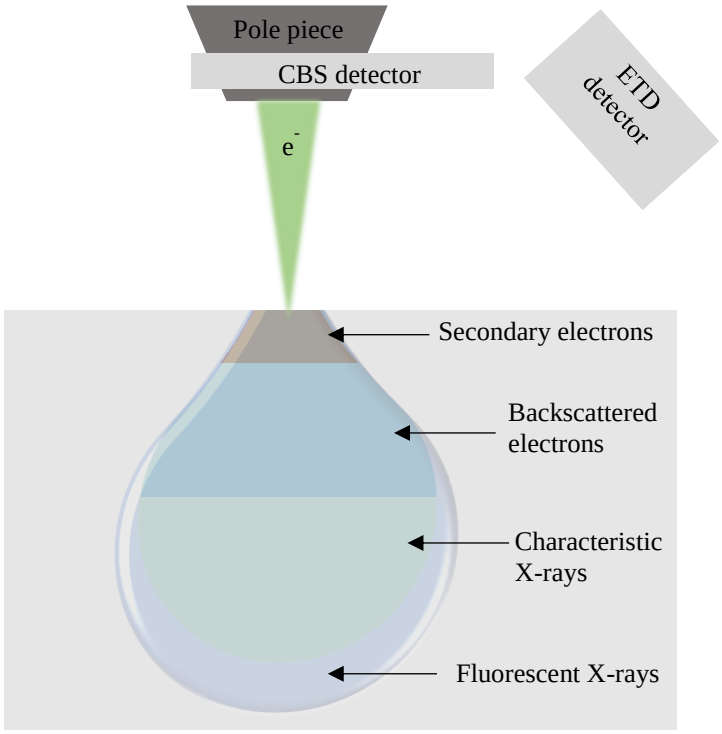

Figure 2-5: Schematic of detector arrangement in SEM along with interaction volume of different signals detected in sample.

The depth and shape of the interaction volume of all signals is dependent on the energy and amount of incident electrons, i.e. the accelerating voltage probe current of the electron source, as well as material specific properties, such as the atomic masses of the elements in the sample. The accelerating voltage and probe current can both be varied within the SEM and should be selected carefully based on the material of the sample and the features that are intended to be imaged. An example of the difference between SE and BSE signals, as well as the difference between different accelerating voltages can be seen in **Figure 2-6**. The SE image taken in **Figure 2-6a** provides more surface details of the sample, and topography due to the

angle of the ETD detector to the surface of the sample. The BSE image provides a better phase contrast due to the elastic scattering of the electrons off of the heavier elements, but also causes features to appear flat due to the CBS detector being directly above the sample. When the accelerating voltage is increased, a clear drop in the resolution is seen due to the increase in the interaction volume, and certain features on the surface of the sample are completely lost.

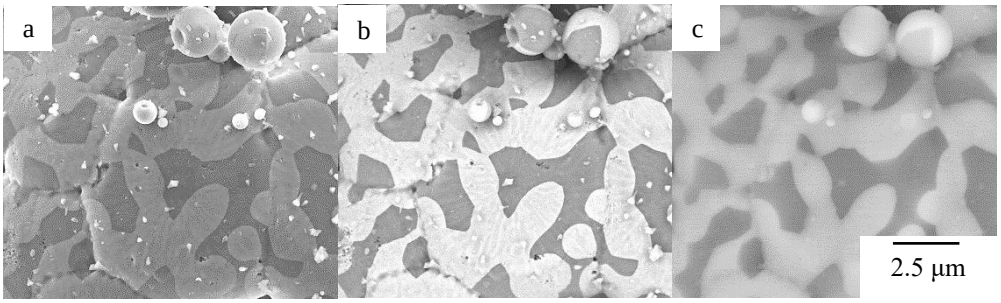

Figure 2-6: Annealed Al-Cu particle imaged with SE at 7 kV (a), imaged with BSE at 7 kV (b), and imaged with BSE at 20 kV (c).

2.3.1.1: FIB Cross-sectioning

Characterization within the FEI Helios G4 DualBeam allowed for in situ cross-sectioning of samples using the integrated FIB. This was critical for powder samples, allowing the internal microstructure to be analyzed without removing the particle out of the local environment in which it was irradiated. A gallium source was used for the FIB and an ion conversion and electron (ICE) detector was used to image the sample during milling using ions as the excitation source. Platinum was often deposited on the surface of the sample before milling to help preventing curtaining effects on the cross-section surface. The accelerating voltage was often lowered from 30 kV to 5 kV for the last pass of the mill in order to ensure gallium ion implantation did not alter the microstructure at the surface of the cross-section.

Along with this, serial sectioning could be performed by the FIB Auto Slice and View software, where fiducial markers allowed the software to automatically FIB small sections away

from a sample and take an image of the newly exposed face before removing another layer of the material. An automatic focus alignment feature was also available with the software that could periodically refocus the sample within the serial cross-sectioning by taking a series of images at different focal lengths and selecting the length that gave the best contrast. After the serial cross-sectioning was complete, the images acquired during this process could be sued to reconstruct a 3D image of the microstructure. Avizo software was used in this work for all 3D reconstructions. Step size of these 3D models were equal to the thickness of each slice that was performed by the FIB, in this work ranging from 20-50 nm. These reconstructions proved valuable when trying to determine how the two-phase eutectic microstructure grew in different environments, specifically within an isolated particle, and at the melt pool boundary of LPBF produced part.

FIB lift outs were performed at specific regions of interest within the microstructure. To perform a FIB lift out, Pt was first deposited over the surface of the region of interest at a depth of approximately 1 µm and a length and width of 10-20 µm and 1 µm. Next, the gallium ion source was used with an accelerating voltage of 30 kV to mill out trenches on either side of the deposited Pt at a depth of approximately 5 µm. The deposition and the milling were both performed with the sample surface oriented normal to the ion source, i.e. with the sample tilted at 52° angle. After the trenches have been made, the sample is tilted so that the ion source is oriented at a 38° angle to the surface of the sample, and an undercut is made at the bottom on the area of interest so that it is attached by only one side to the bulk sample. A needle is then inserted so that it is nearly touching the milled sample, Pt is deposited to attach the needle, and the remaining side of the area of interest attaching it to the bulk is milled away. This FIB lift out is then thinned with the ion source, using progressively lower accelerating voltages down to 2 kV to prevent ion implantation from damaging the crystal structure of the sample, until a final

thickness of 100-200 nm is achieved. This sample is then attached to a copper TEM grid for further analysis.

2.3.1.2: Transmission Kikuchi Diffraction

The EBSD detector within the FEI Helios G4 DualBeam was used to acquire crystallographic orientation of samples through a method known as transmission kikuchi diffraction (TKD) or transmission EBSD (t-EBSD). Similar to EBSD analysis, this technique utilizes kikuchi patterns generated from the diffracting crystal to determine the orientation of the crystal, although here instead of the kikuchi pattern being generated by backscattered electrons, the sample is oriented so that electrons are diffracted as they transmit through the sample. For this to happen, samples used in this technique must be only 100-200 nm in thickness. Because the electrons are transmitted through the sample instead of backscattering from the bulk, the interaction volume is much smaller, allowing TKD to achieve finer lateral spatial resolutions of up to a few nanometers [50]. This was necessary for the laser processed Al-Cu, where the interlamellar spacing was on the order of 10^1 nm. A schematic of the sample orientation along with the EBSD detector is shown in **Figure 2-7**.

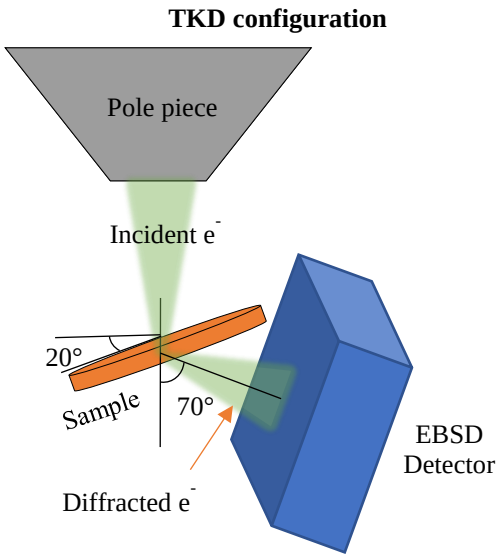

Figure 2-7: Sample orientation with respect to the pole piece and the EBSD detector within the TKD technique.

2.3.2: Rheometry

Rheology data of powders and powder blends were obtained from a Freeman FT4 powder rheometer. These tests were performed directly after drying the powder samples under Ar for over 24 h to remove any water absorbed on the powder that might cause adhesion of the particles. Powder samples were then poured into glass holding vessels and a propeller like blade attachment was used to slowly sift the powder. A series of different tests can be performed with the Freeman FTR rheometer, but in this work analysis of the powder was confined to compression and shear tests. These tests provided several different properties including compressibility of the powder, cohesion, unconfined yield strength, major principle stress, bulk density, flow factor, and angle of internal friction. Although all of these properties describe how the powder will behave, the most straight forward property is the flow factor, which is the ratio of the unconfined yield strength and the major principle stress. This property provides the best

predictor of whether a powder will flow during the LPBF process, with powders that have a value greater than 10 being considered free flowing [51].

2.3.3: Hardness Testing

A VH1102 Vickers hardness tester from Buehler was used to conduct all of the hardness measurements in this work. This was performed on both LPBF processed samples, as well as on line scans performed on bulk samples. Samples were polished down to 1200 grit before conducting hardness tests to remove the majority of surface deformation caused by cutting or grinding that may have induced higher densities of dislocations near the surface. A load of 0.2 kgf (1.96 N) was used for all measurements due to the smaller indent it caused which gave the finer spatial resolution needed to test small features within the samples, such as melt pool boundaries. The Vickers hardness tester was equipped with a pyramidal diamond indenter with an angle of 136° from the surface of the holder. The diagonals of each indent made in the samples were measured under an optical microscope at 50X. The depth of the indents was derived from the following equation:

$$depth = \frac{d_{avg}}{2\sqrt{2} * \tan\frac{\theta}{2}},$$

Eq. 2-2

Where $\theta = 136°$ for the pyramidal indenter and d_{avg} is the average diagonal length of the indent. Each indent made was always separated by at least $3d_{avg}$ from previous indents as well as from the edge of the sample [52]. Calculation of the Vicker's hardness number (HV) is performed by dividing the force applied (F) by the surface area of the indent (A_s) as shown in the following:

$$HV = \frac{F}{A_s} = \frac{F * 2\sin\frac{\theta}{2}}{d_{avg}^2}$$

Eq. 2-3

When converting HV to MPa a simple unit conversion of kgf to Newtons and mm^2 to m^2 yields a factor of 1 HV: 9.807 MPa [52].This conversion is useful when comparing hardness values to mechanical properties such as yield or tensile strength.

2.3.4: TEM

An FEI Titan transmission electron microscope (TEM) and a Themis 60-300 kV TEM from Thermo Fisher Scientific were used to obtain crystallographic orientations and high resolution chemical information respectively. FIB lift out samples of specific regions within the microstructure of the LPBF processed Al-Cu were prepared for TEM analysis as previously discussed in sections 2.1.3: LPBF processed samples and 2.3.1.1: FIB Cross-sectioning. Characterization within the Titan consisted of high resolution electron imaging on the atomic scale, allowing interfaces of both colonies and lamellae to be closely studied, electron diffraction of individual colonies which provide information about the crystal orientation of the lamellae, and "dirty" dark field analysis which clearly highlighted the boundaries of colonies when lamellae were often appeared contiguous across these boundaries in bright field. Along with this, the Titan provided α and β tilt capabilities that could be used to further assess lamellae orientation relationships within the colonies. EDS chemical analysis performed on the Themis was performed to characterize and tertiary impurity elements that were within the samples. This was performed using high resolution scanning transmission electron microscopy (STEM) in high angle annular dark-field mode (HAADF).

Chapter 3 : Utilizing eutectic microstructure to analyze solidification events during LPBF

3.1: Background

The relationship derived by Jackson and Hunt between the steady state growth velocity of the eutectic solid-liquid interface and the interlamellar spacing of the resulting microstructure allow for a post-process analysis of the solidification that occurs within a sample. This, along with other aspects of eutectic solidification such as its directionality and its sensitivity to fluctuations in the composition, provides a wealth of information when trying to understand specific solidification mechanisms within a processing technique. Use of the eutectic microstructure in this way has been applied in the past to understand solidification phenomenon in different processing techniques, such as recalescence in gas atomized particles[53,54,55]. In the work performed by Trivedi, et al., on Al-Si eutectic particles, the direction and spacing of the two phase microstructure was used to show how the particles solidified from a nucleation point and underwent recalescence towards the end of the solidification process. The interfacial velocity, thermal gradient, and cooling rate were all estimated in this study from the eutectic microstructure of the particles.

Other processing techniques such as casting and melt spinning have also used eutectic alloys, specifically the well-studied Al-Cu system, to experimentally determine the cooling rate of the process and understand how changes in the parameters may affect the solidification velocity[56,57]. Recently, Pauly, et al., attempted a similar approach to estimate the cooling rates of LPBF built Al-Cu eutectic samples processed at different laser parameters[13]. The goal of this study was to determine if the cooling rate changed throughout the entirety of a build at two

different parameters, yet the data presented is difficult to interpret due to the layer-by-layer process of LPBF. For within each melt pool track, the microstructure, and thus cooling rate, will vary from the edges to the free surface due to the geometry of the melt pool and solid-liquid interface[8]. Therefore, trying to determine the cooling rate from a sample composed of layers of melt pools, with each melt pool being melted over by the following one, is a difficult task to say the least. To properly make an analysis of the interlamellar spacing, a cross-section must be taken along the axis where the highest solidification rates occur, i.e. along the center of the melt pool. With this, the angle of the microstructure must be taken into account in accordance with the free surface, for the fastest solidification will occur where the solid-liquid interface is oriented normal to the translation of the laser. In the present work these challenges are overcome by building single track "walls", and taking the longitudinal cross-section of these walls to determine the interlamellar spacing. The actual solidification velocity can then be normalized through the relation

$$v_s = v_b \cos\theta,$$

Eq. 3-1

where v_s is the solidification velocity, v_b is the velocity of the laser beam, and θ is the angle between the solid-liquid interface and the surface of the melt pool.

In addition to providing experimental evidence of the cooling rate, the eutectic microstructure can also provide a record of any fluctuations in the motion of the melt pool through a phenomenon known as banding. The term "banding" may be used to refer to a number of different solidification phenomenon all of which produce oscillating structures that form parallel to the solid-liquid interface[58]. These bands can be caused by both internal factors, such as nonequilibrium effects or nucleation events, or by external factors, such as those associated

with the processing technique itself. It is the externally driven banding that is useful when leveraging the eutectic microstructure to understand the solidification that occurs within LPBF, for these bands occur when the velocity of the solid-liquid interface slows suddenly, and then returns to the previous velocity. This type of banding has been previously investigated within other processing techniques, specifically that of welding, where correlations of the banding microstructure with ripples that form on the surface of the melt pool were investigated [59,60]. One of the conclusions drawn from a study by Garland and Davies was that periodic surges in the power source were the cause of both the ripples and bands in the weld. Other studies, such as that of Bennet and Mills, have correlated ripples with the depth to width ratio of the melt pool in steel welds [61]. In regards to LPBF, eutectic banding may possibly contribute to a better understanding of the fluctuations of the melt pool that occurs during laser keyholing[62].

Lastly, the composition dependence of the formation of the two-phase eutectic microstructure may be used to elucidate fluctuations of composition that occur within the melt pool. This is specifically useful when investigating the possibility of performing in situ alloying within LPBF, where elemental powder blends are alloyed during laser melting. For Al-Cu eutectic, Gill and Kurz showed that the microstructure that forms liquid is dependent on both the solidification velocity as well as the composition of the solute [37]. In the microstructure selection map they produced experimentally, the nominal lamellar microstructure of Al-Cu eutectic will only form if the solute concentration is kept between ±3wt%Cu at solidification velocities of 100 mm/s. Above or below this range hyper- or hypoeutectic microstructures will form respectively, providing a clear record of where local deviations of the composition in the liquid occurred. Other methods to characterize the local composition inhomogeneities within a sample made through in situ alloying have been attempted using EDS by such groups as Ewald, et al., yet this

method is better suited to characterize local compositions, and would be tedious to use over large areas [63,64].

3.2: Morphology changes in LPBF recycled powder feedstock

3.2.1: Motivation

In the field of laser powder bed fusion (LPBF), much research has been focused on characterizing the changes that occur in the powder feedstock after laser irradiation in order to better understand the limitations of its powder recyclability [65,66]. The majority of these studies assume that all irradiated particles undergo melting and are incorporated into the melt pool of the laser track, focusing on the spatter that is ejected from the melt pool as the main source of defects in recycled powder [67,68,69,70]. However, very few consider particles on the peripheries of the laser track which have been irradiated but not incorporated into the melt pool. If no sintering between neighboring particles occurs, this irradiated powder will end up being recycled and used in sequential builds [71,72,73,74]. Studies that focus on recycled powder are vital for the LPBF process since morphology irregularities of the particles could lead to failed builds due to uneven powder flow and spatial distribution [75,76]. Thus, a better understanding is needed on the mechanisms behind the morphological anomalies observed in recycled powder, especially those systems such as aluminum based alloys that contain a tenacious native oxide shell that could pose a barrier to sintering [67,77,78,79].

Recent studies have started to categorize the different types of particle morphology found in recycled powder. For example, Popov, et al., identified thirteen different particle defects within the Ti-6Al-4V system ranging from mechanically induced (broken particles) to agglomerates caused by spatter from the laser melt pool [80]. In order to better understand the

formation of spatter-type defects within the AlSi10Mg system, Andani, et al., used a high-speed camera to capture images of the laser melt pool in situ [81]. From this study they proposed that both powder particles and liquid spatter were being jettisoned from the lasers path due to the recoil pressure of the laser. The nature of the jettisoned powder was not discussed further by Andani, et al., but a similar "partially heated" powder is brought to attention by Asgari, et al., on their study of the same system (AlSi10Mg) [78]. In this study, only the large particles separated through sieving are thought to be affected by the laser, and are assumed to be agglomerates, or "condensate", due to their large size and fine microstructure. It was suggested that the mechanism behind the formation of these large particles and their fine microstructure was related to the heating-cooling cycles and partial sintering between particles. In contrast to this conclusion, Lutter-Gunther, et al., showed by isolating spatter from the feedstock powder that agglomerated particles originate from the laser melt pool, and further categorized spatter that solidified in air as spherical spatter, and spatter that solidified on other particles as agglomerated spatter [67]. It was also shown in this study that individual particles (non-agglomerated) were blown out of the melt pool, but little was done to characterize these particles to see how they had changed from the virgin powder.

Because it is common practice within the LPBF process to sieve powder with mesh sizes of below 70 μm, most agglomerated particles will be removed from the recycled powder before reuse [65,73,78]. Thus, a degradation in the rheology of recycled powder is more likely to come from morphology changes of smaller, non-agglomerated particles [82,83]. Changes in the rheology between gas atomized and plasma atomized Ti alloy powders were attributed to slight differences in the sphericity of the particles by Yablokova, et al., suggesting that even small alterations to the shape of spherical particles will lead to poor flowability [84]. It becomes

imperative then to understand how laser irradiation affects the morphology of powder that is neither included into the melt pool nor formed into an agglomerate. Particles that fit into this category could potentially be found in the "blown powder" as well as along the sides of the melt pool, assuming a standard Gaussian power density distribution for the laser beam profile. In addition to this, powder alloys with naturally occurring oxides that could pose barriers to sintering and agglomeration may have a higher density of these non-agglomerate, heat-affected particles in the post-sieved powder [77,79,85].

In this investigation, elemental Al and Al-Cu eutectic alloy powders are characterized before and after laser irradiation to assess and understand morphological changes that occur in the particles. It is suggested that particles on the edge of the laser melt pool can undergo melting and solidification during LPBF without incorporation into the melt pool or isolated agglomeration. The Al-Cu eutectic system is used in this study as a device to record the thermal history of the particles since changes in the two-phase microstructure can be observed through scanning electron microscopy (SEM) [86]. To confirm that melting and solidification contributed to the morphological anomalies, individual particles are characterized both before and after laser irradiation. From these results, a direct correlation is made between laser irradiation and changes observed in particle surface morphology. It is shown that the retained oxide shell plays a crucial role in the prevention of sintering and the development of aspherical morphologies.

3.2.2: Results and Discussion

3.2.2.1: Base powder characterization

The as-received Al-Cu eutectic powder exhibited a range of eutectic microstructures as shown in **Figure 3-1a**. These microstructural differences arose during gas atomization due to

stochastic nucleation of the solid phase in the molten particles at varying undercoolings. An isothermal annealing of the powder was used to produce a coarsened two-phase microstructure uniformly across all particle sizes, with an average interlamellar spacing of 2 μm shown in **Figure 3-1b**.

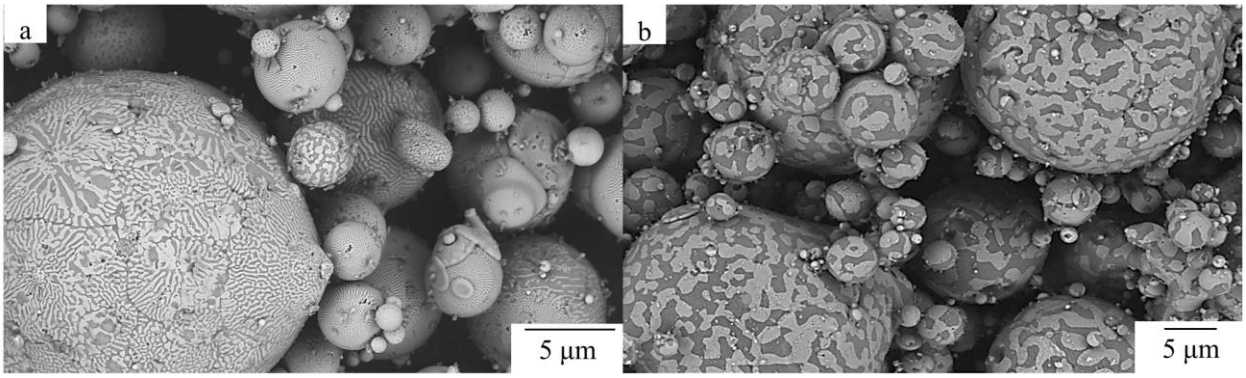

Figure 3-1: As received gas atomized Al-33wt%Cu powder displaying fine eutectic microstructures (a). Powder annealed at 450°C for 2 hours showing uniformly coarsened eutectic microstructure (b).

Closer inspection of the annealed powder surface reveals faint lines superimposed on the annealed microstructure, which are believed to be the imprint of the as-received microstructure embossed on an oxide shell as seen in **Figure 3-2**.

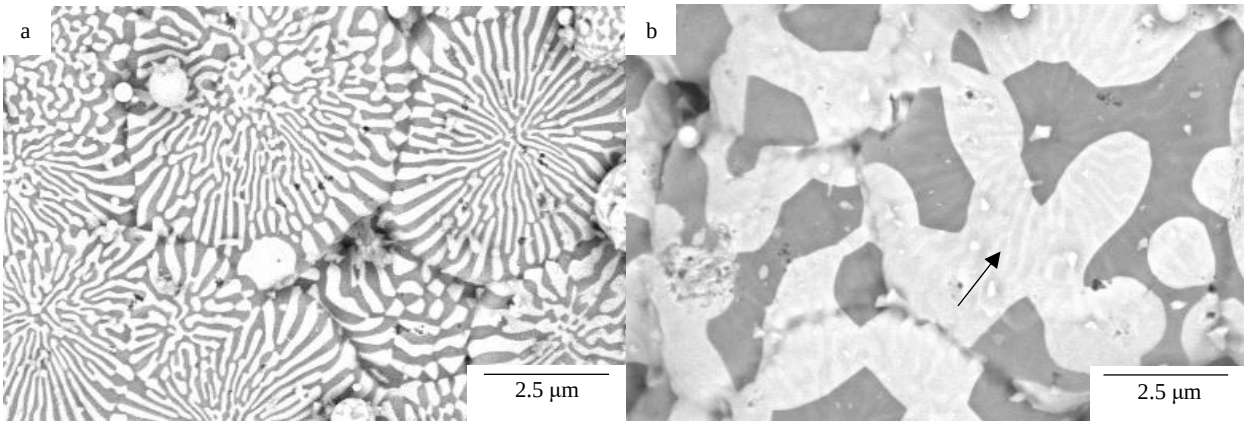

Figure 3-2: Lamellar microstructure of as received powder (a), coarse microstructure of annealed powder showing faint lines (black arrow) of original lamellar microstructure embossed on the oxide shell (b).

These features could only be detected at probe currents below 7 kV within the SEM, suggesting that the secondary and backscattered electrons forming this signal were coming from a very thin surface layer. Both powder systems had satellite particles on the surface of larger particles, typical of gas atomized powders. Elongated and irregularly shaped particles were infrequently observed within both powders. The elemental Al powder (**Figure 3-3**) exhibited a rougher surface morphology than the annealed Al-Cu powder (**Figure 3-2**). Both powders consisted of a low percentage of particles that contained dents on their surfaces, but none were observed with distinguishable cusps, or collapsed-like morphologies, such as will be shown to form after laser melting.

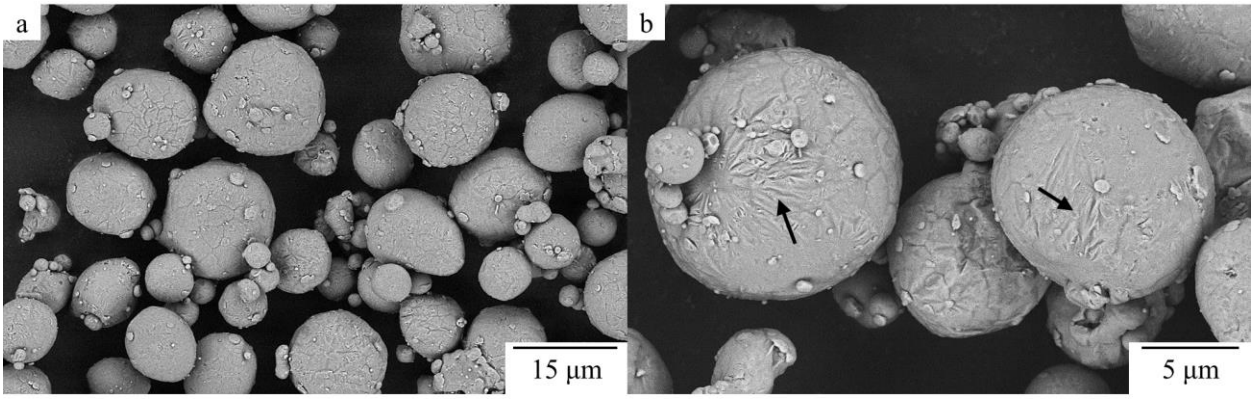

Figure 3-3: As received pure Al gas atomized powder (a). Surfaces of many particles appear rough due to a wrinkling (black arrows) effect most likely occurring during the gas atomization process (b).

3.2.2.2: Morphology changes during LPBF

Processing parameters for line scans were chosen to be comparable with those found in literature for the manufacturing of Al10SiMg in the LPBF process, being one of the most commonly manufactured and studied aluminum alloys in the field [87,12,10]. Powder collected from

the vicinity of the line scan boundary in the Al powder showed large agglomerates (50-200 μm) formed along the laser's scan path.

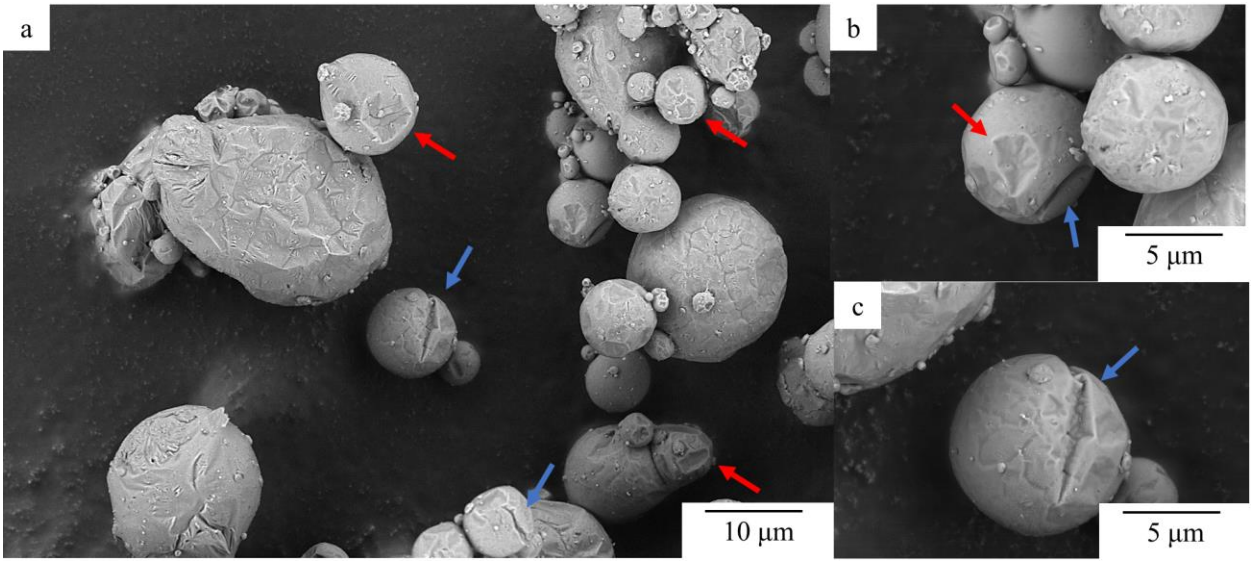

Figure 3-4: Al powder collected on carbon tape around line scan performed at 300 W and 1150 mm/s, with large agglomerates clearly seen along laser path (a). Many particles at edge of line scan that did not agglomerate show morphological anomalies not typical of base powder, showing (b) dented (red arrows) and (c), rift-like (blue arrows) morphology.

Since these larger particles would most likely be removed from the recycled powder during sieving, they were ignored, and smaller particles near the edge of the line scan were investigated. Morphological features not characteristic of the base powder were observed in small particles with diameters <20 μm near the edge of the laser path, with very little signs of agglomeration or sintering between neighboring particles, as seen in **Figure 3-4a**. Morphological abnormalities on smaller particles consisted of concave features circular in nature, defined here as *dents*, and narrow, collapsed-like features that contain an abrupt straight edge, defined here as *rifts*. **Figure 3-4** shows examples of these dent and rift features, highlighting them with red and blue arrows respectively.

Line scans were then performed in the Al-Cu powder at the same parameters and characterized in a similar manner. Large agglomerates were again observed, but approximately 5

times less frequently than in the pure Al. Due to the two-phase microstructure of this eutectic powder, a clear distinction could be made between particles that were close to the edge of the laser path with those that were farther away as seen in **Figure 3-5**.

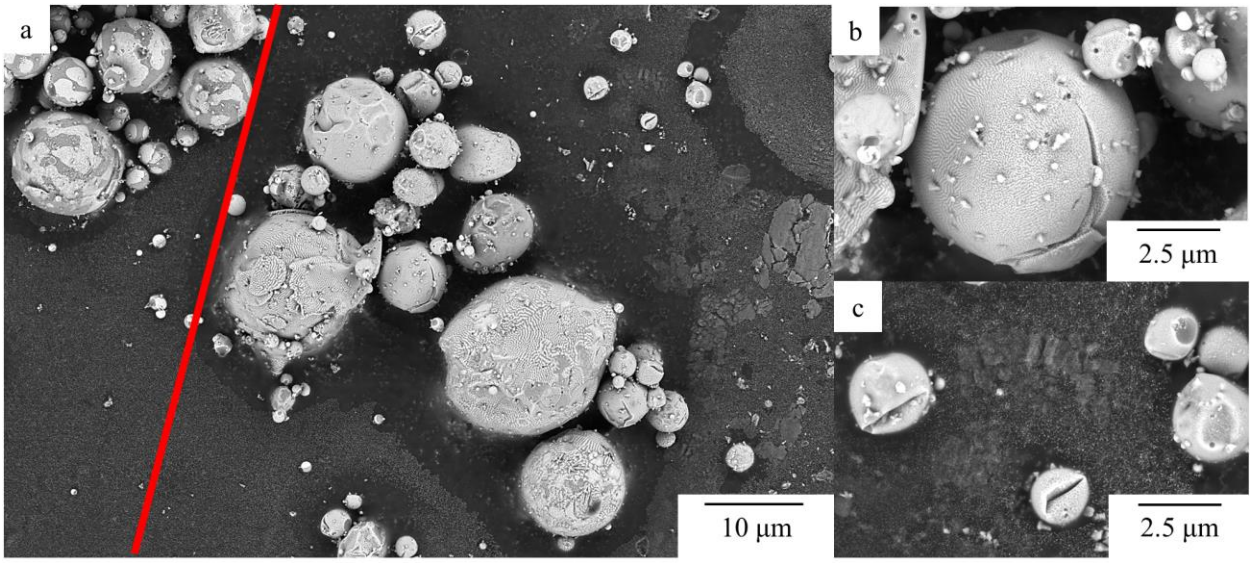

Figure 3-5: Al-Cu eutectic powder collected on carbon tape around line scan at 300 W, 1150 mm/s. Powders collected at edge of line scan show a clear change in microstructure (right side of red line) from the coarsened base powder (left side of red line) (a). Closer inspection of irradiated particles shows signs of dented and rift like morphology similar to those observed in the irradiated Al powder (b&c).

The microstructure of the particles on the edge of the scan changed from the coarsened eutectic to a fine lamellar or dendritic structure. Morphologies distinct from the base powder could also be associated with these particles, with **Figure 3-5b&c** showing dent and rift features similar to those observed in the Al powder. To obtain a finer microstructure after laser irradiation, eutectic or dendritic solidification must occur, depending on the local solidification rate in each particle. As is well-known in solidification theory, the lamellar eutectic period or the dendrite arm spacings are inversely related to both the undercooling and the solidification speed associated with the liquid/solid interface [88]. In powders, nucleation events depend strongly on the number of potential heterogeneous nucleation sites, such that the undercooling obtained in

individual particles will be stochastic. In addition to nucleation, differences in the local environment of the molten particle, such as the overall contact area with heat sinks, will also change the rate that heat is extracted and thus the solidification rate. It is therefore understandable (and observable) that the microstructure of the irradiated particles will vary, but that all particles that have undergone melting and solidification after laser irradiation will be distinct from the coarsened starting powder.

3.2.2.3: Characterization before and after low power CW irradiation

To further investigate the morphology changes seen in the Al and Al-Cu particles along the edges of the line scans made using LPBF parameters, a model system was explored. Dilute powder dispersions on inert substrates were prepared and the same sets of particles were characterized both before and after laser irradiation. Optically transparent and electrically conductive ITO-coated glass was used so that samples retained optical transparency while minimizing charging effects in the SEM without need for any additional coatings over the particles. A 6.5 W laser was used in these experiments at scan rates of 5-10 mm/s; the low power minimizes shock-induced movement of particles on the substrate. This lower power irradiation can be related to the local power density found at the edge of a high-powered laser with a Gaussian distribution beam profile, consistent with the LPBF system. The wavelength of this laser differs from that of the lasers used in the LPBF experiments. This could cause some quantitative changes in thermal transduction, but these are likely to be minor. These experiments permit before and after characterization of microstructure changes on the same particles, which provides deeper insight into the general mechanistic behaviors associated with the resolidification process, as will be shown and discussed below.

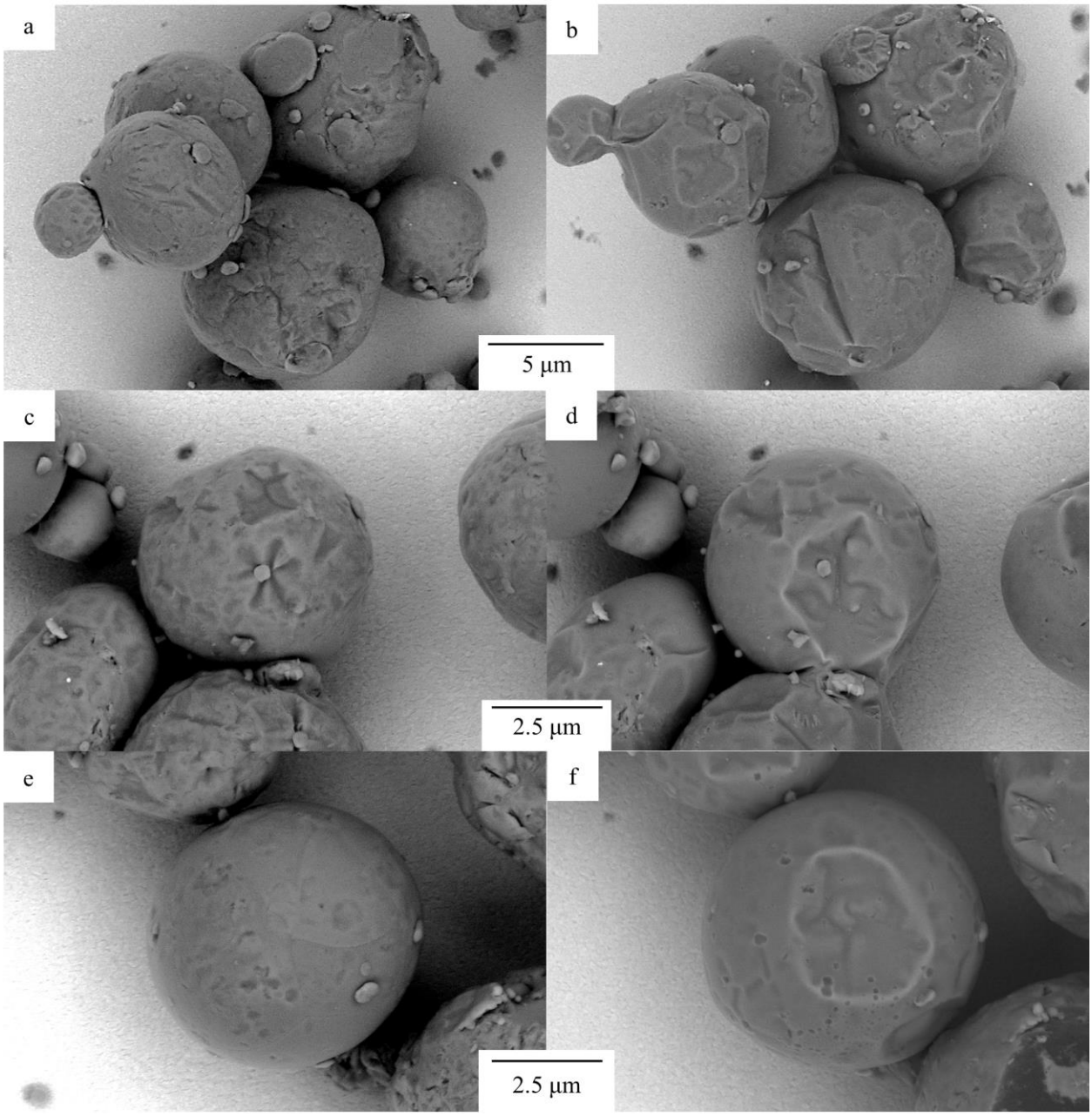

Figure 3-6: Al powder on ITO-coated glass before laser irradiation (a,c,e) and after (b,d,f). Irradiated particles show dented or collapsed like morphologies, with some displaying sharp rift like features (b). Very little wetting is seen to occur between particles (b&d) most likely due to an oxide barrier. The spot size of the laser used was ca. 200 µm, allowing for irradiation of all particles within each cluster.

Characterization of the elemental Al powder in these experiments showed that morphology changes occurred as a result of laser irradiation, with dented and collapsed features

appearing post-irradiation as seen in **Figure 3-6**. No large agglomerates were observed in these experiments, with only limited sintering occurring between neighboring particles post irradiation as seen in **Figure 3-6b&d**. Particle satellites often serve as useful fiducials to verify that identical regions on specific particles are being compared before and after laser melting.

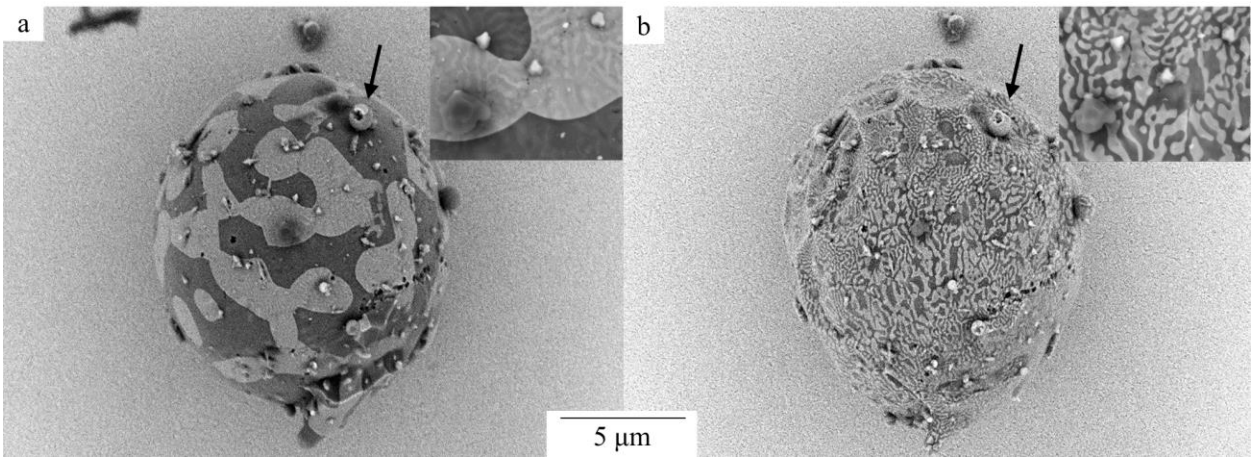

Figure 3-7: Isolated 10 µm particle before laser irradiation (a) and after (b). Satellite particles are found in the same position on surface of particle after laser irradiation (black arrow) with no agglomeration taking place.

By performing these same experiments with the Al-Cu powder, the mechanism behind these morphology changes could be better understood by observing the change in microstructure of the individual particles. As with the line scans performed in the LPBF system, the microstructure of the irradiated particles changed from the coarse eutectic structure to a fine lamellar or dendritic structure as shown in **Figure 3-7**. Minimal sintering was observed between particles, and the post-irradiated morphologies resembled those found in the experiments conducted with the Al powder. In addition, FIB cross-sections were taken of several irradiated Al-Cu particles to ensure that the fine eutectic structure was consistent throughout their bulk (refer to electronic supplementary material). By performing serial cross-sectioning on several

particles, the solidification direction was able to be determined, which facilitated understanding of how these collapsed features arose, as discussed in the following sections.

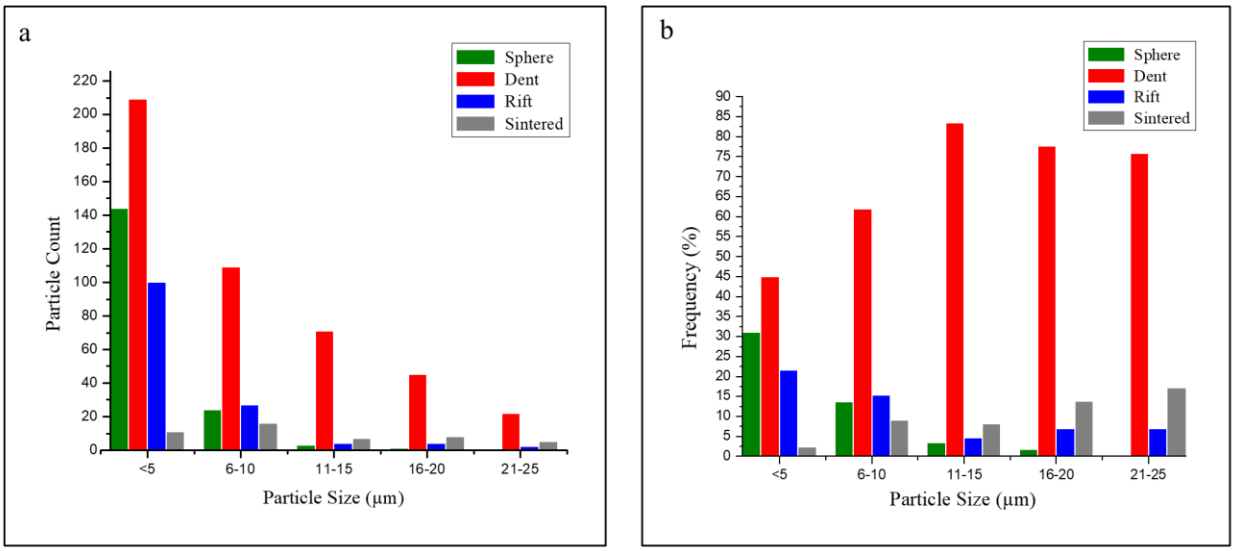

Figure 3-8: Number of irradiated Al-Cu particles observed to display either a spherical, dented, or rift like morphology, as well as those that were sintered together, categorized by size (a). Normalized data showing trends in the occurrence of different morphologies, such as a higher percentage of particles with spherical and rift morphologies occurring in smaller particles, while larger particles appear to have a higher occurrence of sintering events (b).

To better understand trends in the observed morphologies, over 800 Al-Cu particles were counted and categorized according to their size and surface features (i.e. spherical, dent, rift or sintered) as seen in **Figure 3-8**. The changes in the eutectic structure provide definitive proof that these particles underwent complete melting. It is clearly seen from this data that the majority of the irradiated particles in all size ranges displayed dent-like morphologies.

The normalized data in **Figure 3-8b** reveals that larger particles have a higher tendency to deform as the majority of particles in size ranges greater than 10 µm were categorized as either dented or sintered. In addition, particles less than 10 µm in diameter have a higher frequency of both rift and spherical morphologies. Particles that were irradiated and did not display a dent or

rift feature were categorized as spherical, although many of these particles may have features hidden from view in the SEM. This same reasoning applies to particles that were categorized as sintered, with the possibility of hidden sintered particles existing in the sample that were not counted. Thus, for the spherical and sintered particles, the values displayed in **Figure 3-8** represent the respective upper and lower bounds of these categories. It should be noted though that sintering events were about five times more frequent in the Al powder than in the Al-Cu powder system. This suggests the oxide shell may play more of a critical role in the Al-Cu system, as will be discussed.

3.2.2.4: Morphology changes after pulsed laser irradiation

A parallel study was performed using an excimer laser (wavelength = 248 nm; pulse duration at HWHM = 25 ns) to see if pulsed laser irradiation produced similar morphologies in the powder. It was theorized that the pulsed laser would ablate the oxide off the surface of the particle, and that this would free the particle to either wet the substrate, or form a smooth spherical droplet. In the first experiments performed, the fluence of the laser was kept low (1 J/cm^2) and Al-Cu eutectic particles were irradiated with one pulse. The larger particles in these experiments showed no change from the original microstructure, nor changes in the morphology. Yet the smaller particles (<5 μm) were found to have similar dent and rift morphologies as the experiments performed with the CW lasers. **Figure 3-9** shows an example of the morphologies and microstructures observed in the smaller particles after pulse irradiation. In the next round of experiments, the laser fluence was doubled, and a layer of Al-Cu powder was irradiated on a glass slide for the duration of one pulse. The increase in the fluence was enough to melt the larger particles, and sintering as well as contiguous melting was seen in this sample. It was

assumed then that a fluence of 2 J/cm^2 was sufficient to both ablate the oxide shell off of the particles, and to melt the larger particles. It should be noted here though that when particles were applied to a glass substrate using the drop cast method (as discussed in 2.1.1: Powder processing) at low concentrations so that particles were mostly isolated on the glass, that one of two results would occur: 1) particles would not melt, or 2) particles would be blown off the glass substrate through the force of the laser pulse and the resulting piston effect. The reason particles would not melt when isolated at this fluence was most likely due to the lack of reflection and scattering events that occur from neighboring particles, allowing photons multiple opportunities to be absorbed by the metal particles. To remedy this, a low concentrations of dispersed particles were stamped onto a piece of carbon tape and irradiated at a higher fluence (3 J/cm^2).

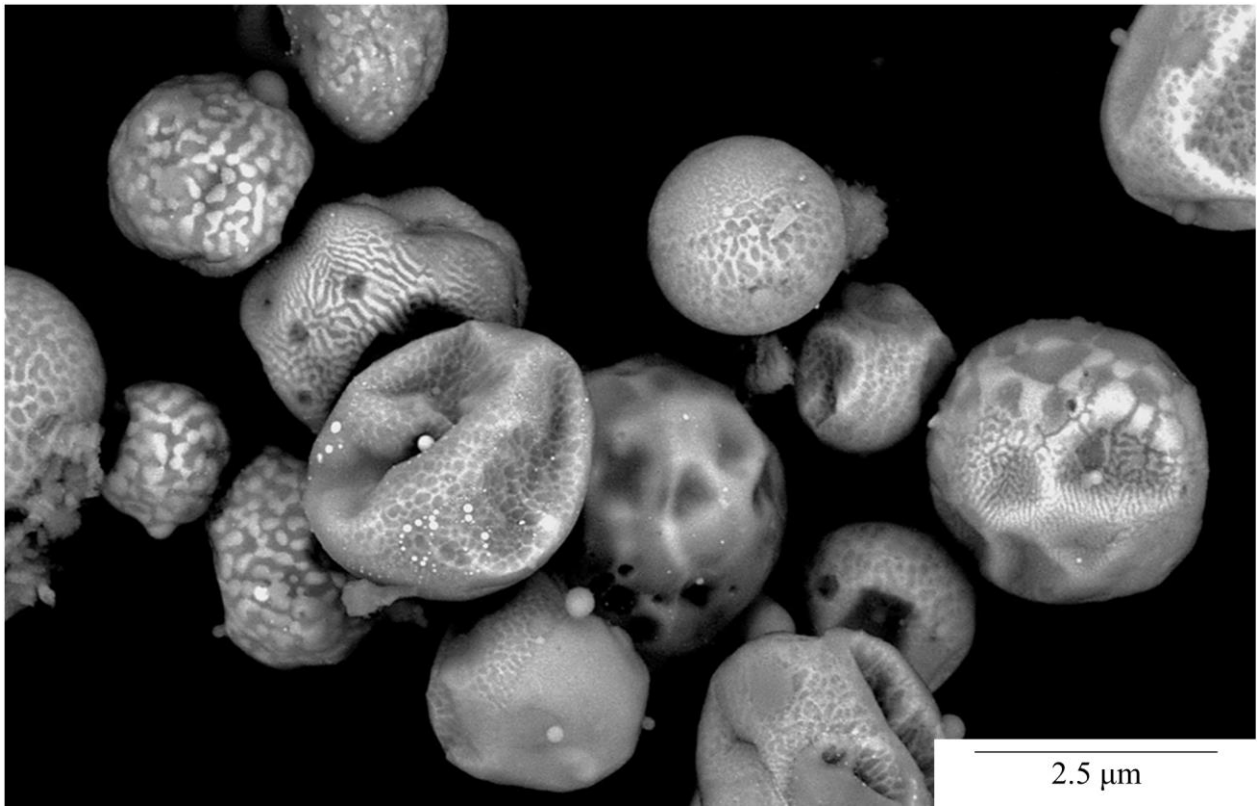

Figure 3-9: Small Al-Cu (< 5 μm) particles irradiated by an excimer pulsed laser on glass substrate at 1 J/cm2. Particles show no signs of sintering with severe collapsed morphologies, suggesting oxide remained intact during irradiation and buckled upon cooling and solidification.

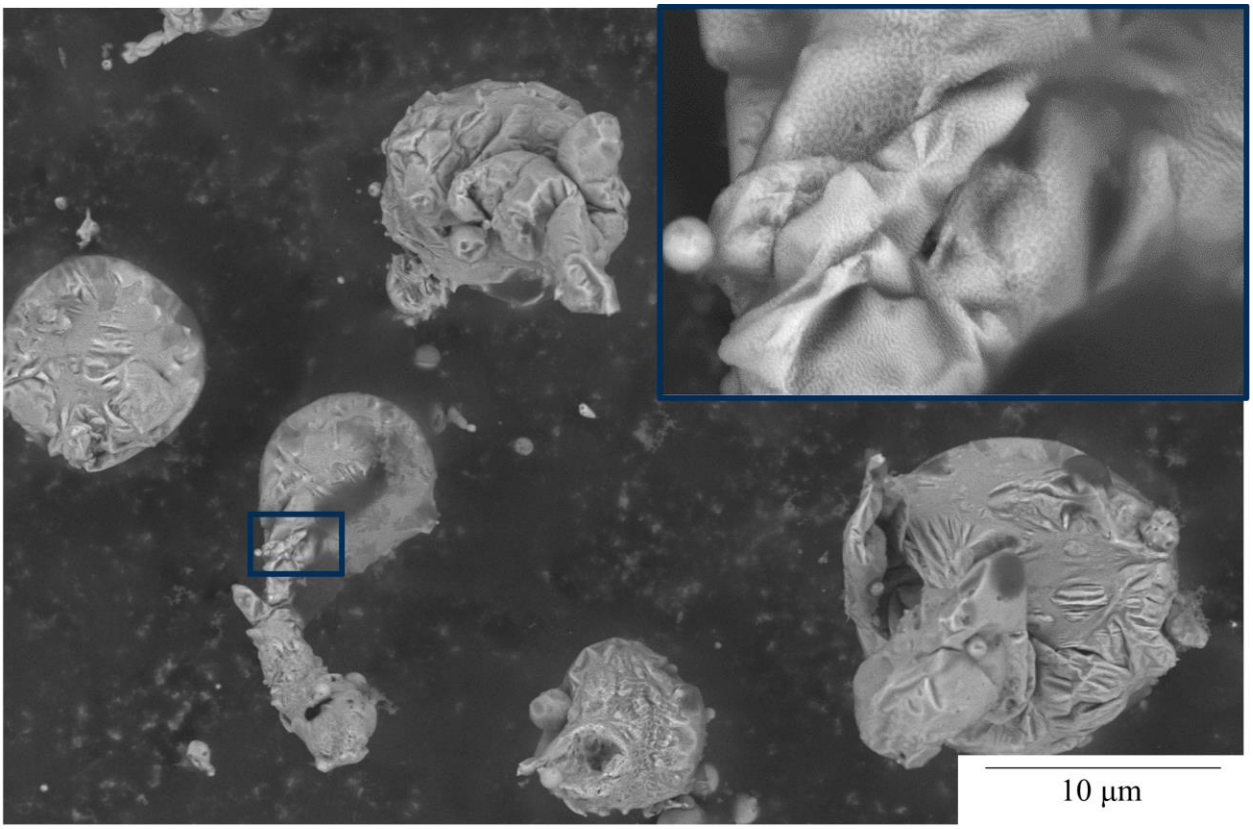

Figure 3-10: Al-Cu particles in air while embedded on carbon tape at 3 J/cm^2. Particles displayed pillars of ejected material from their surfaces, while lower half of particles remained spherical. Inset shows fine eutectic microstructure, indicative of rapid solidification, occurring within the base of the pillar.

These experiments were successful in producing at least partially melted large Al-Cu particles that were spaced far enough apart to be examined individually. Along with this, a strange morphology of the particles was observed, where long pillars of material were seen coming from the tops of the particles as shown in **Figure 3-10**. These pillars most likely formed due to the ablation of the oxide shell on the top of these particles, which allowed the molten interior to be ejected upward with the recoil force of the pulsed laser. This ejected material then froze in place, making the observed morphology. The formation of these pillars suggest that the oxide shell is

indeed being ablated on the surface, but even so, remains intact enough so that the ejected material occurs only locally, while the rest of the particle remains a mostly spherical morphology.

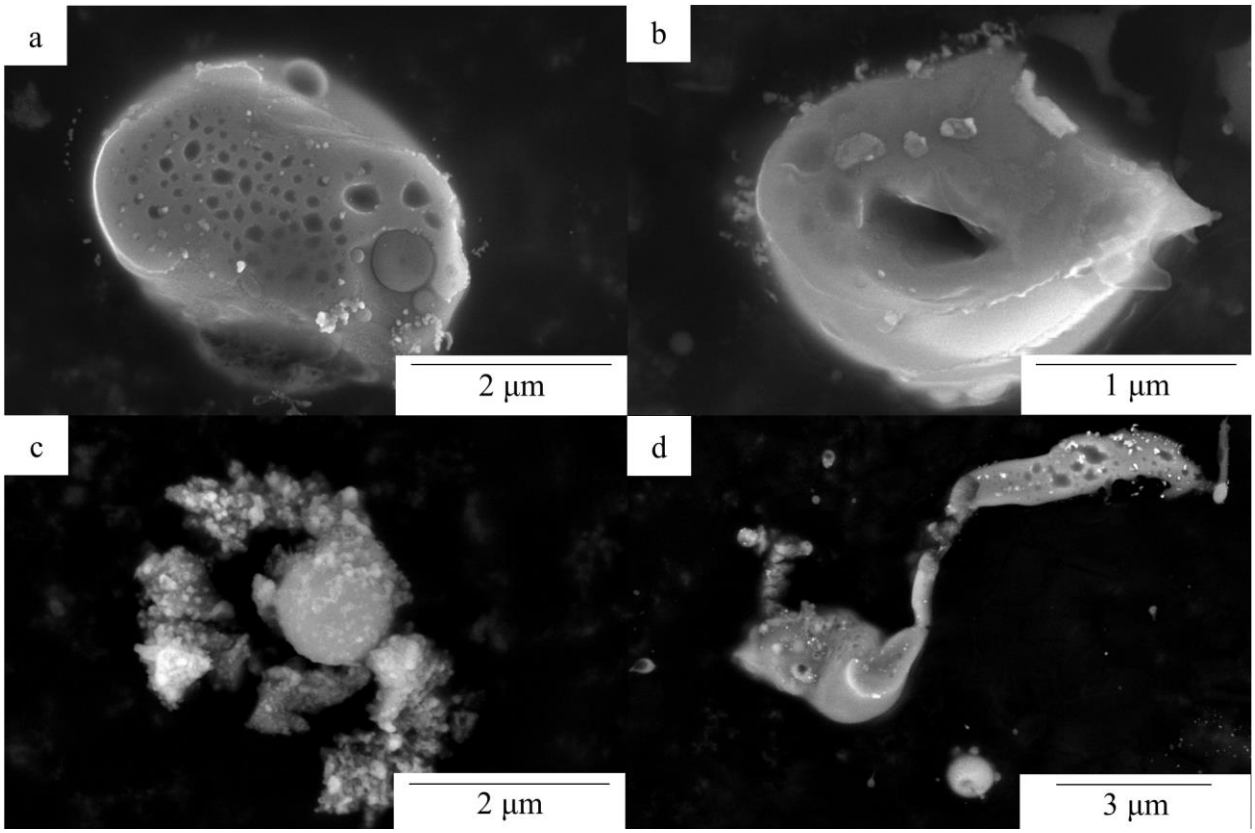

Figure 3-11: Al-Cu particles irradiated by an excimer pulsed laser in an inert Ar environment at 2.4 J/cm^2 on a glass substrate. The interface between the particle and the substrate shows signs of wetting (a,b) and several particles appeared to have burst while molten (c,d).

A final set of experiments were performed with the smaller Al-Cu particles, this time at a high fluence (2.4 J/cm^2) and within an inert Ar environment. This was done to observe what the morphology of the irradiated particles would be if the oxide shell was ablated and could not dynamically grow in time to contain the molten interior. The results of these experiments are shown in **Figure 3-11** where both wetting of the substrate and ejection of the molten material was observed. The two-phase eutectic microstructure of the particles in this experiment were not

observed indicating that either the features were too fine for detection with the SEM, or that the solidification velocity of these particles was high enough (>1000 mm/s) to produce a metastable solid solution phase. Either case implies that these particles were solidifying at higher rates then what was seen in previous experiments. This may possibly be due to the fact that a much greater surface area of the liquid was in contact with the glass substrate due to the wetting of the molten particle, which allowed for a greater heat sink and rapid solidification.

3.2.2.5: Origins of morphological change

Based on the experimental data, it is suggested that a native aluminum oxide on the surface of these particles can serve as a containment vessel surrounding molten metal. Retention of a contiguous oxide shell supports many observations herein, including retention of discrete satellites even after melting of the primary particle, infrequent sintering, and surface "embossing" of the microstructure prior to melting (see **Figure 3-2**). Native oxide shells on Al alloys are inevitable, and the thickness of the native oxide of pure Al at room temperature in atmosphere stabilizes at ≤5 nm [89]. The eutectic Al-Cu powder is expected to have a thicker oxide on the order of 15 to 20 nm since it was heated in air at 450 ºC for 2 hours. From the literature, it has been shown that furnace heating of pure Al under these conditions produces an oxide shell estimated to have a net thickness of 18 nm [90]. The larger oxide thickness of the annealed Al-Cu powders correlates with the reduced number of sintering events observed vis-à-vis the Al powders (which were not pre-annealed), as a thicker oxide would provide a larger barrier to these events. Interestingly, Al_2Cu is found to oxidize more readily than Al alone at room temperature, which could result in a locally thicker oxide above the θ phase [91]. An increased oxide thickness

of the θ phase would explain for the "embossed" pattern observed on the surface of the eutectic powder as seen in **Figure 3-2b**.

The major morphological changes in resolidified Al and Al-Cu powders, e.g., dents and rifts, can be attributed to the presence of an oxide shell. Upon heating of a particle during laser irradiation, the metal undergoes thermal expansion in both the solid and liquid phases, as well as expansion at the melting point due to density differences in the two phases. For example, the total expansion expected in pure Al going from room temperature to just above the melting temperature (~ 660 ºC) is 11% calculated by the change in density [92]. Since the oxide shell will have a much lower thermal expansion for the same thermal excursion, 0.8% for amorphous alumina, the shell will be placed in tension [93]. This can lead to fracture and spalling of the oxide, which is observed under more intense melting conditions. However, at lower laser power densities, the shell is retained. A similar observation was made by Storaska and Howe during in situ TEM experiments of Al-11.6wt%Si particles, where a hot stage was used to heat the particles past the melting point [94]. During these experiments it was reported that 90% of the particles (80-400 nm in diameter) were contained within their oxide shell during melting and resolidificiation, yet no morphology changes in the particles were observed [94]. It was proposed that tangential strain on the amorphous oxide shell was accommodated through a creep mechanism, which aligns with strain rates of amorphous alumina oxide reported later by Mavric, et al. [95]. Although a creep mechanism could help explain how particles observed in this study retain their contiguous oxide shell after laser irradiation, two important distinctions should be made between the study performed by Storaska and Howe and the one performed here. First, the temperature during the in situ TEM experiments performed by Storaska and Howe was slowly raised just above the melting temperature of the Al-Si particles, while the average temperature

reached within milliseconds during the laser irradiation performed in this study is believed to be in excess of a few hundred degrees above the melting point of the particles. Second, the size of the Al-Si particles used by Storaska and Howe were two orders of magnitude smaller than the particles used in this study, and thus contained a much higher shell thickness to radius ratio [94]. For these reasons a direct comparison cannot be made the two experiments, yet a creep mechanism may still explain in part why the oxide shell appears to stay unchanged after laser irradiation in this study.

A second mechanism is hypothesized here based on the rapid regrowth of the alumina oxide, in an air or partial oxygen environment, which may explain how the oxide shell can accommodate the strain induced by the thermal expansion of the particle during the heating cycle. Validation for dynamic oxide regrowth on timescales equivalent to the thermal expansion of the laser irradiated particles in these experiments was observed from recent work performed by Yang, et al., whose in situ TEM experiments captured real-time growth of amorphous alumina over an exposed aluminum surface during deformation [96]. The growth rate was determined to be approximately 0.25 nm/s, at an O_2 pressure of $3.6x10^{-6}$ Torr and room temperature [96]. Using standard expressions for molecular arrival rate in a gas vs. pressure, and the idealized structure of corundum to estimate monolayer densities and thicknesses, the maximum growth rate (the rate associated with complete reaction of all arriving oxygen to form Al_2O_3) is given by $G_{max}(nm/s) = 9.1x10^5*P$ (Torr). For the pressures used by Yang, et al., this predicts G about 10x larger than measured by them, reflecting sluggish reaction/diffusion kinetics at room temperature. For an O_2 partial pressure of 0.1 Torr (more typical of the LBPF environment), the maximum growth rate is $9x10^4$ nm/s. Regrowth of a 10 nm oxide in 1 msec would require a rate of $1x10^4$ nm/s, so the oxygen *supply* is well in excess of what is needed.

Rates are much higher than Yang, et al., both because of the much higher oxygen supply, and because of the much higher temperatures reached during laser melting. Hence it seems quite reasonable that the oxide shell can dynamically heal ruptures and continuously conform to the thermally expanding powder particles during laser heating. Notably, in separate experiments performed in this study (not shown here), a 25 ns pulsed excimer laser resulted in rapid melting of the Al-Cu powder particles, and the oxide shells were often lost since the oxidation rate was unable to respond to the much shorter heat pulse. This led to sintering, wetting of the support substrate, and even "fountains" of molten metal extruding through openings in the oxide.

If the oxide shell dynamically heals during the heating and melting cycle as discussed above, then at the maximum temperature, the shell can be assumed to be strain free. Upon cooling and resolidification, the rapid contraction of the metal particle then places the oxide shell under a state of inward-directed hydrostatic pressure [97,98,99]. This assumes that the liquid metal wets the oxide and does not pull away from the shell as it contracts. Buckling of the shell into the molten metal would lead to the dent or rift features seen frequently in this work. A standard expression for the pressure required to create buckling in a perfect spherical shell is:

$$P_c = \left(\frac{2E}{\sqrt{3(1-\nu^2)}}\right)\left(\frac{h}{R}\right)^2 ,$$

Eq. 3-2

where E is the Young's modulus, ν is Poisson's ratio, h is the thickness of the oxide shell and R the shell radius [100]. Unsurprisingly, thinner shell walls, or larger shell diameters (here, the particle diameter), will buckle more readily [101]. Note that for an oxide shell with E = 300 GPa, ν = 0.21, h = 20 nm and R = 5 μm, then P_c = 5 MPa.

Dewetting of the molten Al to leave a vacuum gap under the oxide shell would not result in buckling, since the external pressure P_{ext} = 1 atm = 0. 1 MPa << P_c. This supports the

contention above that the contractile liquid metal wets the oxide shell and places it under hydrostatic compression during cooling. That said, voids or entrapped gas already present within the particle as a result of being gas atomized may cause pockets to form between the liquid core and the oxide shell (see **Figure 3-13**). This scenario does not appear to be the norm though and is not further considered here.

The standard expression for the radial strains in the thin shell limit, expressed in spherical coordinates, is:

$$\varepsilon_{rr} = \left(\frac{\Delta P \nu}{E}\right)\left(\frac{R}{h}\right),$$

Eq. 3-3

where ΔP is the pressure differential across the shell wall. Equating the strain to the thermal strain, $\Delta\alpha\Delta T$, where $\Delta\alpha$ is the difference in thermal expansion coefficient between the metal and oxide, and $\Delta P = P_c$ from eqn. 1, allows the required temperature change for differential thermal expansion to buckle the shell to be obtained:

$$\Delta T = \frac{2\nu}{\Delta\alpha\sqrt{3(1-\nu^2)}}\left(\frac{h}{R}\right),$$

Eq. 3-4

Taking $\nu = 0.22$ for alumina, $\Delta\alpha = 2.1 \times 10^{-5}$ (alumina vs. aluminum) and the oxide shell thickness to be 10 nm, yields $\Delta T_c = 124/R$, where the particle radius, R, is expressed in μm [93,102]. For example, a powder particle with a 2 μm diameter requires a cooling of 62 ºC from the maximum temperature to produce the critical strain for buckling. This seems eminently reasonable for laser melting, but note that eqn. 1 is well-known to over-predict the critical pressure for buckling by 2-6x due to imperfections in real shells [103]. Hence the required temperature excursion may be only of order 10-30 ºC for buckling to form dents, and even less in larger particles. The data of **Figure 3-8** show that the likelihood of dent formation increases as the particle size, and therefore R/h,

increases (at least until sintering starts to become significant), consistent with predictions of buckling theory.

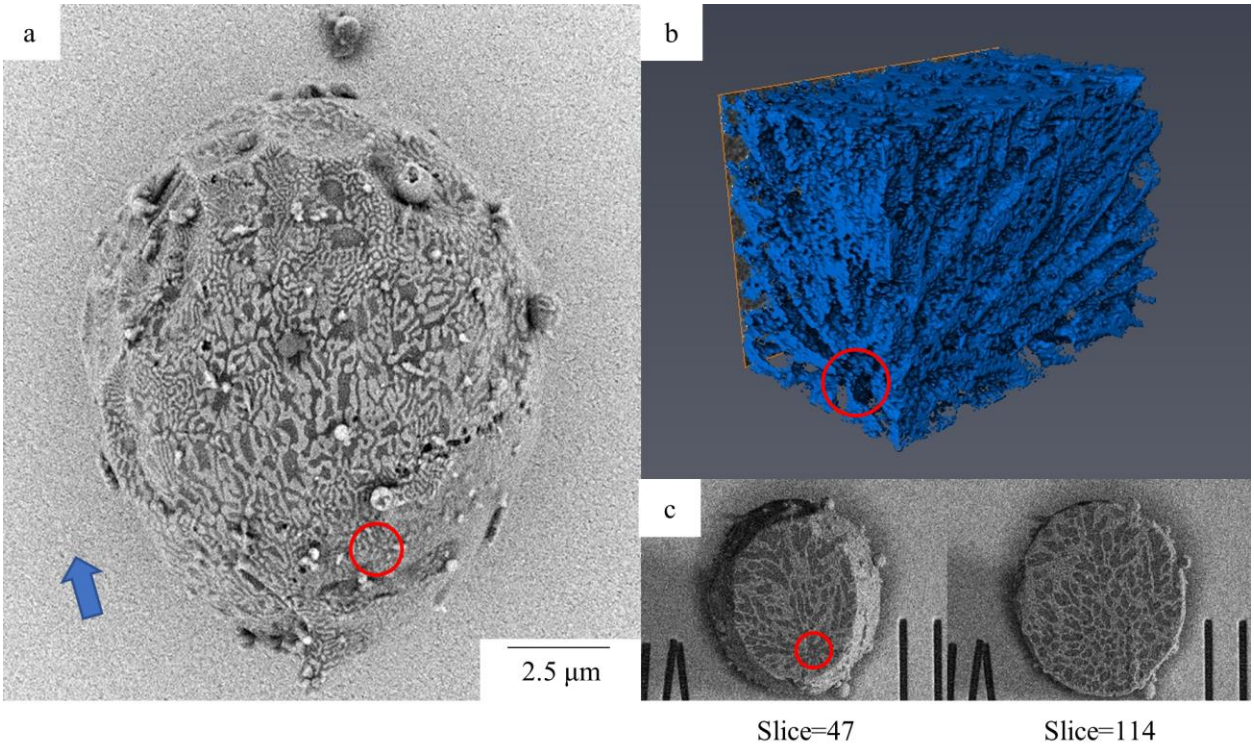

Figure 3-12: Al-Cu particle after laser-melting (a) as shown in Figure 7, with 3D image of dendritic microstructure (b) generated from 114 frames taken during serial FIB cross-sectioning. Each slice removed between frames was approximately 20 nm thick. Slice 47 (c) shows center of dendrite nuclei (red circle). The 3D reconstruction displays the microstructure with the alpha (FCC) phase dendrite removed, allowing the solidification direction of the particle to be determined (blue arrow in (a)). Note that the surface of the particle near the nucleation site is smooth, while the surface opposite contains the highest concentration of collapsed features, supporting the hypothesis that the advancing solidification front can "plow" buckles in the oxide shell ahead of it.

Dent and rift morphologies are "post-buckling" instabilities associated with pressures exceeding the critical value, which are frequently observed in pressure vessels of all shapes and sizes [104]. Dents are envisioned here to form during cooling of the superheated liquid prior to solidification. They can continuously enlarge with thermal contraction as the liquid cools towards the melting temperature (or even supercools below the melting point). They can also enlarge by coalescence of two or more smaller dents [105]. The solidification process likely

influences the formation of dent and rift structures. This may also explain why Storaska and Howe did not observe buckling events in their experiments due to both the smaller ΔT produced during heating, and the larger h/R ratio [94]. Solidification of a liquid within a spherical shell has been shown to produce morphologies analogous to those observed here, as shown by Yu, et al., in their study of microencapsulated phase-change material slurries [106].

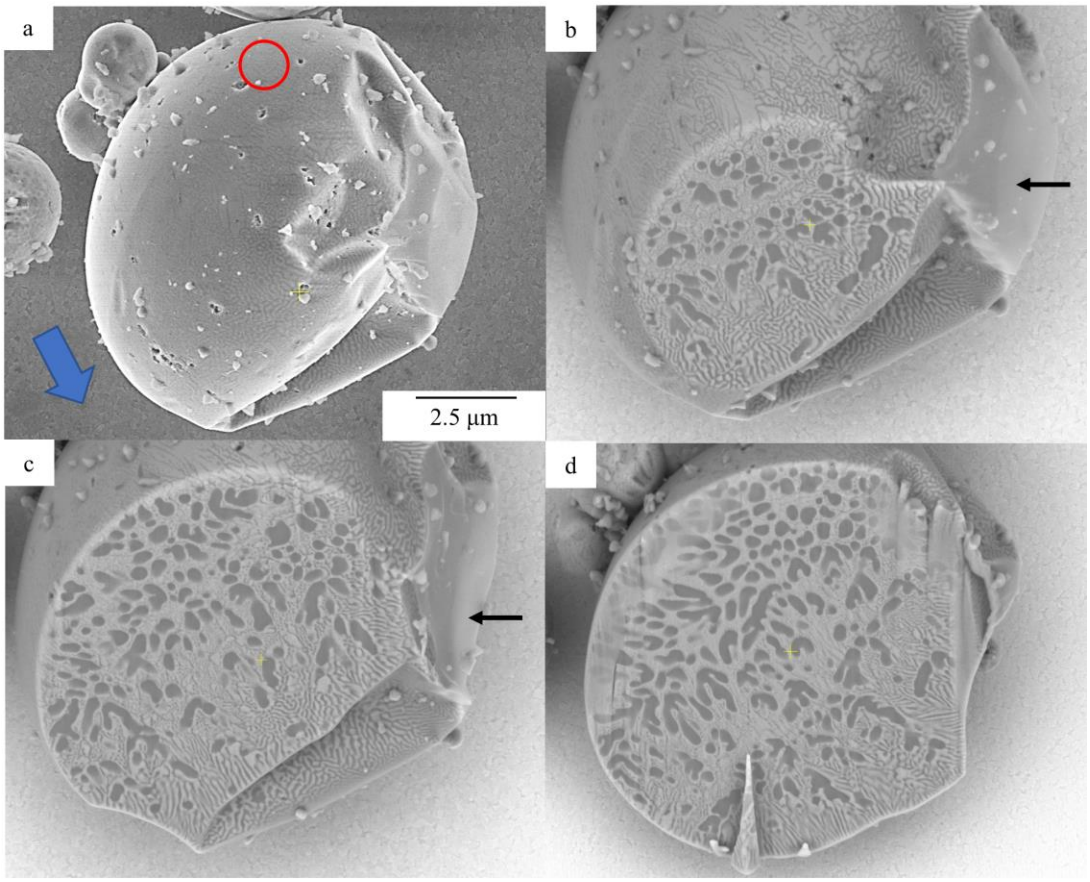

Figure 3-13: Al-Cu particle melted by the 6.5 Watt CW laser (a) and sequential FIB cross-sectioning (b,c,d). The microstructure suggests the solid phase nucleated subsurface in the region indicated by the red circle in (a) and that the solidification front propagated in the direction of the blue arrow. The surface of the particle near the nucleation site appears smooth, while the side the solidification front is moving towards has a high concentration of collapsed features. The black arrow in (b) shows what is believed to be an oxide "tent" that has formed over a dent, perhaps due to gas release from the particle. In (c), an edge of this feature has been milled away, exposing the collapsed metallic surface underneath, and showing how thin the now partly-deflated shell is.

Solidification induces large additional strains due to the density increase and breaks the spherical symmetry ahead of a propagating solid/liquid interface. For example, the advancing

solidification front might force coalescence of smaller dents or buckling modes into larger dents opposite the front. Evidence for this "plowing" mechanism was obtained by serial cross-sectioning as seen in **Figure 3-12** and **Figure 3-13**.The microstructure indicates where solid phase nucleated and the approximate shape of the advancing interface. The external surface of these particles near the solid nucleation site is smooth, while the surface furthest away from the nucleation site (last region to solidify) exhibits a higher concentration of dents. This strongly suggests that solidification plays a key role in the final morphology of these particles.

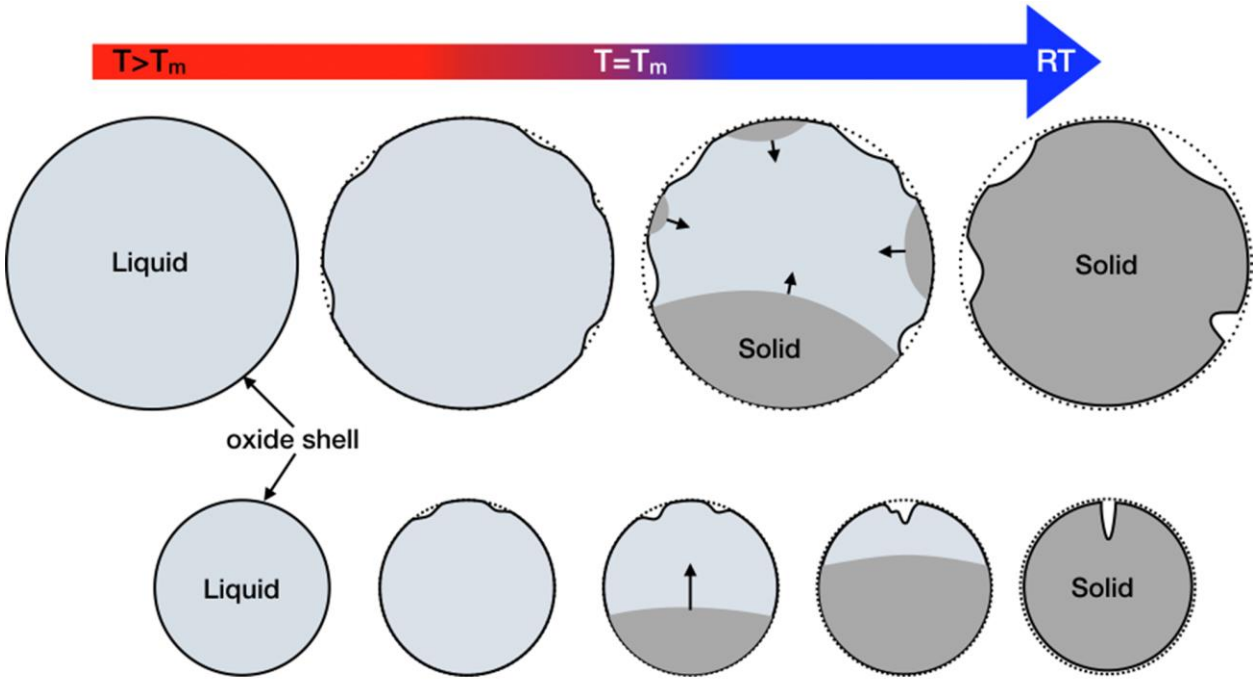

Figure 3-14: Schematic illustration of the proposed mechanism for formation of the dent and rift morphologies observed in irradiated particles. Buckling is shown to occur in shell while particle is still molten due to thermal contraction. These buckles are then shown to coalesce during solidification, being pushed together by the advancing solid/liquid interface. Other factors that may determine variance in irradiated morphology include size of particle, number of nucleation sites, and velocity of the solidification front.

Interestingly, **Figure 3-8** shows that rifts tend to occur more often in smaller particles, which is not expected *a priori* from eqn. (1). Two possible scenarios may explain why smaller

particles are more likely to rift during solidification. First, smaller particles are more likely to contain only a single nucleation event, evident by the many single grain particles found with diameter ranges of <5 μm in this study. The advancing solid/liquid interface breaks symmetry as discussed above, creating more localized stresses in the shell. Smaller particles have a larger h/R value that can allow larger stresses to develop, and in cases when only one nuclei forms, these stresses may concentrate in the shell above the last of the liquid to solidify, leading to catastrophic failure in the form of a rift. A schematic of how dents and rifts may occur in different particle sizes can be seen in **Figure 3-14**. Larger particles, with multiple nucleation sites may solidify on the surface too rapidly for deep rifts to form. The second possible contributor towards skewing prevalence of rifts in smaller particles is a difference in solidification rate that occurs between smaller and larger particles. Because smaller particles will have on average fewer potential nucleation sites, they are more likely to experience greater undercoolings and larger solidifications rate relative to larger particles. An example of a small particle undergoing a rift collapse is shown in **Figure 3-15**, where the rift appears to have occurred during an abrupt change in the solidification rate. A possible explanation for the microstructure and morphology seen in the particle in **Figure 3-15** goes as follows: 1) a nucleation event occurs as indicated in the figure after some undercooling and begins to rapidly advance through the molten particle, 2) solidification halts due to recalescence and rift forms at the solid-liquid interface, 3) previous solidified microstructure is coarsened due to recalescence, 4) columnar dendritic growth occurs at solid-liquid interface, 5) the remaining liquid solidifies as fine eutectic at the edge of the particle.

Further evidence that smaller particles experience a higher undercooling can be observed in **Figure 3-1** where smaller particles (<5 μm) typically have finer length scales in their

solidification microstructure than larger particles. Faster solidification rates imply higher strain rates in the oxide shells, which can enhance tendencies for more extreme buckling [107]. This can again be see in **Figure 3-9**, where catastrophic collapses are observed in the smaller particles. Many of the particles in **Figure 3-9** display an abrupt transition in the microstructure, similar to that shown in **Figure 3-15**. It is concluded that a similar sequence of events is occurring then, where deeply undercooled particles begin to rapidly solidify from a nucleation site, only to be halted by recalescence, coarsened, and then proceed to rapidly solidify [86].

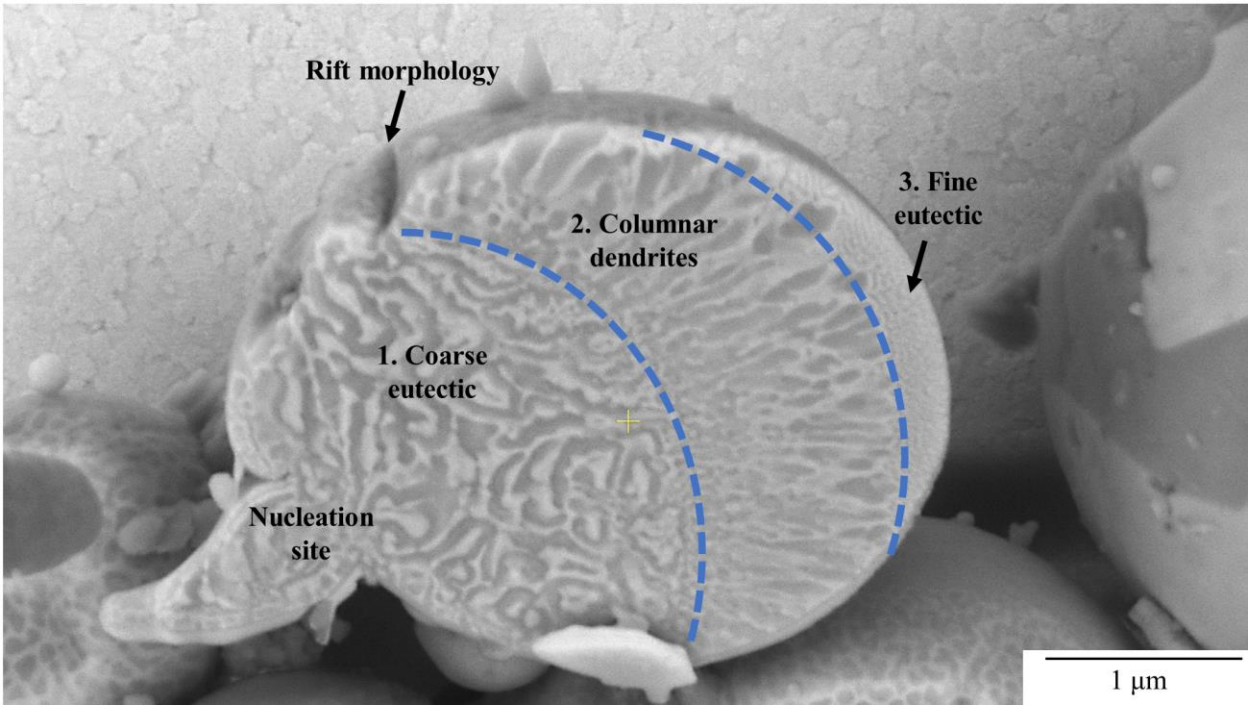

Figure 3-15: Cross-section of Al-Cu particles irradiated by the low power laser. There are three distinct regions of microstructure (roughly indicated by the dotted blue lines), though all eutectic length scales are still finer than the pre-irradiated annealed microstructure. The microstructure suggests that the solid phase nucleated in the particle as indicated. It should be noted that the rift morphology is located at the boundary where the microstructure abruptly changes (black arrow).

While there are other possible explanations for the morphological changes observed here, the large-scale effect of distributed voids in the powder particles is rejected since the pressure on a void would not initiate collapse. Sectioning of as-received particles gave further evidence that

the void volume is insufficient to account for the amount of collapse observed here. Dents in particles could result from local Hertzian contact between adjacent particles during melting. However, SEM micrographs taken before and after laser processing clearly showed that the dents cannot be attributed to local mechanical contact. Laser induced shockwaves and Marangoni effects often can create extreme morphologies [108109110]. However, the oxide entrainment of the liquid is not consistent with this. For example, it is frequently observed that satellite particles survive local surface collapse without ejection or other obvious movement.

3.2.3: Conclusions

The morphological changes occurring in Al and Al-Cu powder after laser irradiation were studied and a mechanism explaining the cause of these changes is proposed. The eutectic microstructure was used to show that the majority of particles that undergo low power irradiation melt and resolidify without agglomeration or sintering, and that this can occur under standard processing parameters during LPBF along the edges of each track. Characterization of particles before and after low power laser irradiation clearly demonstrate that the dent and rift features observed in irradiated particles are morphologies resultant from solidification coupled with buckling of the oxide shell. Further tests with pulsed excimer laser show that different morphologies form when the oxide on the particle is ablated away and dynamic growth of the oxide is impeded. It is thus proposed that the oxide layer around each particle acts as a microcapsule that can prevent sintering while collapsed morphologies form due to thermal stresses that lead to buckling of the oxide shell.

Pertinent to additive manufacturing, these results explain how morphological anomalies may arise in recycled powder feedstocks with robust oxides in lieu of the more commonly

studied agglomeration and spatter defects. Furthermore, it has been shown that a dynamically healing oxide can suppress contiguous melting and even local sintering between particles, specifically along the track periphery where the laser power density is low. Powder particles that are not fully subsumed into the build will deform, and if these particles are recycled, they will impact the subsequent powder rheology, potentially leading to additional build defects. Thus, while larger spatter or agglomerate defects will be removed during sieving, particles with collapsed morphologies will retain sizes equivalent to the virgin powder, causing them to be inextricable from the recycled powder. Therefore, it is believed that these morphology changes may play a critical role in the degradation of recycled powder that has hitherto been overlooked.

3.3: Elemental mixing during in situ alloying of Al and Cu powder during LPBF

3.3.1: Motivation

The LPBF process has shown potential in printing a wide variety of metal alloys, yet the quality of the built parts hinges on the type of powder feedstock used [111]. Gas atomization and plasma rotating electrode process both produce spherical powders that provide high flowability, a necessary quality for the recoating step in LPBF, but only specific alloy compositions are produced by these processes, considered commercial off the shelf (COTS). Custom alloy powders can be made but often require a large starting quantity and high costs [112]. Thus, research in LPBF has been restricted and even disincentivized from exploring nonconventional alloys.

In situ alloying of powder blends within LPBF is currently being investigated as an attempt to alleviate the restrictions in acquiring unconventional powder feedstock. Several research groups have made significant progress in this area, both validating and advancing this approach. One avenue towards new alloys is to start with a conventional alloy powder, and blend

in small additions of other elements. This has been performed in recent studies such as by Krakhmalev, et al., who made small additions of Cu to Ti6Al4V to enhance the antibacterial properties of the 3D printed bio implants, and by Hanemann, et al., who showed that the thermal expansion of AlSi10Mg LPBF built parts could be controlled through various additions of Si in the feedstock powder [113,114]. Other studies like the one performed by Montero-Sistiaga, et al., have shown that small elemental additions of Si to the AA7075 alloy can induce grain refinement when being processed through LPBF and reduce solidification cracking within the build [115,87].

Beyond making minor elemental additions to COTS pre-alloyed powder, in situ alloying is also being researched as an approach to create alloys starting entirely from elemental powder blends. This has been shown to be a viable approach for alloys with both low solute concentration such as Ti6Al4V and high solute concentration such as Al-Cu alloys with 12 to 40 wt% Cu [85,116,117]. Furthermore, a method of screening high entropy alloys has been put forth by Haase, et al., and then followed by Ewald, et al., where blends of over five constituent elemental powders at various compositions were alloyed in situ during LPBF [64,63]. Such prototyping methods that leverage the use of low-cost elemental powders could prove to be invaluable in the development of alloys that are specifically designed to be processed by LPBF. This may be particularly important for many aluminum based alloys, where compositional changes are shown to provide solutions to many of the current processing defects that occur during LPBF [118,119,120].

Although in situ alloying during LPBF greatly expands possible alloy selections, there exist several challenges that must be better understood and overcome before this approach is widely utilized. The recent review by Mosallanejad, et al., outlines six primary difference between elements within a powder blend that must be considered when performing in situ

alloying, including size, melting temperature, reflectivity, viscosity, density, and thermal conductivity [121]. Difference in melting temperatures between elemental powders is one of the most common obstacles to in situ alloying, leading to incomplete melting of one or more of the constituent elemental powders within the build. One of the most common drawbacks to in situ alloying is incomplete melting of one or more of the constituent elemental powders. This arises due to the difference in melting temperatures between elemental powders, and has been observed in both the Al-Cu and the Al-Si systems, where unmelted particles of Cu or Si can be found in the bulk builds [116,122]. Along with this, elemental particles with different size distributions may segregate in the powder hopper or recoater, leading to compositional variations within the built part [123,76]. Further complications in elemental mixing may arise due to the size of the elemental particles within the powder blend, and the dimensions and solidification rate of the laser induced melt pool, with larger and slower melt pools allowing for better mixing.

In this study, in situ alloying of elemental Al and Cu powder is investigated with respect to the particle size distribution within the powder blend. The eutectic composition of Al-33wt%Cu was chosen for all blends so that poor mixing of the elements in the melt pool may be observed through deviations in the eutectic microstructure. Regions in the melt pool that deviate from the eutectic composition by ±3wt%Cu will form either alpha phase (FCC Al) or theta phase (Al_2Cu) dendrites depending on whether the composition is hypo- or hypereutectic [37]. These regions can be distinguished by both the distinct change in microstructure, as well as the difference in Z-contrast as shown through backscattered imaging in a scanning electron microscope (SEM). Using this approach, the degree of mixing in four different powder blends is analyzed with respect to the relative size distributions of the elemental powders used.

3.3.2: Results and Discussion

3.3.2.1: Powder characterization

Elemental powder feedstock was characterized to observe sphericity of particles as well as to obtain particle size distribution. **Figure 3-16** shows the micrographs of the four elemental powders and their size distributions as calculated using ImageJ software. The larger Al powder (Al-2) was specifically developed for use in LBPF by Valimet and was found to have the narrowest particle size distribution as observed in **Figure 3-16e**. The four combinations of these elemental powders resulting in the four powder blends are shown in **Figure 3-17**. In blends 1 and 3 (**Figure 3-17**) the smaller Cu powder (Cu-1) was found to be embedded on the surface of the Al particles after mechanical mixing, most likely due to interparticle impacts or static charge effects. Although blend 3 appears to have a higher coverage of Cu particles on the larger Al particles than in blend 1, the actual wt% of adhered Cu particles is greater in blend 1. In blends 2 and 4 (**Figure 3-17)** no adherence was observed between the Al and Cu particles. These inherent differences in the powder blends lead to differences in the overall elemental distributions within a powder layer during the LPBF process, as will be further discussed in subsequent sections. Characterization of the powders were performed using EDS to ensure that no impurities had contaminated the powder during mechanical mixing as shown in

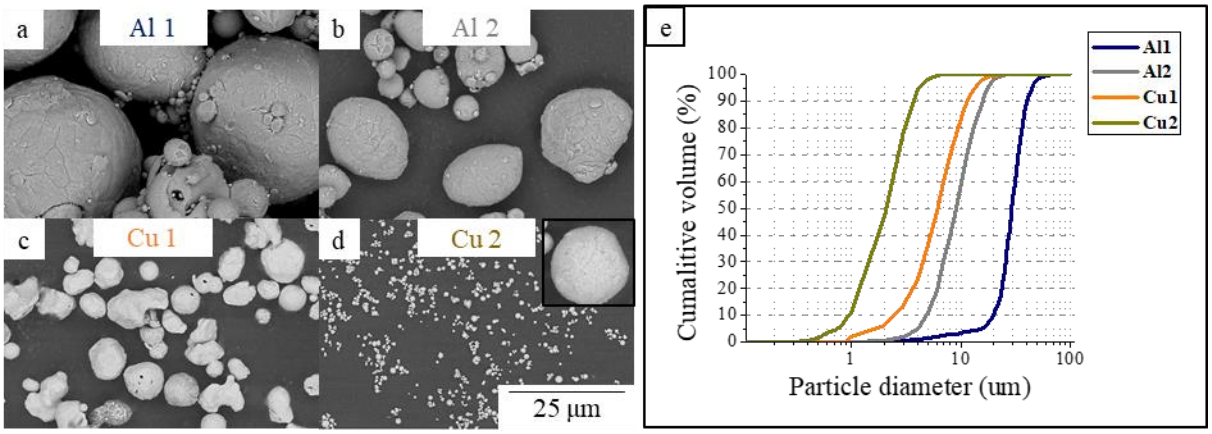

Figure 3-16: SEM micrographs of elemental powder feedstock of Al (a and b) and Cu (c and d) with corresponding particle size distributions taken from areas of particles calculated in ImageJ (e).

Rheology data obtained from the Freeman FT4 rheometer allowed for comparison of powder blends through several different properties. **Figure 3-19a** shows the compressibility of the blends, which can be used as an indicator of powder flowability, although this property alone cannot predict how well the powder will flow during the recoating process in LPBF [124,125]. The shear stress of the powder blends (**Figure 3-19d**) provides a metric that is more comparable with the motion of the particle sliding under the recoater blade, which places the powder both in shear and uniaxial compression. From the shear stress tests, several other properties can also be extracted to characterize the powder. The powder property that most correlates with the flowability is the unitless flow function (FF), which is derived from the ratio of the major principle stress (MPS) and the unconfined yield strength (UYS). Powders with an FF<1 are considered non-flowing while those with an FF>10 are considered free flowing [51]. The difference between the Al-2 (30 µm) elemental powder designed specifically for LPBF and the four powder blends can be clearly seen within this property, with the former having FF = 10.2 and the latter having FF = 3.8-5.4, shown in **Figure 3-19c**. The reason for the decrease in flowability of the powder blends may be attributed to both the strongly bimodal particle size distributions of the

blends as well as a decrease in the average sphericity of the gas atomized Cu powders, especially Cu-2 (6 µm), which was found to have many irregularly shaped particles. Blends of smaller powder sizes are also more prone to absorb moisture when testing in air due to their abundance of surface area, and therefore may flow better within an inert environment then indicated by the rheometry data.

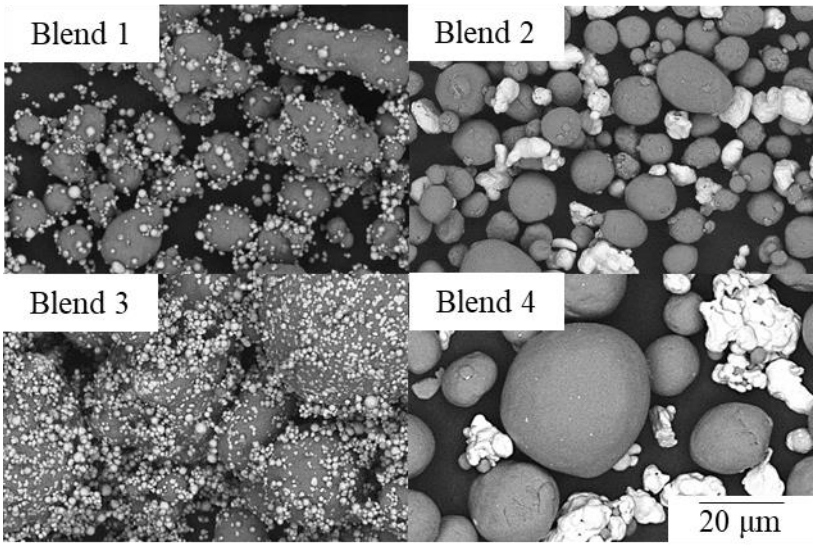

Figure 3-17: Four elemental powder blends of various sizes of Al and Cu powder mixed at the eutectic composition. SEM micrographs were taken after blends were mechanically mixed for 2 hrs. The lighter-contrast particles are Cu.

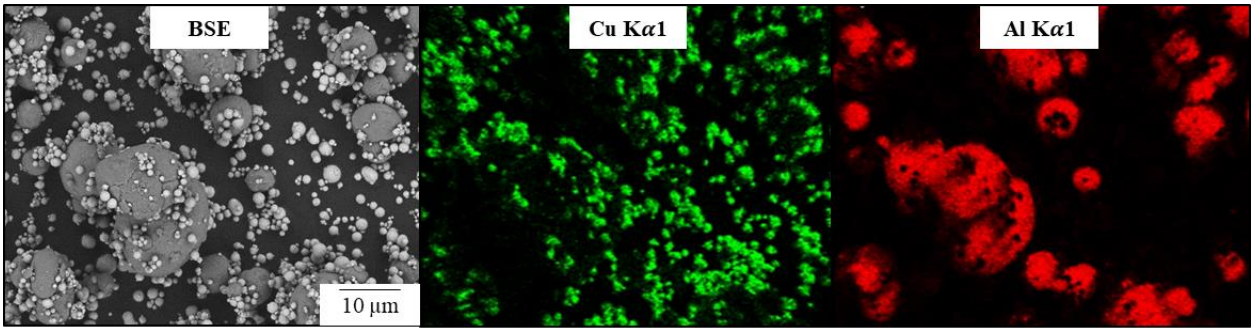

Figure 3-18: EDS characterization of blend 1 powder showing the decoration of the smaller Cu particles on the Al particles.

The flowability of the feedstock powder in LPBF has far reaching consequences, thus maximizing this property when designing elemental powder should be a priority that is balanced

with other desirable attributes such as a homogenous distribution of the elemental powder, and particle sizes that allow for elemental mixing to occur within the melt pool. The powder blends studied in this investigation represent the lower size range of feedstock powder that could feasibly be used in LBPF due to their low flowability, yet trends from the different combinations of size ratios and insight into elemental blend design will be applicable to larger, and possibly more spherical, powder feedstock.

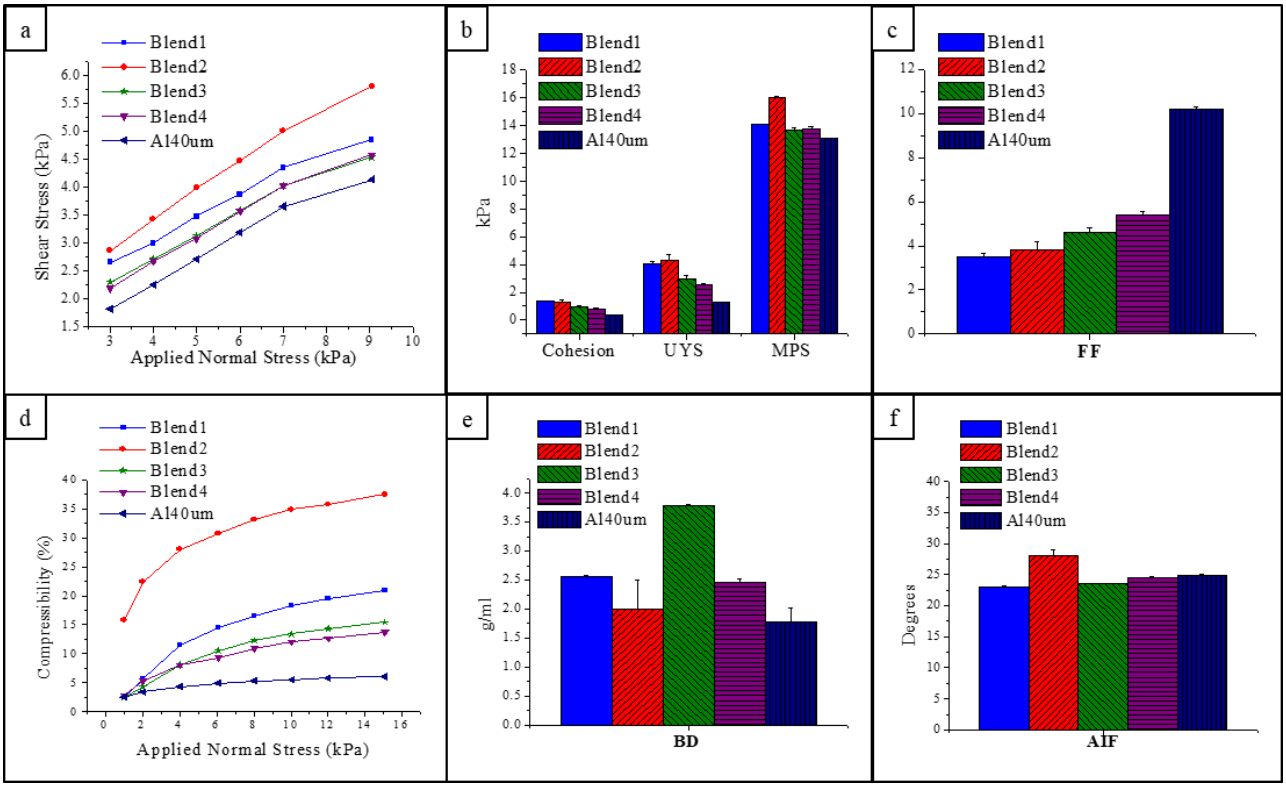

Figure 3-19: Rheology data of powder blends showing the compressibility (a) and the shear stress (d) of the powder. From the shear stress data, several other powder properties may be gained such as the cohesion, unconfined yield strength (UYS), major principle stress (MPS) (b), flow function (FF) (c), bulk density (BD) (e), and angle of internal friction (AIF) (f). The Al (30 µm) elemental powder is plotted with the blends for comparison.

3.3.2.2: Microstructure Analysis

Characterization of the samples built from the different elemental powder blends allowed for a qualitative comparison of the elemental mixing achieved during laser melting. Samples

made from a pre-alloyed powder were used to allow for a comparison of the microstructures. All samples were made using each of the four powder blends at six different laser parameters as shown in **Table *3-1***.

Table 3-1: LPBF laser parameters used to make in situ and pre-alloyed samples.

	50 mm/s	100 mm/s	200 mm/s	300 mm/s
125 W		AM4		
150 W	AM1	AM3	AM5	AM6
200 W		AM2		

Figure 3-20 shows the microstructures of samples made from the four powder blends processed at the AM8 laser parameter (**Table 3-1**). EDS performed on the dark and bright regions of the BSE micrographs confirm that these regions correspond to higher concentrations of Al and Cu respectively, as shown in **Figure 3-21a-c**. Due to the nature of eutectic solidification, deviations from the Al-33wt%Cu composition in the melt pool result in local changes to the nominal lamellar microstructure, where either α-phase or θ-phase dendrites will begin to form, depending on the shift in composition [37]. **Figure 3-21d&e** show micrographs of the hyper- and hypoeutectic regions, where θ-phase and α -phase dendrites are present. It should be noted here that some areas that are high in Cu concentration from the EDS maps, and that appear bright in backscatter micrographs, actually still retain the nominal lamellar microstructure. These areas are usually found close to θ-phase dendrites, and may result from an extension of the hypereutectic region under the surface that is being detected by the interaction volume of both the backscattered electrons and characteristic X-rays. Similarly, dark areas are also seen around many of the α dendrites. Such regions were categorized as part of the overall hyper- or hypoeutectic region, even though there exist no change in the microstructure.

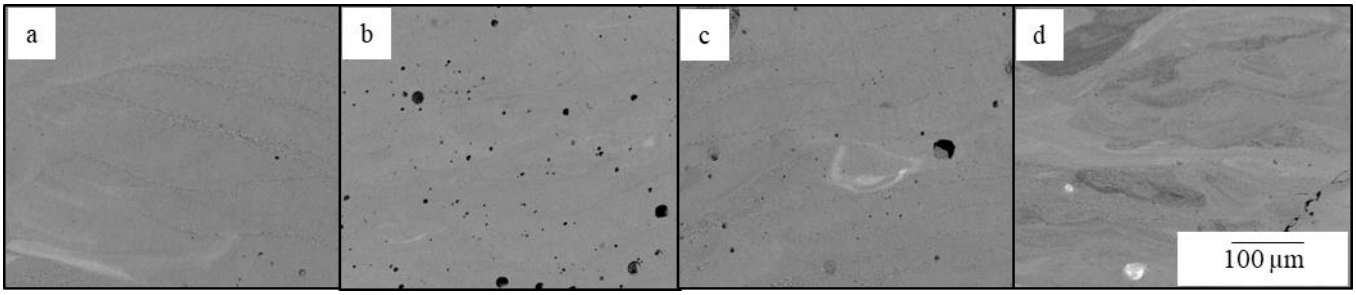

Figure 3-20: SEM Backscattered micrographs of microstructures of samples built from the powder blends 1(a), 2(b), 3(c), and 4(d) all processed at AM8. Bright regions indicate region of high Cu concentration (hypereutectic) while darker gray regions indicate locally elevated Al concentrations (hypoeutectic). Black spots in samples were determined to be spherical pores.

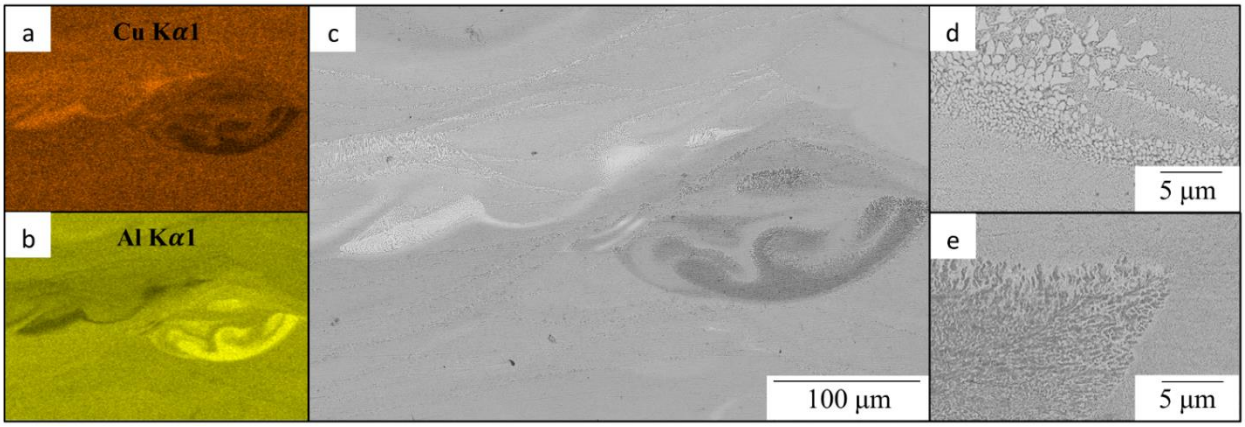

Figure 3-21: SEM EDS maps of Cu (a) and Al (b) in a sample made from blend 4 at the AM2 laser parameter. Light and dark regions in the backscattered micrograph (c) correspond to high concentrations of Cu or Al respectively. Higher magnification micrographs of the Cu and Al rich regions are shown to have (d) hypereutectic and (e) hypoeutectic microstructures.

To quantify the degree of mixing, regions of high or low Z-contrast in the BSE micrographs were measured through ImageJ software. An example of the selection process for a hypereutectic region is shown in **Figure 3-22**, where thresholding is used to select pixels above a certain greyscale level and the selected area is then measured. Because these samples were built layer-by-layer through LPBF, coarsening of the microstructure occurs at the melt pool boundaries, and these are assigned by the software as part of the hyper- or hypoeutectic regions as seen in the numerous fine-scale lines across the background of **Figure 3-22b**. To eliminate this, a minimum area filter was used during the particle analysis process (**Figure 3-22c**).

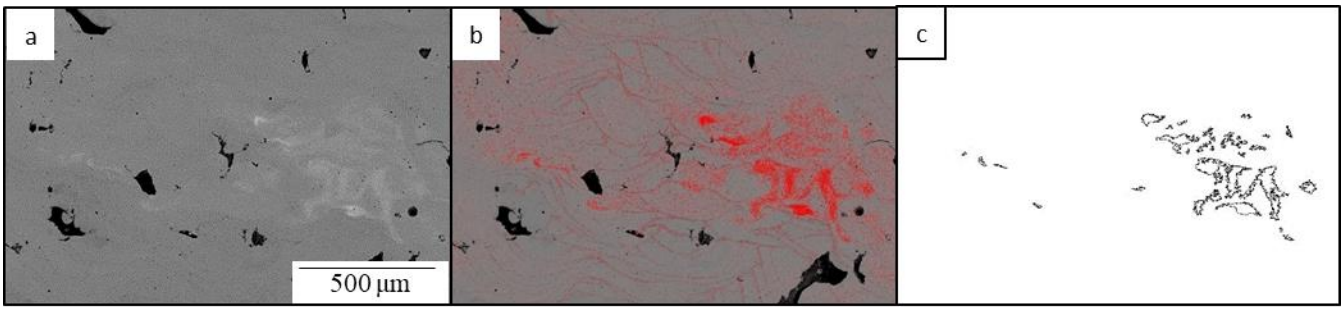

Figure 3-22: Example of a hypereutectic region in a BSE micrograph (a) being selected through thresholding (b) and then quantified, using ImageJ (c).

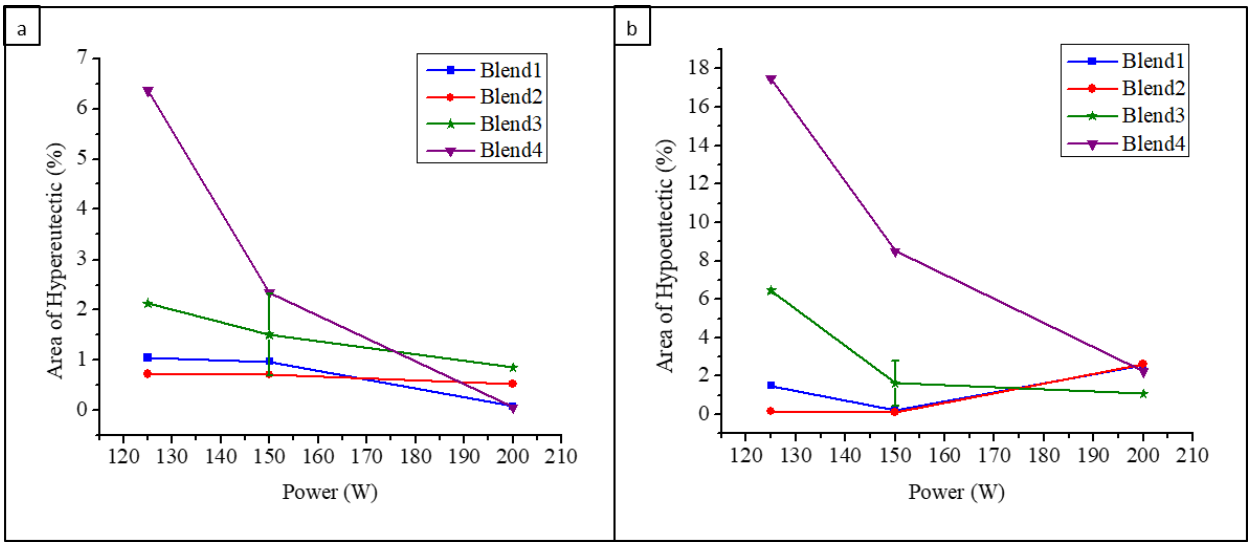

Figure 3-23: Quantification of hypereutectic (a) and hypoeutectic (b) areas in samples processed from the different powder blends at increasing powers. Error bars were placed on one of the data points (blend 3, 150 W) to show an approximate range of uncertainty of this analysis based on thresholding variability.

Trends in the percentage of hyper- and hypoeutectic areas in samples processed with the different powder blends at increasing powers can be seen in **Figure 3-23**. Blend 4 had the highest percentages of hyper- and hypoeutectic areas, which implies the lowest degree of in situ mixing for this blend. However, mixing of blend 4 improved markedly with increasing power. In

general, the results from the different blends tend to converge at the higher powers. At 200 W, the area percentages of the hypereutectic regions were from 0-1%, while the hypoeutectic regions converged in the range of 1-3%. **Figure 3-23b** shows that samples made from blends 1 and 2 appear to exhibit worse mixing a laser power of 200 W vs. 150 W. Keyholing was observed to occur in the samples when processed at 200 W, forming a deep, narrow melt pool that results in more intermixing with the aluminum base plate. In blends 1 and 2 this effect is more evident since good mixing was already occurring at lower powers. This also explains why such a trend is not observed in the percentage of *hypereutectic* areas in the same samples.

The stronger dependence of mixing on increasing laser power observed in blend 4 may be explained in part by the larger powder sizes. Coarser particle size requires larger melt pools to envelop a statistically representative number of particles, in order to achieve the average liquid composition that is on or near the eutectic. This requires a very thorough mixing of the elemental powders, and is facilitated by use of smaller powder diameters. In particular, when the melt pool dimension is only a factor larger than the mean particle size, severe local fluctuations in the local blend composition are likely. Additionally, a smaller powder diameter size also reduces the diffusion distance between alloy components within the laser melt pool. Lee and Cahoon provided experimental data showing the interdiffusion coefficient of copper in liquid aluminum to be 8.39×10^{-9} m^2/s, implying a solute atoms diffusion length of approximately 4 μm in a 200 μm melt pool, assuming a laser scan velocity of 100 mm/s [126]. However, the length scale of mixing is unlikely to be dictated solely by diffusion due to convective and Marangoni currents within the melt pool. Nonetheless, the size of the particles will play a role in mixing efficacy within the transient liquid, especially as the size of the melt pool decreases at lower laser powers. Taken together, these considerations show that even small degrees of powder segregation within

powder blends that use larger particles (>30 µm) will adversely affect the in situ alloying much more than in blends with a smaller average powder size.

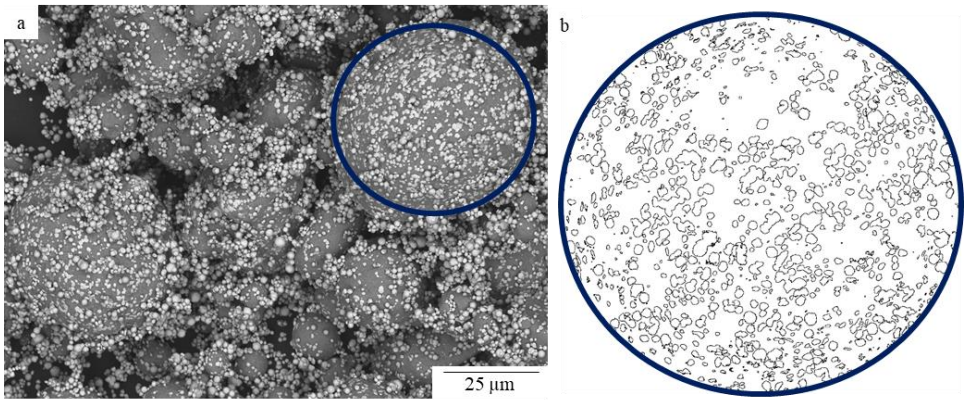

Figure 3-24: An example image of blend 3 that was used to calculate the area coverage of Cu particles on the larger Al particles (a). Image of particle is again shown after post process analysis using imagej, where the software has outlined all of the Cu particles based off of thresholding (b).

A large degree of chemical segregation of the elemental powders within the powder layer, i.e. groupings of either Al-Al or Cu-Cu particles greater than approximately 100 µm in diameter, can cause the composition of the melt pool to diverge from the average composition, producing local hypo- or hypereutectic regions. Coarser powders (> 30 µm) are more prone to statistical fluctuations in local powder composition in this size range due to the fact that fewer particles are needed in a group to reach these dimensions, as observed with blend 4. Furthermore, two types of mixing may occur due to the differences in sizes of the elemental powder – one is the standard mixing of the independent powder particles, while the other type of mixing is via mechanical embedding, wherein minority (by weight) Cu particles are joined to the majority Al particles by mutual impact to form Hertzian contacts. The more this latter type of mixing occurs, the less likely it is that large amounts of free powder segregation can occur. Mechanical embedding will be less effective for larger Al particles as these have a lower surface area to volume ratio, and as such will allow fewer relatively smaller particles (2 um Cu) to be embedded

on their surface. A rough estimate of the wt% of Cu particles that were embedded on the surface of the 30 µm Al powder was made through the following equation:

$$wt\%\ Cu = \frac{N_{Cu}V_{Cu}\rho_{Cu}}{V_{Al}\rho_{Al}} = 4C_{Cu}\left(\frac{\bar{r}_{Cu}\rho_{Cu}}{\bar{r}_{Al}\rho_{Al}}\right)$$

Eq. 3-5

Eq. 3-5 takes the total mass of the surface embedded Cu to be the number of embedded Cu particles, N_{Cu}, times the volume of each times the density, ρ_{Cu}, and normalizes this by the mass of the Al particle. The final expression makes the simplifying assumption that Cu particles of the mean size in the original powder are embedded at constant mass into an Al particle of the mean size. The final expression contains C_{Cu}, which is the average area fraction of Cu particles on the larger Al particles. By analyzing micrographs of blend 3 with ImageJ software, the average areal coverage of the Cu (2 µm) particles on the Al (30 µm) particles was found to be 14%. An example micrograph for this analysis is shown in **Figure 3-24** along with the software selection of the Cu particles based off of the contrast in the image. These embedded Cu particles were estimated to be hemispheres since only the flat surface of the particles could be seen. Thus, the average composition of Cu embedded in the Al particles in blend 3 was found to be 12.2wt%. This suggests that a large amount of the Cu (2 µm) was free within the elemental blend to agglomerate. In contrast, the smaller Al (9 µm) powder used in blend 1 contained much more surface area for the Cu (2 µm) particles to adhere to. As such, even though only 9% of the surface area of the Al (9 µm) particles were covered with Cu particles, this amounted to 26.6wt%Cu, suggesting that much less Cu (2 µm) particles were available to agglomerate within the blend. When regarding the liquid mixing occurring during laser melting of blends 1 and 3, the Cu not embedded into the larger Al particles may tend to agglomerate within the blends,

leading to regions of both hyper- and hypoeutectic compositions within the melt pool which may not fully homogenize before solidification. Because it was shown that blend 3 has a smaller wt% of embedded Cu particles than blend 1, it is likely that this is the cause of increased hypo- and hypereutectic regions within samples made from blend 3 (**Figure 3-23**).

It should be noted here that the manual recoating used in this study may provide results that differ slightly from autonomous builds in terms of creating an even distribution of the elemental powders in each layer. Yet the manual recoating method should provide optimum results for powder distribution for two reasons. First, the application of the powder blends in the manual recoating process greatly reduces powder transport distance, allowing less opportunity for elemental particles to segregate based on density, while the autonomous method requires the powder to travel through several feet of tubing from the hopper to the recoater. Second, the manual recoating method allows for visual inspection of each powder layer applied to the build, ensuring that large gaps in the powder layer may be detected and remedied by a repeated application and leveling of the powder blend. Thus, if elemental segregation occurs in samples built through the manual recoating method, it is very likely that similar or worse results will be found in samples built through the autonomous recoating method.

3.3.2.3: Analysis of mixing through hardness measurements

Vickers microhardness measurements were used as a complementary characterization method to evaluate the local variations of the mechanical properties across a sample. In the Al-Cu system, the tetragonal θ-phase is harder than the FCC α-phase. In the two-phase eutectic lamellar microstructure, hardness will increase as the spacing between the phases decreases. Thus, the coarse α dendrites of the hypoeutectic regions will give a lower hardness value then the

fine lamellar microstructure of the eutectic composition, due to both the length scales of the microstructure as well as the lack of the θ phase present. In regions of the sample that are hypereutectic, it can be expected that the hardness value will be equal to or greater than the surrounding eutectic microstructure. The average diameter for an HV (0.2) indent in these samples was approximately 50 μm, which in principle would provide a high enough spatial resolution to detect hyper- or hypoeutectic regions with areas on the order of 100 μm^2 (**Figure 3-20**). Because coarsening occurs at the melt pool boundaries, the hardness was found to decrease by ~ 50 HV (0.2) when the indenter was centered on these features. Measurements were thus taken in between these boundaries whenever possible.

Figure 3-25 shows the average hardness values for each sample processed from the four different powder blends with their associated error. The average hardness values of samples built from a pre-alloyed powder are also shown (in black) for comparison. Because the solidification of the microstructure occurs at different rates from the bottom of the melt pool to the top due to the curvature of the solidification front, the interlamellar spacing becomes finer near the surface of the melt pool, and thus the hardness can be expected to increase with the finer microstructure. Lei, et al.,measured this variation of hardness to be on the order 1 GPa within a laser melted Al-Cu eutectic sample through the use of a nanoindenter. The variance in hardness seen in the samples made from the pre-alloyed powder, which contained no hyper- or hypoeutectic regions, was found to be approximately 50 HV (~490 MPa), which may be the result of the using a microindenter in this study rather than a nanoindenter.

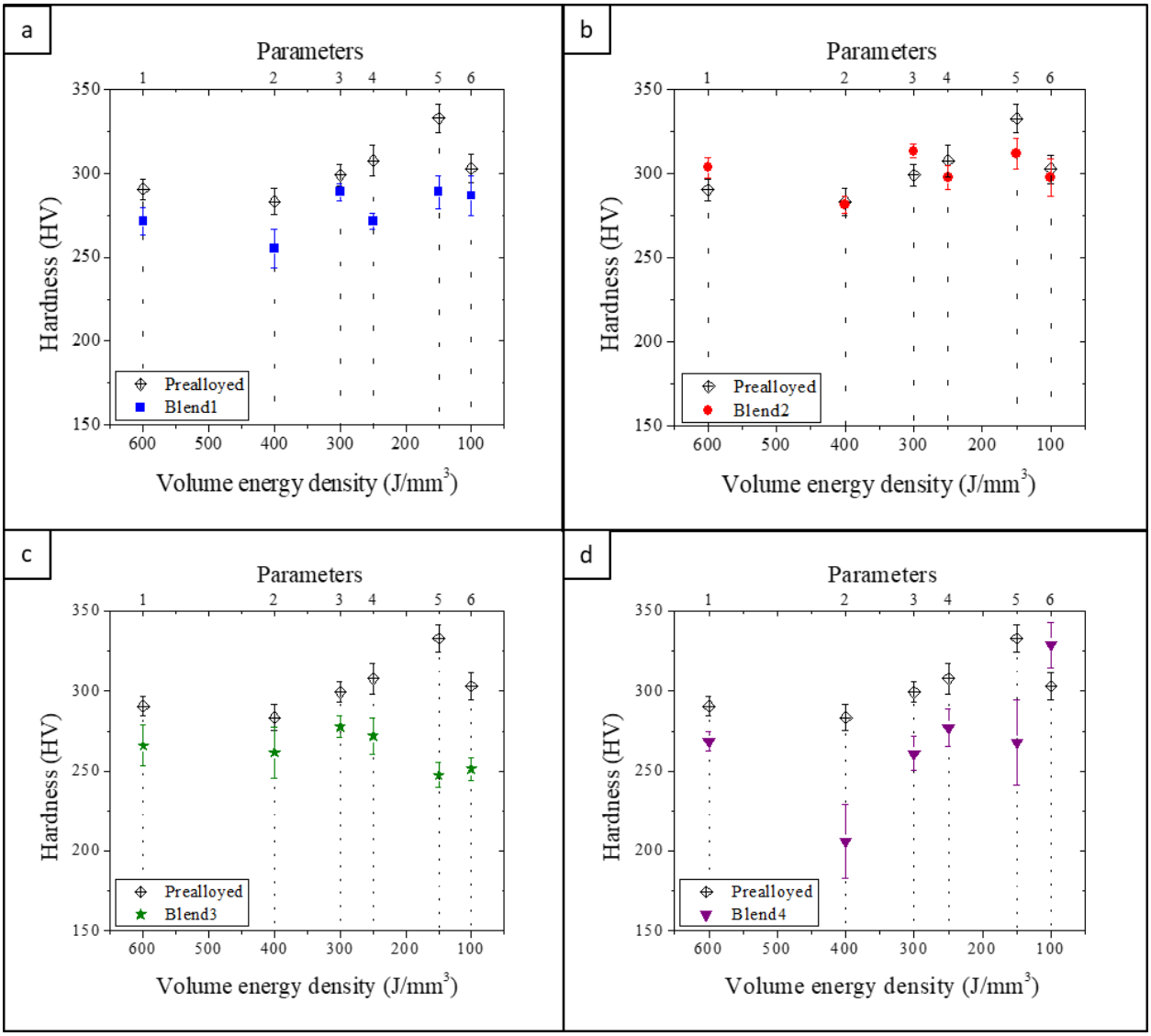

Figure 3-25: Hardness distributions of samples process at the six laser parameters for powder blends 1-4 (a-d). Hardness values for samples built from the pre-alloyed powder are overlaid on all graphs for comparison. Parameters are arranged from highest to lowest energy density (J/mm^3)

Variations in hardness between the pre-alloyed samples are largely attributed to the different laser velocities used within this parameter set. Higher laser velocities cause higher solidification rates within the melt pool which decreases the lamellar spacing. This refinement of the lamellar spacing occurs up to a peak hardness at 200 mm/s, after which increases in the laser velocity cause the lamellar microstructure to transition into a fine dendritic like microstructure [37]

These changes in the microstructure caused by varying laser velocity are most prominent near the surface of the melt pool, where the solidification rate is nearer to the laser velocity, but diminish lower in the melt pools due to the dependence of the solidification rate on the curvature of the solid-liquid interface as discussed earlier. Thus, difference in hardness between samples depends on where the microhardness test was taken within the melt pool. Even so, a trend can be seen in the max hardness between samples, with AM2 (50 mm/s, 150 W), AM5 (100 mm/s, 150 W) and AM5 (200 mm/s, 150 W) having increasingly hard microstructures, while AM6 (300 mm/s 150 W) decreases in max hardness most likely due to the transition from the fine eutectic to a fine dendritic microstructure.

The best overlap of the hardness distributions from the samples made from pre-alloyed powder and the samples formed by in situ alloying can be found in blend 2, while the worst overlap, and widest hardness distributions, are found in blend 4. This trend in the data correlates with trends in the structural inhomogeneity determined from image analysis of the hyper- and hypoeutectic regions (**Figure 3-23**). All powder blends show a relatively good correlation to the hardness of the pre-alloyed powder at the processing parameter with the highest energy density (AM1) and that this correlation worsens in parameters with lower energy density, specifically in blends 3 and 4.

The porosity of these samples should also be taken into consideration, both when considering the hardness values, as well as in terms of the overall processability of the powder. The relationship of the hardness and the porosity of the samples appears to not be directly correlated, as the samples made from blend 4 showed the widest range of hardness values, while in **Figure 3-26** it is shown to have the least amount of porosity for the majority of the parameters. Blend 2 in contrast had some of the smallest ranges of hardness values, while having

some of the highest porosity of the blends. In regards to the processability of the powder, it is difficult to discern any clear trends relating to the porosity of the bulk samples and the size of the powder blends they were built from.

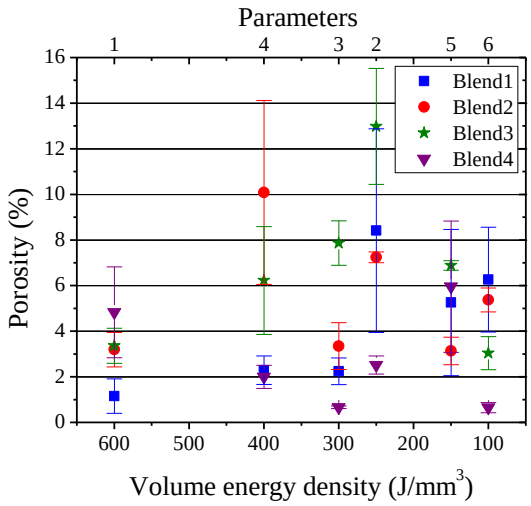

Figure 3-26: Porosity of samples built from all four elemental powder blends. Measurements were made by calculating the area fraction of porosity in cross-sections of each sample as observed through SEM characterization. The average of three measurements per sample are shown along with the corresponding error bars.

A few distinctions may be made between the blends though, such as blend 4 appears to have the lowest porosity across the parameter range. This could perhaps be related to the flowability of blend 4, as less clumping within the powder layer could produce a denser part. The higher energy density parameter (AM1) appears to produce samples with the lowest porosity for all four blends, although blend 4 trends to even lower porosity at lower energy density parameters. Trends may also be obscured by the different types of porosity that are occurring. For example, lack of fusion pores may be the cause of high porosity at lower energy densities, while keyholing porosity may be present at higher energy densities. Further fine tuning of the processing parameters may yield more fully dense samples for each of these powder blends, with such

features as hatch spacing or laser spot size that could be adjusted to decrease lack of fusion porosity within the builds.

3.3.2.4: Correlation of powder distribution and in situ mixing

In order to determine whether poor mixing was occurring in the line scans due to segregation of powder or due to particle size, SEM micrographs were taken of a monolayer of powder blends before laser irradiation and after. From these images it could be observed whether hyper- or hypoeutectic regions were forming in the melt pool due to powder size, or segregation of elemental powder. To ensure no dilution of elements in the melt pool, an Al-Cu eutectic substrate was used. The surface of this substrate was laser processed before the powders were applied to ensure that the coarse eutectic microstructure did not contribute to elemental segregation in the melt pool. **Figure 3-27** shows before and after image of line AM1 scanned over powder blend 4, and an area where a small hypoeutectic region is visible. This is most likely due to the high concentration of Al particles in that region of the powder layer (blue circle in **Figure 3-27a**). The majority of the line scan shows lamellar eutectic microstructure, indicating the larger powders still allow for good diffusion of elements in the melt pool, but that small segregations of the powders (clumps of 5-6 particles) will produce small regions of off eutectic compositions. Powder layer of blend 3 is shown in **Figure 3-28** both before and after line scans. This powder contained small Cu particles embedded on the surface from ball milling, thus preventing segregation. Yet the amount of Cu on the Al particles alone is not enough to reach the eutectic composition. Thus, in this sample, the smaller Cu particles that were not embedded in the Al particles were separated from the larger particles by the water, leading to an

over powder composition that was below the eutectic point. This can be clearly seen by the microstructure of the laser track as seen in **Figure 3-28c**.

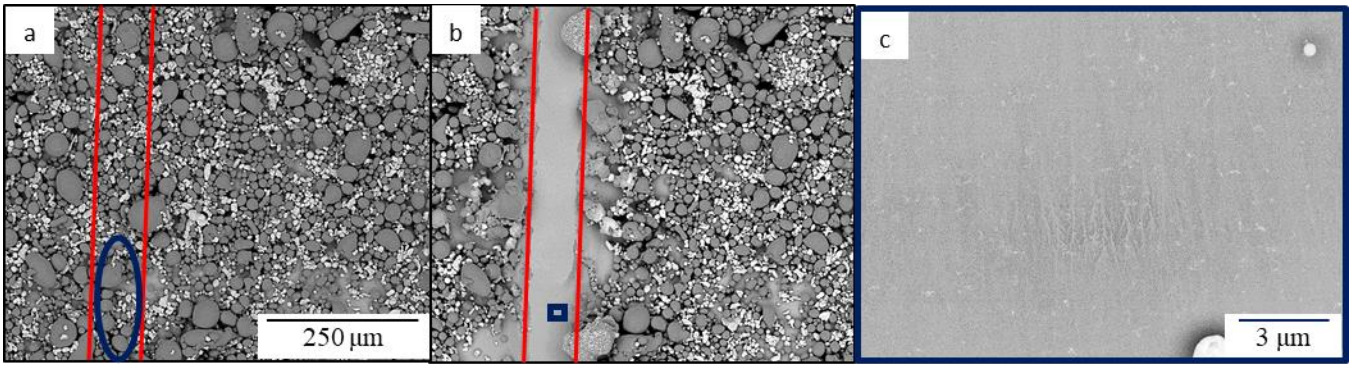

Figure 3-27: Before (a) and after (b) images of line AM2 of powder blend 4, with close up of melt pool showing slight hypoeutectic region in melt (c).

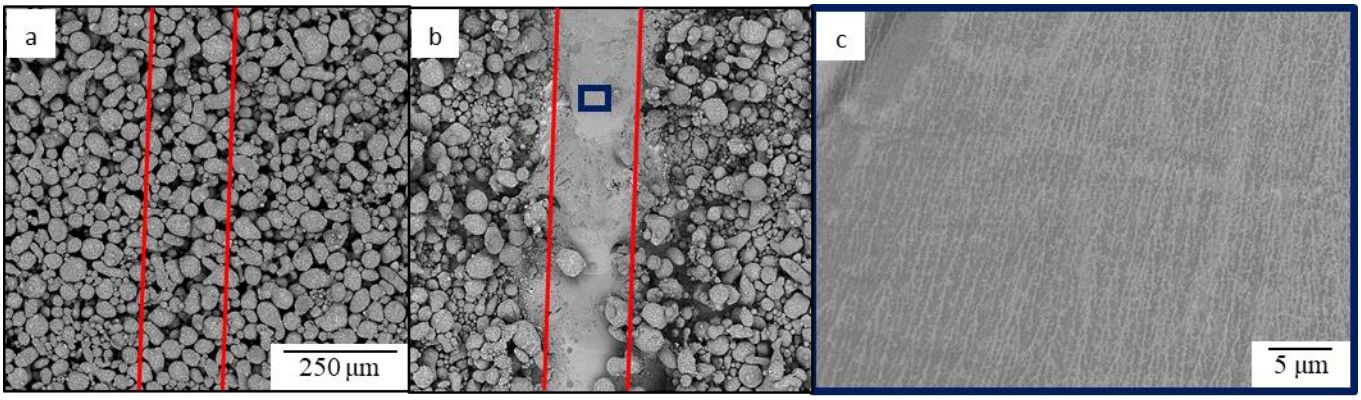

Figure 3-28: Before (a) and after (b) images of line scan AM2 on powder blend 3, with majority of line scan showing hypoeutectic microstructure (c).

3.3.3: Conclusions

The in situ alloying of Al-33wt%Cu was studied in order to determine the effect powder feedstock size and processing parameters have on the mixing of the elemental powders during LPBF. The solidification microstructure of this eutectic alloy was used to assess the degree of mixing that occurred within each sample. This was performed both quantitatively through the use

of SEM and image analysis and qualitatively through the use of Vickers microhardness testing. Significant results are summarized through the following:

1. Measurements of local compositional fluctuations within an Al-Cu eutectic alloy processed through LPBF in situ alloying have been performed using the eutectic microstructure as an indicator of variations of the solute concentration of up to a few weight percent. This technique allowed for both the size and location of these compositional fluctuations to be readily observed, as well as a method to quantify what percentage of the sample was off the desired composition with the help of image analysis software
2. The particle size distribution of the blends was shown to be directly correlated with the degree of compositional homogeneity that existed in the built samples across a range of processing parameters. Particle sizes that are customary to the LPBF processing method were shown to produce large regions of compositional fluctuations, while powder blends with smaller size distributions produced samples with only small regions of compositional fluctuations.
3. Particle decoration in powder blends was studied in an attempt to reduce dry segregation of elemental powder, with limited success, due to the large amount of solute concentrations in this alloy. Small Cu powder (2 μm) that did not adhere to the larger Al particles readily clumped, and were most likely the cause of hypoeutectic regions within blends 1 and 3.

These results help lay the groundwork for a rational design of elemental powder blends that optimizes mixing during in situ alloying within a given set of laser parameters.

3.4: Analyzing melt pool instabilities through eutectic interlamellar spacing

3.4.1: Motivation

The formation and solidification of individual melt pools during the LPBF process plays a determining role in the defects, microstructure, and surface roughness of the finished part [109]. As such, understanding the solidification rate and any fluctuations that occur as the melt pool is freezing is necessary to understand the properties of the built part as a whole. Furthermore, if the cause of fluctuations within the solidification of the melt pool are ascertained, then efforts to prevent or control these events could be pursued. Yet oscillations within the melt pool, let alone the solid-liquid interface, are difficult to observe even with high speed cameras due to the length scale and rapid movements of the melt pool [128,129]. High speed X-ray imagining has been shown to be useful in observing melt pool dynamics during laser melting, but such experimental set ups require access to synchrotron irradiation sources, and thus bottle neck research in this area [62,130].

An alternative approach to measuring fluctuations in melt pools may come from using eutectic microstructures to record the solidification history. Due to the specific relationship that occurs between the lamellar spacing and the solidification velocity, analysis of the microstructure can be used to determine the solidification rate of any point within the melt pool. Along with this, fluctuations in the solidification of the melt pool may induce what is known as "banding", where periodic structures form perpendicular to the growth direction, outlining the melt pool geometry at specific instances in time [58]. Such bands form in a variety of ways, including solute build up in front of the solid-liquid interface, or convection instabilities within the melt pool, but have also been correlated with external irregularities in the processing method [131]. For eutectic alloys, these band often appear as a brief coarsening of the microstructure, suggesting fluctuations in the melt pool solidification velocity [58]. Such features could provide

insight to any irregularities that may be present during the LPBF process if the causation of the banding phenomenon can be fully understood.

Banded microstructures have recently been shown to occur in several alloys processed by LPBF, yet their causation has not been fully investigated [132,133]. Performing research in this area then could provide guidance as to why these bands are forming, and the relationship they have with the melt pool dynamics. Banding of the Al-Cu eutectic system has previously been studied and thus stands as an appropriate model system to better understand why banded microstructures form within LPBF [58,134]. Here, banding microstructures that form as a result of melt pool oscillations are investigated in the Al-Cu system with specific attention to external factors that may be involved. Correlations between mechanisms that cause ripple formation, and oscillations in melt pool depth are also closely examined.

3.4.2: Results and Discussion

3.4.2.1: Correlation of banding and microstructure

Banding was first observed in multi-layer line scans samples built through LPBF with pre-alloyed Al-Cu eutectic powder. Banding structures were characterized as periods of coarsened microstructure that extended between melt pool boundaries. Yet, due to the variation of the melt pool depth caused by the uneven topology and absorption of the feedstock powder, melt pool boundaries at times overlap within the sample, making it more difficult to distinguish banding when it occurs. An example of this is shown in **Figure 3-29** where a melt pool boundary found between layers of the LPBF built sample is shown at the bottom, while two bands appear to form from a partially shown melt pool boundary to the left. Interpretation of the 3D geometry of the melt pool boundary and the banding structures can be difficult especially in multi-layered

samples where multiple melt pool geometries are overlapped. Thus to simplify the system, single track line scans were made within a cast bulk Al-Cu eutectic sample at parameters equivalent to what would be performed for an LPBF build. The banding microstructure was thus studied in cross-sections and on the surface of these samples, allowing correlations of the banding events and the original microstructure to be made.

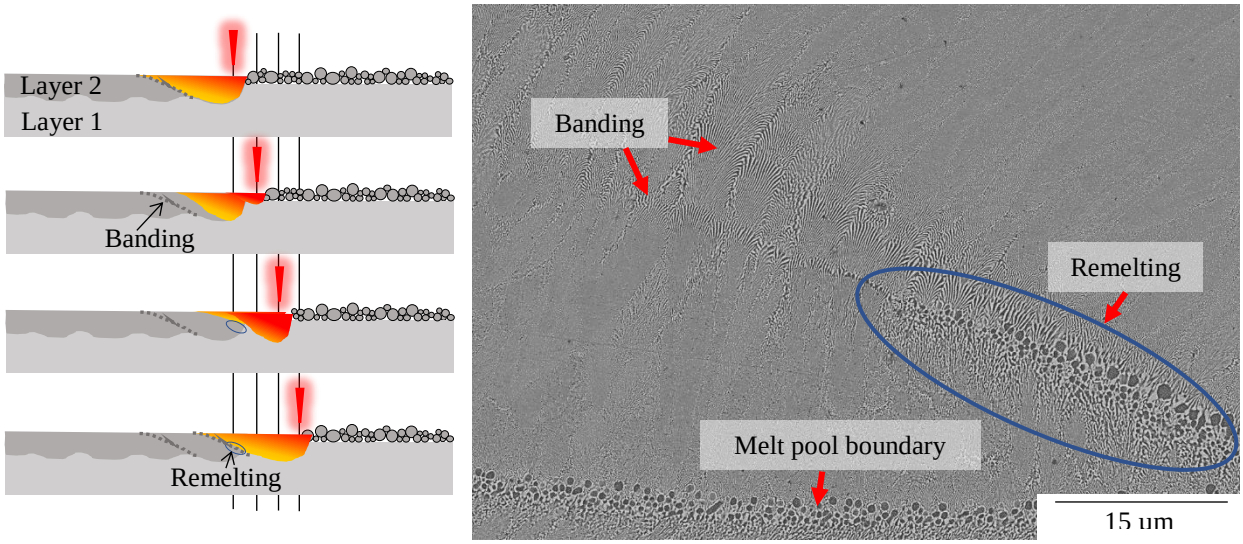

Figure 3-29: BSE micrograph of melt pool boundary and banding phenomenon occurring within a longitudinally cross-sectioned LPBF built Al-Cu eutectic sample. Note how the distinction of bands and MPBs can be blurred due to the many over lapping MPBs within the sample.

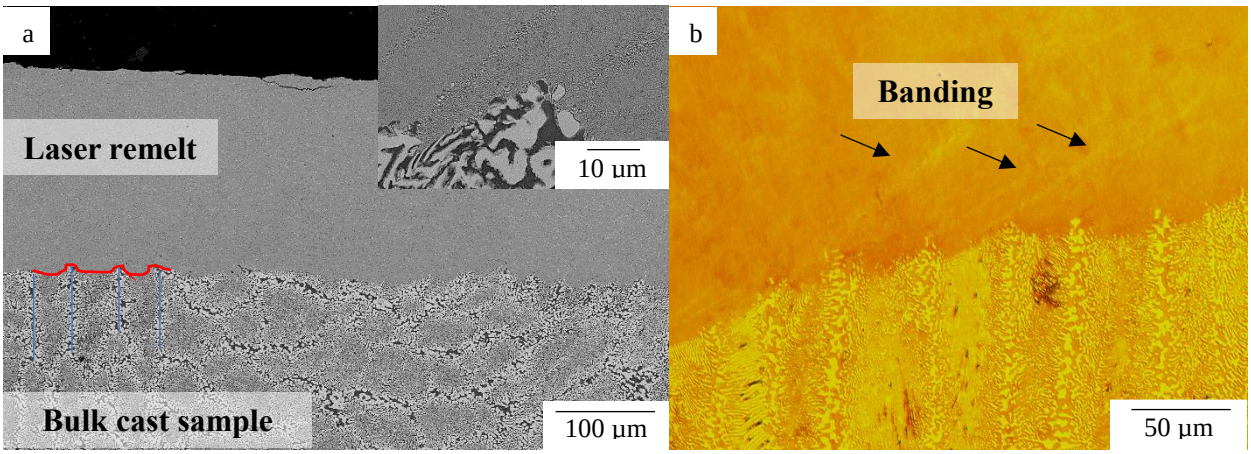

Figure 3-30: Longitudinal cross-section of laser remelt in bulk Al-Cu eutectic sample. Melt pool depth (red line) appears to correspond to bulk microstructure where it is deeper in regions of fine eutectic, and shallower in regions of coarse eutectic (blue

lines) as shown in (a). Banding appears to correspond with the shallower melt pool depths and coarser eutectic microstructure, as shown in the inset of (a) and in the optical micrograph shown in (b).

It was shown that in higher power line scans (~200 W), the melt pool depth correlated with the bulk microstructure underneath the melt pool**. Figure 3-30** shows the melt pool depth increasing over the finer regions of the bulk microstructure and decreasing over the coarser microstructure between the large colonies in the cast sample. A possible explanation for this may be that phonon scattering is occurring within the finer microstructure of the bulk sample due to the higher density of interfaces there, causing the thermal conductivity to be locally lower there than in the coarse microstructure between the colonies. This would cause higher thermal gradients to build up above the fine microstructure, possibly leading to a deeper melt pool at these localities. A recent study by Marasli and Bayram showed that the thermal and electrical conductivity of the Al-Cu eutectic system changed with the interlamellar spacing of the microstructure [135,136]. The thermal conductivity was shown to decrease from 236 W/Km to 200 W/Km when the interlamellar spacing was reduced from 4 μm to 0.4 μm. Banding was observed occurring at the sudden changes in melt pool depth, often at the regions of coarse bulk microstructure between the colonies. This is shown both in the inset in **Figure 3-30a,** and in the corresponding optical micrograph. The correlation between the change in melt pool depth and the banded microstructure is not obvious though since the first phenomenon occurs during melting, while the latter occurs during solidification. Sudden changes in the melt pool size may have caused slight variations in the thermal gradient that could then slow down the solidification rate in that area, and or the difference in thermal conductivity between the coarse and fine microstructure of the bulk could cause local changes in the thermal gradient, as previously discussed. The shift in the solidification velocity caused by fluctuations in the melt pool can be

mapped by measuring the interlamellar spacing at each section within the microstructure according to the **Eq. 1-3** ($v\lambda^2 = K$), where K = 88.8 μm^3/s [137]. An example of this is shown in **Figure 3-31** where the solidification velocity is plotted over the distance of the regions measured in the microstructure.

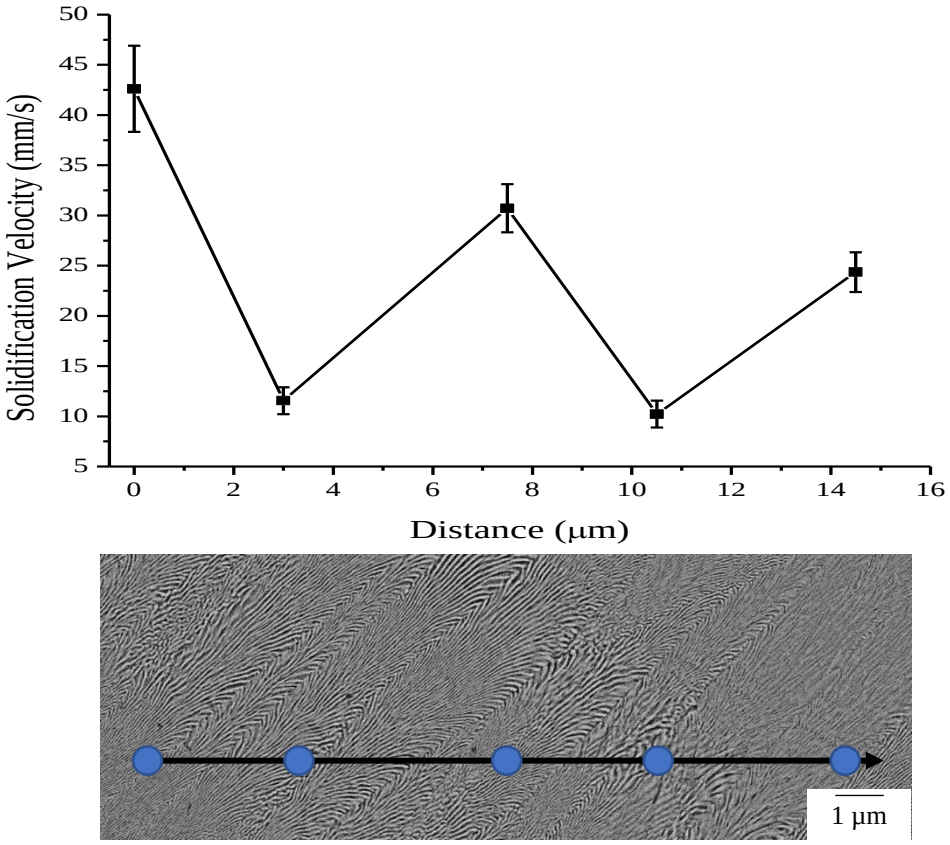

Figure 3-31: Solidification velocity of melt pool derived from the interlamellar spacing of the microstructure. The plot shows how the solidification velocity changes within the banded microstructure, while the SEM micrograph shows a longitudinal cross-section of a remelt line scan processed at 50 mm/s, with each data point in the graph correlating to a blue marker in the image.

Banding microstructures were also observed to correlate with surface ripples of the melt pool, yet not on a one-to-one basis. Ripple formation can occur for a variety of reasons, including displacement of the liquid through piston effect forces of the laser, fluctuations in the laser power, and instabilities caused by both the Marangoni effect and thermal convection [60,138,139,140].

Anthony and Cline developed a theory correlating melt pool ripples to the surface tension gradients and the depth of the melt pool, concluding that the flow of material away from the laser due to the difference in surface energies (dictated by the temperature gradient) may develop instabilities as it shears across the underlying liquid, creating surface waves which solidify into ripples [138]. Volkov and Zhigilei later showed through their model that the laser recoil effect may be the main driving force of the flow of material away from the laser [140]. In either case, if instabilities in the flow of material away from the power source cause wave formation on the surface, these waves may alter the thermal gradient of the melt pool by transferring warmer material towards the solid-liquid interface and thus periodically change the solidification rate of the melt pool and induce banding in the microstructure. That said, if the melt pool is traveling at a fast enough velocity, ripple formation may still develop, but not have much influence on the thermal gradient of the liquid, and thus not change the solidification rate. **Figure 3-32** shows examples of banding microstructure appearing within ripples in a laser remelt sample.

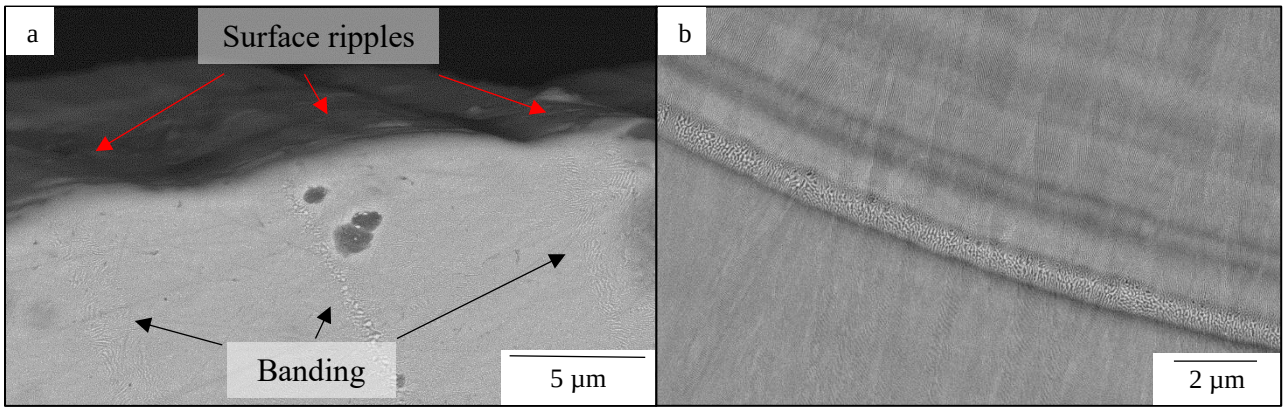

Figure 3-32: Longitudinal cross-section of a laser track in Al-Cu eutectic bulk sample showing banding structures correlating with ripples on surface (a). Top down view of laser track showing banding occurring along surface ripples.

Cross-sections of these samples show the banding microstructure extending from the surface into the bulk of the laser remelt (**Figure 3-32b**). Ripples may also form due to features

within the bulk microstructure, such as pores, that cause a sudden shift within the melt pool. These changes in surface height, while rare in the polished bulk substrate that these line scans were performed in, would be more ubiquitous within the powder layer in the LPBF process, and thus should be taken into consideration. **Figure 3-33** shows an example of ripples that formed as the melt pool fell into the pore, and as the melt pool is reformed on the other side of the pore. It is believed that both the melt pool entering the pore and exiting the pore cause recoil effects on the surface of the liquid that in turn cause ripple formation. In both examples shown in **Figure 3-33**, banding microstructures can be seen within each ripple, suggesting the same shift in the thermal gradient as previously discussed. It should be noted that the banding microstructures observed correlating with ripples extend across the laser remelt track, creating a surface that outlines the geometry of the melt pool at a specific point in time. A distinction is made here between these banding microstructures and others observed within the laser remelt tracks that appear to have no correlation with ripple formation or the underlying bulk microstructure but are more likely due to external sources such as periodic fluctuations within the laser power. These other banding events are discussed in more detail in the following section

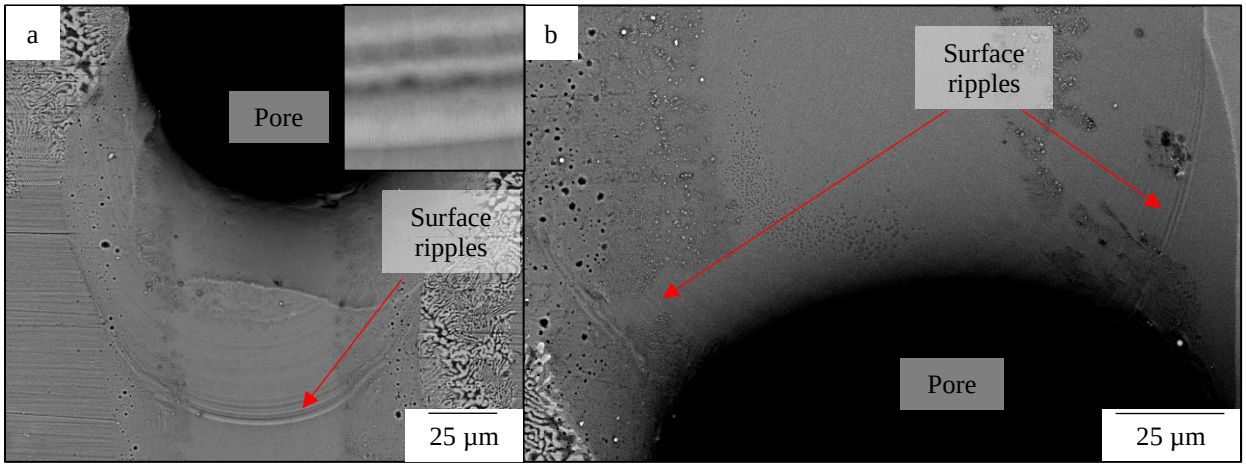

Figure 3-33: Ripple formation both as the melt pool enters a pore (a) and after it reforms on the other side of the pore (b). Inset shows banding microstructure within ripple (a).

3.4.2.2: External causes of banding microstructures

Although most banding microstructures appeared to be caused by fluctuations produced from internal sources, either from instabilities in the melt pool causing ripple formation or changes in the underlying microstructure, a second type of banding was also observed that did not appear to correlate with either of these sources. These banding microstructures extended only partially across the laser remelt track from the edges of the line scan and occurred even when ripples were not present on the surface of the track. The cause of the fluctuation in the solidification rate of the melt pool that produced these partial banding microstructures is thought to be different than that which caused bands found within ripples. The length that these partial bands extended into the laser track appeared to correlate with the laser velocity, and thus solidification velocity, of the remelt track. Correlation of the laser velocity and the extent of the banding structure across the track is shown in **Figure 3-34a**, while an example micrograph of these partial banding features is shown in **Figure 3-34b**. Correlations of these banding features and the melt pool width were also observed (**Figure 3-34b**) suggesting that these bands may arise from fluctuations within the laser power or absorptivity of the material. It is reasonable to suspect that these fluctuations would have less of an effect on the thermal gradients the faster the solidification rate of the melt pool, explaining why the extent of these features decrease in remelt tracks produced at higher laser velocities.

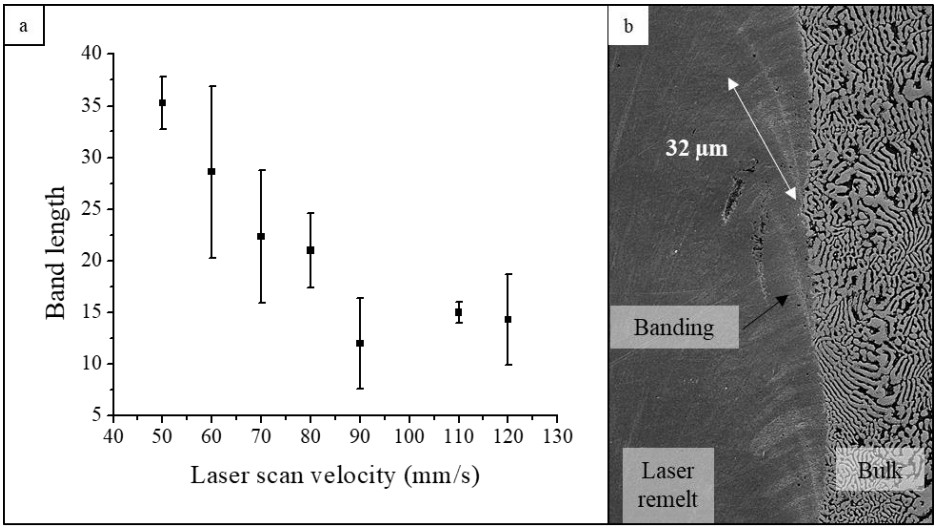

Figure 3-34: Length of bands from edge of laser remelt at varying velocities (a). Top down micrograph of polished laser remelt (50 mm/s) with partial banding occurring at edge (b).

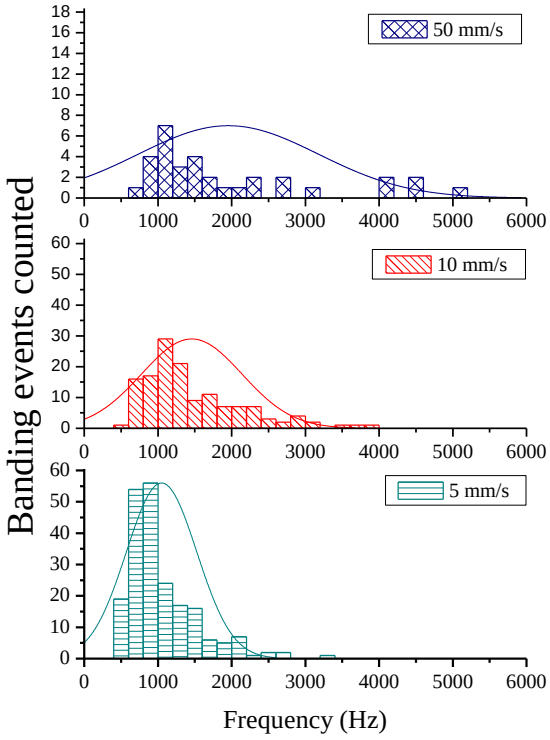

Figure 3-35: The spacing between banding events were measured on edge of laser remelt tracks and plotted as a frequency with respect to the different laser scan velocity. All three laser scan velocities appear to show a peak in the frequency of melt pool fluctuations that occurs around 1 kHz.

The periodicity of these partial bands were measured within laser remelt tracks scanned at 5, 10, and 50 mm/s and the frequencies were plotted. All three line scans appear to have a peak frequency of banding around 1 kHz as shown in **Figure 3-35**, suggesting these partial banding structures may be a result of periodic instabilities within the laser system. Instabilities within high power fiber optic laser systems were investigated by Otto, et al., who utilized a high speed camera and thermal imaging to capture laser spot fluctuation on the order of milliseconds [141]. From their study they found mode instabilities can form at 1.1 kHz at laser powers close to 160 W. The remelt tracks in these experiments were performed with a similar fiber optic laser system at 150 W, thus lending support to the theory that laser instabilities are producing fluctuations within the melt pool, which in turn are leading to periodic banding. Fluctuations in the laser would also explain why the width of the melt pool appears to oscillate, and why these bands correlate with these oscillations. In many ways these bands are similar to those shown in **Figure 3-30**, where fluctuations in the depth of the melt pool correlated with the bands from the bottom rather than the width, yet the difference lies in what causes the melt pool fluctuations, with the first presumably being caused by changes in the thermal properties of the underlying microstructure, and the latter being driven by the external fluctuations within the laser system.

3.4.3: Conclusions

Causations of melt pool fluctuations were studied by using eutectic banding phenomena to indicate where changes in the solidification velocity of the solid-liquid interface occurred. These causations were divided into internal and external sources, where the changes in the microstructure were categorized as internal sources, and instabilities within the laser power or velocity were categorized as external sources. Within the internal sources, correlations were

made between banding phenomena and fluctuations in the melt pool depth caused by variation of the interlamellar spacing of the underlying lamellar microstructure. This was believed to be due to the change in thermal conductivity that has been related to the interlamellar spacing of this microstructure. Correlations of surface ripples on the melt pool and banded microstructure were also shown, suggesting that mass transport of hotter liquid in the melt pool to the solid-liquid interface caused a sudden change in the solidification velocity.

Characterization of the banding length with respect to the scan velocity showed that these fluctuations decreased and ceased to exist as scan velocities above 140 mm/s were reached. The length between banding events within the melt pool were measured in order to determine their frequency. The peak frequency of banding events within line scans processed at three different scan velocities was found to be near 1100 Hz, which is comparable to the frequency of power instabilities found within the laser system used in this study.

Chapter 4 : Controlling Al-Cu eutectic microstructure through LPBF

4.1: Background

Eutectic alloys have recently garnered interests as high-strength alloys in the automotive and aerospace industries when processed by LPBF, with specific attention being given to systems that contain Al or Ti as one of the primary components [132,142,143]. Processing these alloys with LPBF allows rapid solidification rates to be reached within the entirety of a component, which in turn allows the microstructure of eutectic systems to be driven down to the nanoscale. This in turn increases the density of interphase interfaces within the material that impede dislocation motion during plastic deformation [127]. As a result, the strength of these alloys can be directly related to the dimensions of the interlamellar spacing within the eutectic microstructure, analogous to grain size within the Hall-Petch relationship [35]. The solidification rate needed to achieve the minimum interlamellar spacing will depend on the specific eutectic system and the material variables that contribute to the Peclet number such as the diffusion coefficient of the constituent elements in the liquid, yet as long as this rate lies within the processing window available within LPBF, then components could theoretically be built with the microstructure at peak hardness except for deviations that occur at the melt pool boundaries.

Along with this, eutectic alloys processed in LPBF contain the advantage over precipitant hardened alloys of not having to undergo post-processing heat treatments. This, in tandem with the ability of LPBF to build parts that need little post processing anyway makes, makes eutectic alloys more suitable to achieve the goal of a start-to-finish processing technique that can make

fully functional parts on demand. This is specifically the case with aluminum alloys, the majority of which are precipitate hardened, and therefore have been slow to be used within LPBF [119]. The major difference in strengthening mechanisms between eutectic and precipitant hardened alloys may be found in the anisotropic nature of the eutectic microstructure vs the isotropic microstructure of precipitant hardened alloys [20]. While the use of isotropic microstructures are largely favored in industry, the capability to direct the solidification of the eutectic microstructure with the laser scan strategy of LPBF could allow for a layered "plywood" like anisotropy, theoretically giving the bulk material near to isotropic like mechanical properties [144]. Indeed, many different type of scan strategies could be used to disperse the anisotropic mechanical properties of the microstructure, many of which are used for other materials to limit the texturing that occurs during the LPBF process [46].

Finally, not only does the direct phase transformation from a liquid to a two-phase solid in eutectic alloys provide a one-step strengthening mechanism, but these microstructures can also be tailored throughout the entirety of the built part. To do this, specific parameter changes can be designed into the build file for LPBF so that certain regions within the part are processed with different laser parameters, e.g. laser scan velocity and power. As a result, the length scale of the eutectic microstructure can be varied, and thus properties within the material can be designed in relation to the overall geometry of the part. In this way, materials with gradient or region specific microstructures can be designed, potentially leading to composite like advantages within a single alloy. An example of such a part could be imagined, where the interior of the part was processed at a lower scan speed, while the exterior was processed at a higher, thus giving the part a harder exterior while still maintaining a more ductile interior. These types of region specific designs

would be very difficult to achieve with non-eutectic systems that required post process heat treatments to achieve the desired microstructure and properties.

All of the advantages and design techniques discussed require that the relationship between the processing parameters used and the resulting eutectic microstructure to be well understood. Although LPBF is simply laser melting of a material in a layer-by-layer fashion and thus should obey the Jackson and Hunt (JH) model under steady state solidification conditions, a work by Pauli, et al., showed results in the Al-Cu system that appeared to disagree with this model [13]. They questioned whether an increase in laser power could cause the melt pool to no longer be in steady state, and thus the solidification rate be different from the scan velocity of the laser. If this was indeed the case, then control of the interlamellar spacing would be difficult unless the exact parameters were known at which the melt pool deviated from steady state. On the other hand, the thermal conductivity of the part will decrease as more layers are added, and thus the melt pool will solidify more slowly as the build height increases. Another aspect of the microstructure that should be monitored with changes in laser parameters is the width of the eutectic colonies within the build. Colony interfaces have been shown to contribute to dislocation impediment and an increase in yield strength as the average diameter of the colonies decrease [145]. Because colony growth is a form of cellular growth, the widths of the colony are not only dictated of the interface velocity, but also largely by the temperature gradient. Processing parameters are conceivable then that could possibly change the temperature gradient of the interface, such as the power of the laser, while still maintaining a constant growth rate with the laser velocity. That said, other factors such as impurities within the alloy may dictate the extrema of the width of the colonies by causing small perturbations within the solid-liquid interface [146].

The last feature within the microstructure that should be considered in relation to the LPBF process is the melt pool boundary that forms at the edges of each line pass. The microstructure at these interfaces are often coarsened from the thermal input of the laser, and thus present possible weak points within the material [147]. It is important to understand how the solidification occurs at these interfaces, and how this may differ under various parameters and or scan strategies. New layer forms through continuous growth from the previous layer during LPBF due to the atomically rough solid-liquid interface which allows atoms to be incorporated into the previous crystal structure on contact without having to undergo nucleation [148,149]. This continuous growth allows grains to grow epitaxially between layers, often causing extensive texturing within processed materials [150,151]. It has been shown that by rotating the scan direction between layers, epitaxial growth can be suppressed due to the preferred growth direction of the crystal being oriented parallel to the heat flow and laser scan direction [152]. In eutectic systems, the coupled growth of the two-phase microstructure from the previous layer may prove to be more complex than the growth of single phase microstructures due to the self-organization that must occur, i.e. diffusion of elements within the liquid to their respective phases. Further understanding how the two phase microstructure forms during the rapid solidification that occurs within the LPBF process, and how different scan directions may change growth of the new layer, are thus vital to further understanding the relationship between the processing parameters and the overall properties of built parts.

4.2: Correlation of Al-Cu eutectic microstructure with LPBF processing parameters

4.2.1: Motivation

The LPBF process has gained much attention over the last decade due its ability to make complex geometrical shapes with a fine resolution. Along with this, the wide range of processing parameters available within this technique allow for the possibility to create various microstructures within the same material. While most research into the correlation of processing parameters and microstructure focus solely on the parameter range in which fully dense parts can be made, a few groups have begun to take advantage of the different microstructures that are capable of being made within the same part, both in terms of texture and magnetic properties [153,154]. Further research in this area could potentially lead to a 3D engineering of microstructures within the various geometries possible with LPBF [155]. This degree of control could allow engineers to create hierarchical and gradient microstructures that may greatly enhance the mechanical properties of materials [156]. Recent advances in biomimicry have shown that these type of microstructural designs found in bone and shells can be used to create stronger composite materials, especially when realized on the micro and nano length scales [157,158,159,160,161]. Yet before LPBF can be used to fully integrate these bio-derived microstructures into part designs, a better understanding of how the processing parameters dictate the microstructures formed must be gained. In this study, the eutectic microstructure of the Al-Cu system is studied in relation to the laser parameters used within LPBF.

It was first demonstrated through the work of Zimmermann, et al., that directional solidification of bulk Al-Cu eutectic alloy could produce nanoscale lamellae structure through laser irradiation at scan speeds of approximately 200 mm/s [8]. This work supported the JH model of eutectic solidification, showing a direct $v_0\lambda^2 = k_1$ relationship between the lamellar spacing

and the laser scan velocity up to a minimum spacing of 17 nm. After this limit, it was shown that the solid-liquid interface became unstable and banded structures were formed. At still higher velocities (2000 mm/s) it was shown Gill and Kurz that solute trapping occurs, and a metastable solid solution alpha phase is formed [37]. Recently, Pauly, et al., used the Al-Cu eutectic system as a means to experimentally measure the cooling rate within a bulk sample produced by LPBF [13]. As a result of this, the feasibility of creating a bulk nanostructured material through LPBF was also demonstrated. When this study is compared to that of Zimmermann, et al., it is seen that at scan rates of 200 mm/s both studies show lamellar spacing ranging from 20-50 nm, but when Pauly, et al., increased the scan speed to 300 mm/s while keeping the power density constant, coarser lamella microstructures (λ=100 nm) were observed.

Two explanations can be proposed for the disagreement between these studies. First, the sample produced within the LPBF may not have reached a steady state of solidification between the melt pool and the laser scan speed. If this was the case, then the JH model of eutectic solidification would not be applicable to at these processing parameters, and the relation between the laser scanning velocity and the eutectic lamellar spacing would cease to exist. The breakdown of steady state solidification could occur if the power density of the laser was too low to maintain a stable melt pool or if the melt pool was too large so that nucleation of equiaxed grains had time to occur at the surface of the melt pool [162,109]. Either of these conditions could produce a lamellar spacing that reflected solidification rates lower, or higher in cases of nucleation events, than the velocity of the scanned laser. These conditions could be exacerbated within LPBF processing due to an excess in thermal energy within the part, especially along narrow geometries, where heat flow through conduction is limited.

The second explanation is that the analysis of the lamellar spacing performed in the two studies was conducted differently. During solidification of the melt pool, the lamellar microstructure will grow in the direction normal to the highest thermal gradient. Thus, the colonies of lamellae will curve inward towards the center of the melt pool and in the direction of the laser scan. Because of this curvature to the middle of the melt pool, only the lamellae located within the center of the melt track will be in plane with the scan direction. Analysis of the lamellar spacing then must be conducted on samples that are cross-sectioned longitudinally to the scan direction. Along with this the actual solidification velocity must be normalized through the relation given by **Eq. 3-1**. This analysis is usually performed on single-track melts, as demonstrated by Zimmermann, et al., yet in bulk samples processed through many layers of individual overlapping line scans, as used by Pauly, et al., accurately performing this analysis would be extremely difficult.

In this research, the colony width has also been investigated in terms of solidification rate. Unlike lamellar spacing, no long-standing model has been constructed for colony growth within eutectic systems due to the many factors that influence this microstructure [22]. It was shown by Kraft and Albright that colony formation stems from perturbations within the solid-liquid interface which causes cellular growth to occur, where each cell becomes a colony of lamellae [163]. This formation depends on the ratio between the solidification rate (R) and the thermal gradient (G) at the solid-liquid interface [164]. It was found that these two parameters dictate whether a constitutionally supercooled zone forms within the liquid ahead of the solidification front, which in turn causes the perturbations in the solid-liquid interface [26]. This mechanism is enhanced in materials that have higher concentrations of impurities, i.e. other elements besides the binary eutectic composition, which build up in the liquid ahead of the

interface as they are rejected from the solid. Thus, if control could be established of the G/R ratio through laser parameters, then the dimension of eutectic colonies that form in a processed sample could theoretically be controlled at a constant impurity level.

4.2.2: Results and Discussion

4.2.2.1: Correlation of interlamellar spacing with laser parameters

Single-track walls made through the LPBF process using pre-alloyed Al-Cu eutectic powder were cross-sectioned longitudinally so that the microstructure formed at the center of the melt pool could be characterized. SEM was used to obtain SE and BSE micrographs of the lamellar eutectic microstructure, and the interlamellar spacing was measured. In each sample, the solidification velocity was taken with respect to the angle of the solidification as previously discussed. Interlamellar spacing measurements were taken from colonies that appeared to be oriented so that the lamellar microstructure was edge on, i.e. the colonies with the smallest interlamellar spacing. This same procedure was also performed for single-track walls made from elemental powder blends, and on line scans in a bulk cast Al-Cu sample Analysis of the line scans on the bulk sample was performed on the surface of the scans rather than on the longitudinal cross-section. The interlamellar spacing of three of these types of samples were plotted against the solidification velocity and shown to agree with the JH model as well as with other results of Al-Cu eutectic samples made through various processing techniques as found in the literature [8,23,137,165]. These results can be seen in **Figure 4-1** along with example micrographs of the lamellar spacing found in the longitudinal cross-sections of the single-track walls made from the pre-alloyed powder. When analyzing the LPBF single-track wall samples, it was observed that a remelt depth of 25 to 75 μm occurred during each layer. Thus the finest

microstructure near the surface of the melt pool where the growth direction is close to parallel with the translation of the laser, could only be observed within the final layer of the sample. The microstructure near the surface of the single-track wall samples also showed an increased number of colonies with misoriented lamellar microstructure and some that appeared equiaxed in shape rather than columnar. Both of these features suggest that directional solidification may no longer be occurring near the surface of the melt pool, possibly due to nucleation taking place. This type of equiaxed grain microstructure near the surface of the melt pool is commonly seen in the LPBF and DED processes and could occur due to either a large undercooling achieved through thermal convection and radiation of the melt pool surface, or, more likely, due to heterogeneous nucleation of grains off of partially melted powder [133,166]. Controlling the direction and length scale of the lamellar microstructure in these equiaxed grains would not be possible with the laser parameters due to the stochastic nature of nucleation. Yet, because each layer within an LPBF build is partially remelted, this microstructure would only be present on the very surface of a build and would thus not contribute to the bulk properties.

Little variation in the interlamellar spacing is observed between the different types of samples made in this work when plotted in **Figure 4-1**, with all of them appearing to agree with previous results found in the literature. The in situ-alloyed samples do appear to have a slightly larger interlamellar spacing on average than the microstructures of the pre-alloyed and bulk line scan samples, which could be argued is due to larger diffusion lengths caused by poor elemental mixing occurring in the melt pool. A system with large compositional fluctuations in the liquid would thus favor a larger interlamellar spacing at a given solidification velocity [28]. Further experiments would have to be performed to support this theory, as this small difference may lie well within the statistical variance of a larger data set.

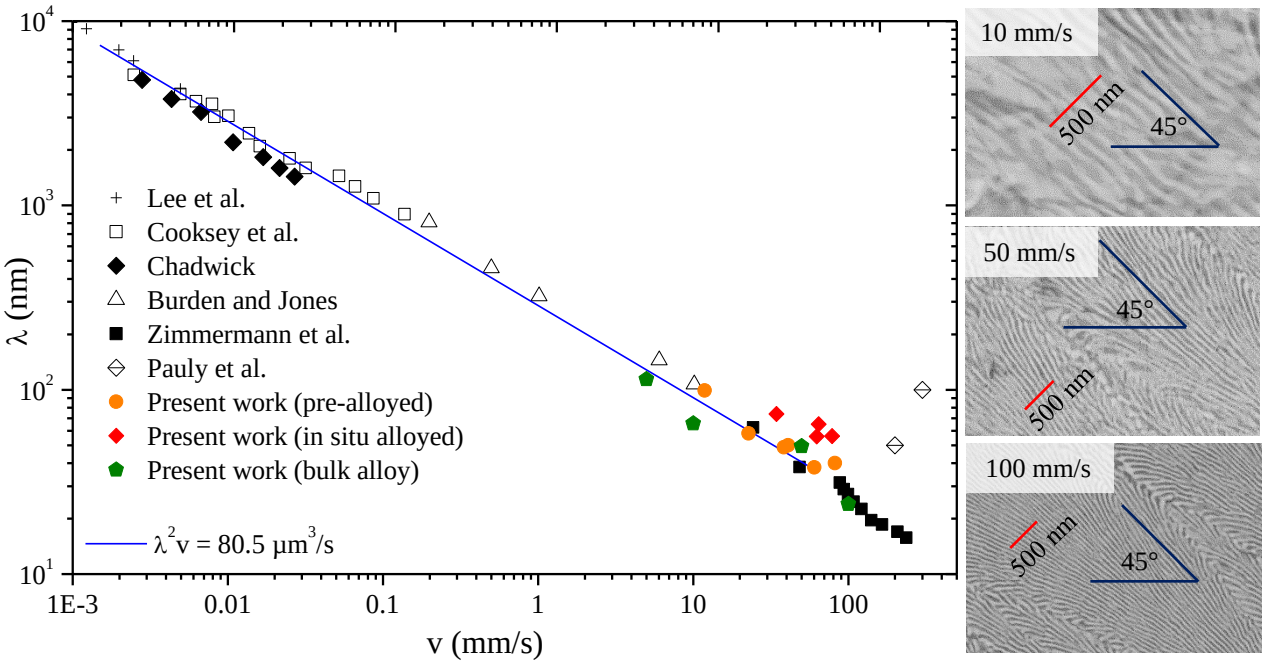

Figure 4-1: Analyzed interlamellar spacing of LPBF processed samples with respect to the laser scan velocity. Present work is plotted alongside data gathered from the literature and shown to agree well with the Jackson Hunt model. Trend line is plotted for data in found in the literature, excluding Pauly, et al., Zimmermann, et al., and present work. This graph has been modified from the work of Sullivan, et al. [137].

To inspect whether laser power had an influence on the lamellar spacing in these samples, three sets of samples were made at three different powers and the resulting interlamellar spacing was plotted against the solidification velocity as shown in **Figure 4-2**. The same trend line is used in this plot as shown in **Figure 4-1** for ease of reference. It can be seen that the overall trend of all data points follows the JH model. Although variation does exist between the data points, there does not appear to be any significant trend with respect to the laser power. A table of the parameters used for these data sets is shown in

Table *4-1*, along with the λ measured in the microstructure and the solidification angle that these measurements were taken at in each sample. It should be noted that for samples made at higher scan velocities and higher laser powers, the melt pool shape usually took on a top hat like geometry, causing the solidification direction of all layers but the very last to be > 45°. The solidification velocity (v) in

Table *4-1* was then calculated using **Eq. 3-1** from the solidification angle and the laser scan velocity.

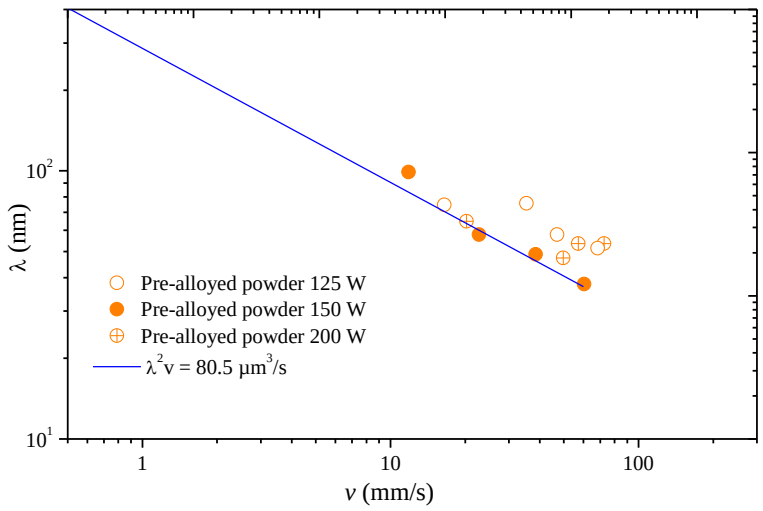

Figure 4-2: Lamellar spacing of pre-alloyed powder samples made at different laser scan velocities and power.

Table 4-1: Parameters used on single-track wall samples made with pre-alloyed powder, along with measurements of λ and the solidification angle at which these measurements were taken within the sample.

	v (mm/s)	λ (nm)	Scan velocity (mm/s)	Laser power (W)	Solidification angle (°)
Set 1	35.4	75.7	50	125	45.0
	27.6	74.7	100	125	74.0
	68.4	51.4	200	125	70.0

	46.9	57.9	300	125	81.0
Set 2	22.8	57.9	50	150	62.9
	11.8	99.0	100	150	83.2
	38.5	48.8	200	150	78.9
	60.3	37.8	300	150	78.4
Set 3	20.3	64.8	50	200	66.1
	49.7	47.3	100	200	60.2
	57.1	53.6	200	200	73.4
	72.6	53.6	300	200	76.0

4.2.2.2: Correlation of interlamellar spacing with laser parameters

Colonies were similarly measured with respect to their solidification angle to see if variations in the scan velocity and or power would influence the length scale of these features. The colonies in all samples were columnar in morphology, with the long axis normal to the solid-liquid interface. The widths of these colonies were measured perpendicular to the solidification direction through a line interception method.

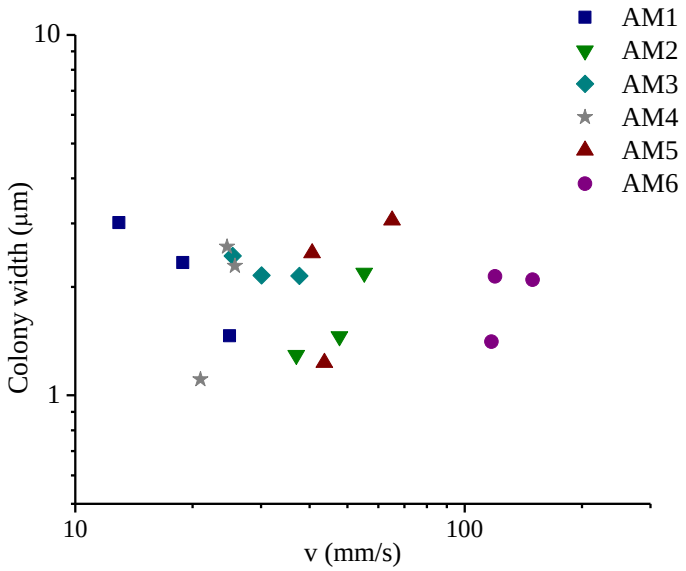

Figure 4-3: Measured width of colonies at six different parameters plotted with respect to solidification velocity. Each parameter is measured in three different regions to show the variation of colony width within the LPBF processed sample. No correlation between solidification velocity and colony width was observed within the parameter range tested.

The colony width of six parameters were measured (laser parameters specified in **Table 3-1**), with three measurements taken from each sample. These results are plotted in **Figure 4-3** against the solidification velocity calculated by the solidification angle. There appears to be no clear trend in this data, with colony widths ranging from 1-3 μm in measurements of all six laser parameters. This suggests that changes in the solidification rate (*R*), and the temperature gradient (*G*) do not alter the length scale within the parameter range used. It is possible that a tertiary impurity element within the powder or build plate is causing constitutional supercooling to occur which dictates the length scale of the colonies within this range of R/G.

If constitutional supercooling was occurring within the melt, then it would be expected that the tertiary impurity would segregate to the colony boundaries as it was rejected from the coupled growth of the two-phase system [146]. To investigate this, a FIB lift out was made of from

a longitudinal cross-section of a single-track wall made with pre-alloyed powder through LPBF. An area was selected near the top of the sample (approximately 2 mm from the build plate) in order to limit any dilution that may have occurred from the build plate. The orientation of the sample was made so that it intercepted several colonies, with the lift out face normal to the solidification direction of the colonies. The selected area that was milled and the resulting FIB lift out sample is shown in **Figure 4-4**.

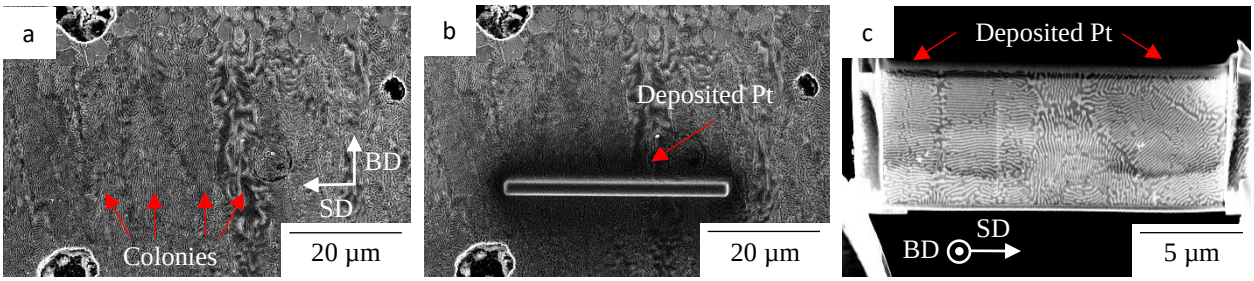

Figure 4-4: Colonies within longitudinal cross-section of Al-Cu single-track wall (a), with Pt deposited (b), and resulting FIB lift out after milling and thinning (c).

Scanning transmission electron microscopy (STEM) was used in high-angle annular dark-field (HAADF) mode with EDS to provide chemical characterization of the colony boundary within a FIB lift out sample. The results of this analysis are shown in **Figure 4-5**. Besides Al and Cu, both Si and Ga peaks were present within the EDS spectra. Because the FIB ion source uses Ga ions, it is assumed this is where the Ga contamination comes from. For Si, the most likely source would be the AA6061 build plate that was used for these samples, which can contain up to 0.8wt% Si in the composition [167].

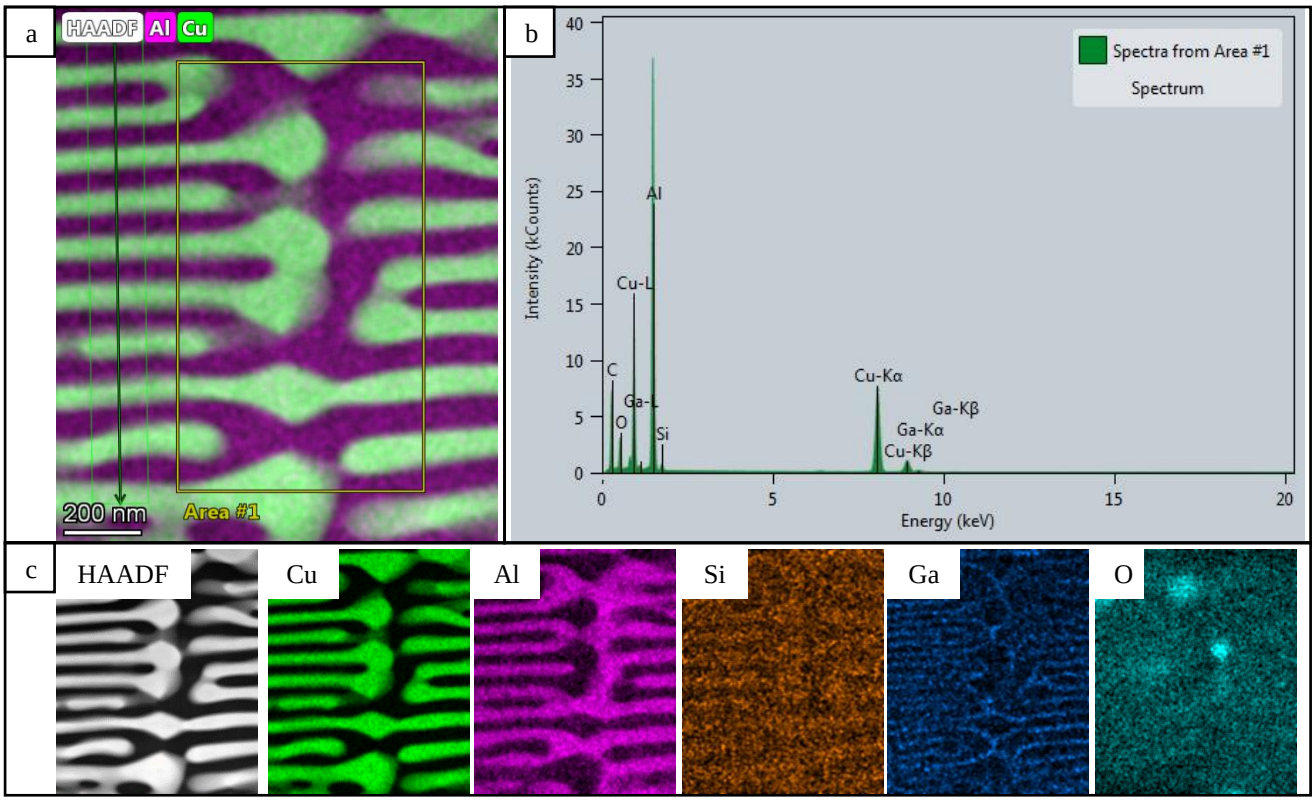

Figure 4-5: STEM EDS results of colony boundary of an Al-Cu eutectic sample processed through LPBF (a). EDS spectrum (b) taken from area 1 (a) shows both Ga and Si present within the sample. Composition maps (c) show net signal of elements being detected within the selected area of the sample, with Si appearing to segregate to the θ-phase lamellae, and Ga segregating to the interfaces between the α and θ-phases.

Remelting of the melt plate upon the first few layers of LPBF could have incorporated this element into the build. Maps of where characteristic X-rays on the sample were detected show that Si is found mostly in the θ-phase (Al_2Cu) being rejected by the Al α-phase most likely due to the binary eutectic that forms between Al and Si. Likewise, Ga is seen segregating to the boundary of lamellae, being rejected by both the α-phase and θ-phase. There is no clear segregation of Si to the colony boundary, but it rather appears to have been incorporated into the θ-phase during solidification. It appears that while Si may be inducing constitutional supercooling in the liquid and contributing to the cellular width, the concentration of this ternary element is still low enough to be soluble with within the θ-phase.

4.2.3: Conclusions

In this study, the relationship between the laser parameters in LPBF and the eutectic microstructure formed were investigated. The steady-state solidification of the melt pool was validated within the parameter set studied by showing that the eutectic microstructure followed the JH model of eutectic solidification. This was performed on both bulk and LPBF processed samples. It was then shown that neither the laser power or scan velocity caused any significant change in the width of the eutectic colonies, with all samples showing colony widths of 1-3 μm. The composition of the colony boundary was then investigated using TEM EDS of a FIB lift out, and Si was found to be present within the θ-phase. The tertiary element is believed to cause constitutional supercooling during solidification which dictates the colony width.

4.3 Variations in mechanical properties of LPBF processed Al-Cu eutectic

4.3.1: Motivation

Recent studies have shown that the mechanical properties of alloys produced by the LPBF process are superior to many traditional processing techniques [168,169,170,171]. Yet little research has been devoted to understanding the possible range of mechanical properties that may be achieved by LPBF. Specifically, eutectic alloys which form a two phase microstructure directly from the liquid have been shown to produce a wide variety of microstructures at different processing parameters and thus pose as good candidate systems to explore the variety of mechanical properties could be produced through LPBF processing [37,172]. Due to the layer-by-layer method of this technique, parameters of the build can be controlled throughout the volume of the part. Thus, a study investigating the range of mechanical properties that might be available through

different processing parameters would lay the foundation to create internal architectures or functional gradients within parts made from these alloys. Such designs could allow for a transition of properties, such as a hard microstructure on the exterior of a part and a microstructure with a softer microstructure towards the interior, a design found in many components such as gears to reduce surface wear and fatigue of the part. Thus providing the possibility to improve the overall performance and service life of the component.

4.3.2: Results and Discussion

4.3.2.1: Correlation of microstructure and hardness

Mechanical properties of the laser induced microstructures in both the LPBF processed and bulk line scan samples were interrogated using Vickers hardness testing. Pre-alloyed Al-Cu powder was used for the samples made through the LPBF process to reduce any variations in the microstructure that might occur due to local variations in elemental concentrations (as shown in Section 3.3.2). Variation in the lamellar spacing, and thus hardness, within these samples existed due to the change in the solidification velocity from the bottom of the melt pool to the top. Because samples processed through LPBF were made in a 5 x 5 x 2 mm coupon, and consisted of an array of melt pools rather than single-track walls, a precise location of the hardness tests within the melt pool could not be determined. Thus, to simplify the correlation between hardness and the microstructure, line scans in a bulk cast sample were first tested to provide a base line for the LPBF samples. Two sets of line scans were made within a bulk cast sample; one at a constant power and one at constant velocity as shown in **Table 4-2**. The average Vicker's hardness values for these two sets of line scans were then compared in **Figure 4-6**.

Table 4-2: Parameters for line scans made in bulk cast Al-Cu sample

Set 1												
Velocity (mm/s)	5	10	50	100	200	300	400	500	700	1100	2000	3000
Power (W)	150	150	150	150	150	150	150	150	150	150	150	150
Set 2												
Velocity (mm/s)	100	100	100	100	100	100	100					
Power (W)	50	100	125	150	200	250	300					

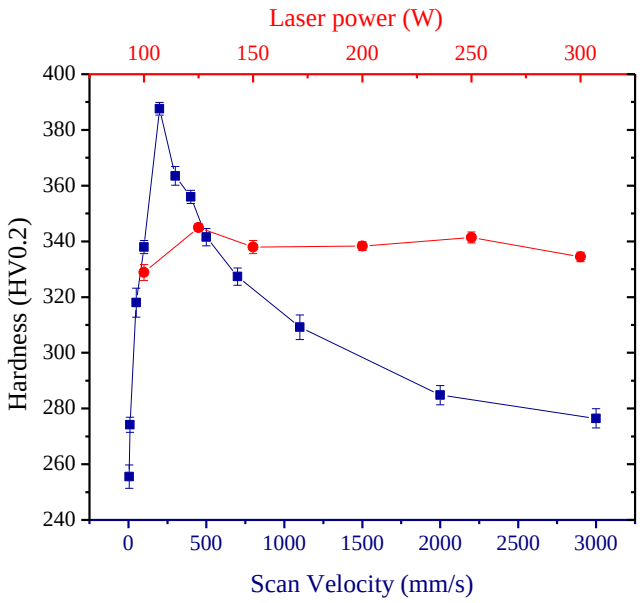

Figure 4-6: Hardness values for two sets of line scans; set 1 varies laser scan velocity (blue) at a constant power (150 W), and set 2 varying laser power (red) at a constant velocity (100 mm/s). The hardness values of the set 1 increase to a peak hardness at 200 mm/s and then decrease at higher scan velocities, while the hardness values of set 2 samples stay consistent as the laser power is increased.

The fact that the hardness values changed very little for the line scans made at varying laser powers further supports the previous conclusion that the length scale of both the lamellar spacing and the colony widths change very little with the power parameter. For line scans produced at varying laser scan velocities, the hardness ranges from 255 to 390 HV/0.2 (2.5 to 3.8 GPa). The hardness of the line scans increases steadily to a peak hardness obtained at a laser scan

velocity of 200 mm/s, where it then begins to decline with increasing scan velocity. The increasing and decreasing trends in the hardness can be directly attributed to several distinct transitions the microstructure undergoes within this range of solidification velocities. **Figure 4-7** shows examples of the microstructure of the line scans at various scan velocities. Because the hardness tests and micrographs were both taken in the center of the surface of the line scans, the solidification velocity of these regions are equivalent with the laser scan velocity. That said, it should be noted that the microstructure changes on the edges and deeper within the line scan due to the solidification angle as previously discussed. This is specifically relevant for the microstructure shown at 200 mm/s in **Figure 4-7**, where the peak hardness appears to be when the microstructure is not lamellar but dendritic. Yet cross-sections of this line scan showed that the dendritic microstructure formed only within a micron of the surface, and beneath this a very fine lamellar microstructure was observed. Considering that the depth of the Vicker's hardness measurement for the force used in this study was approximately 3 μm, it is assumed that the fine lamellar microstructure directly under the surface is responsible for the peak hardness, and that even higher hardness values may be possible at the surface of line scans made at a slightly lower scan velocity.

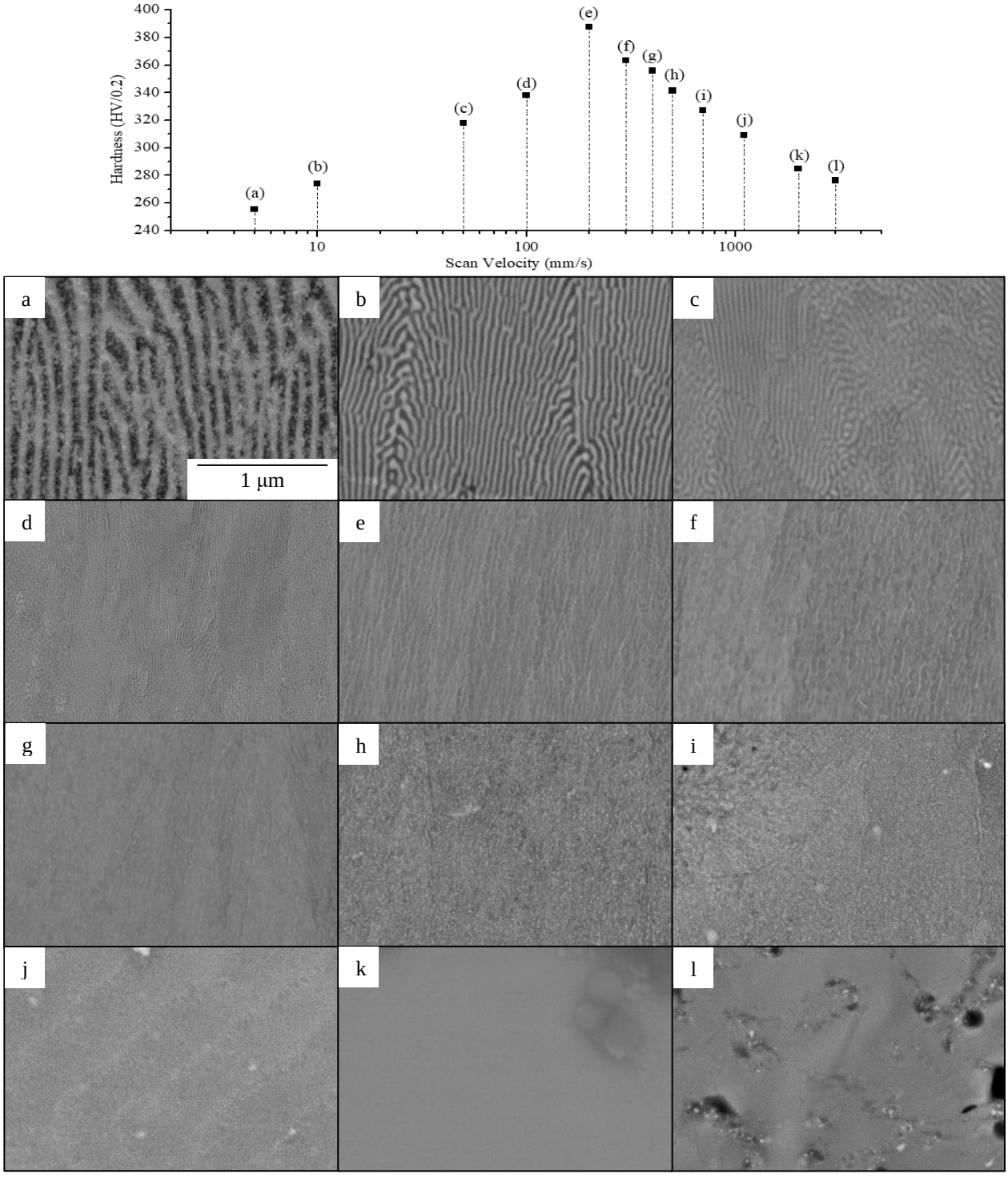

Figure 4-7: Hardness values of line scans plotted on a log scale with images of corresponding microstructures (a-l) produced at the various scan velocities. Trends between the microstructure and the hardness can be seen, with an increase in hardness occurring due to a refinement of the interlamellar spacing (a-d), and a decrease in hardness occurring with the breakdown of the lamellar microstructure to dendritic (e-i) and metastable solid-solution microstructures (j-l). All images are scaled to the same scale bar.

The initial increase in hardness in **Figure 4-7** can be attributed to a refinement of the lamellar spacing within the microstructure, where the higher density of interfaces impede dislocation motion. This strengthening mechanism is much like the Hall-Petch relationship given below

$$\sigma_y = \sigma_0 + \frac{k_y}{\sqrt{d}},$$

Eq. 4-1

where the yield strength of the material (σ_y) is inversely proportional to the diameter of the square root of the average grain diameter (d), and σ_0 and k_y are material constants [173]. Substituting the interlamellar spacing for the grain diameter gives:

$$\sigma_y = \sigma_0 + k_y \lambda^{-\frac{1}{2}}.$$

Eq. 4-2

By taking the inverse of the square root of the interlamellar spacing and relating hardness to overall flow strength, a Hall-Petch plot can be made from which the material constants of the above equation can be determined through the best fit line of the data [127]. The first four line scans of Set 1 (**Figure 4-7a-d**) are plotted in this type of plot and shown in **Figure 4-8** along with a linear trend line. This type of analysis could not be performed on all the line scans due to the microstructure changing on the surface from a lamellar to a dendritic microstructures. To better understand the trend for the decreasing hardness, the solidification velocity must be used instead of the interlamellar spacing.

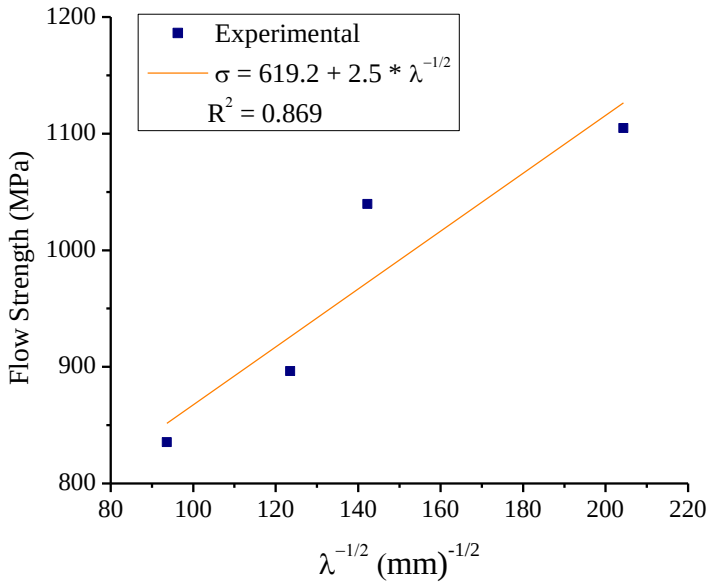

Figure 4-8: Hall-Petch fit of flow strength (estimated from hardness) plotted against the inverse root of the interlamellar spacing.

The flow strength of the material can be related to the solidification velocity through the JH model as given by **Eq. 1-3**. Substituting solidification velocity for λ gives the following:

$$\sigma_y \propto v^{\frac{1}{4}}.$$

Eq. 4-3

Thus a $v^{1/4}$ relationship to the flow strength is expected if refinement of the interlamellar spacing increases the strength of the material as described by the Hall-Petch equation. This relationship may be further extrapolated to see if the decrease in hardness likewise follows a Hall-Petch like trend, where the gradual break down of the interphase interfaces reduces the total flow strength of the material. **Figure 4-9** shows a plot where both the increasing and decreasing trends in hardness are plotted over a $v^{1/4}$ relationship and linear trend lines are fitted to both slopes. It

should be noted that the linear trend line fitted to the decreasing hardness values has a slightly lower R^2 value than the increasing hardness values, yet when plotted against a $v^{1/8}$ relationship, the decreasing values can be fitted to a linear trend line with an R^2 value of 0.980 (not shown in **Figure 4-9**). This may be due to solid-solution strengthening that is occurring at these higher solidification velocities, even though the sum of the flow strength is still decreasing.

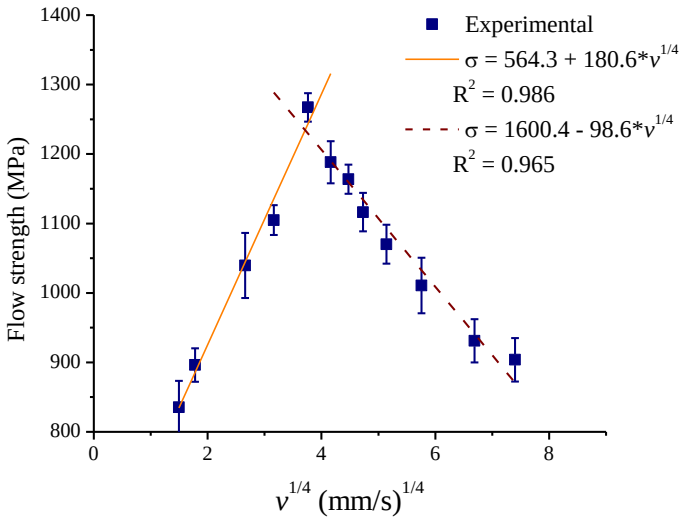

Figure 4-9: Hardness value of line scans made at various solidification velocities plotted to provide a Hall-Petch like fit to the data. Increasing trend in hardness (solid line) is ascribed to a decrease of interlamellar spacing with increasing solidification velocities. The decreasing trend in hardness (dashed line) occurs due to the decrease in interphase interfaces as the lamellar microstructure decays to a dendritic and then metastable solid-solution microstructure.

4.3.2.2: Anisotropy of lamellar microstructure

The anisotropy of LPBF samples were measured by testing the hardness values of the samples on surfaces normal to the scan direction (SD) (transverse cross-section), translation direction (TD) (longitudinal cross-section), and the build direction (BD) (surface of the sample). A schematic of these surfaces are shown in **Figure 4-10** along with the hardness values obtained from samples made at four different scan velocities and constant power (150 W).

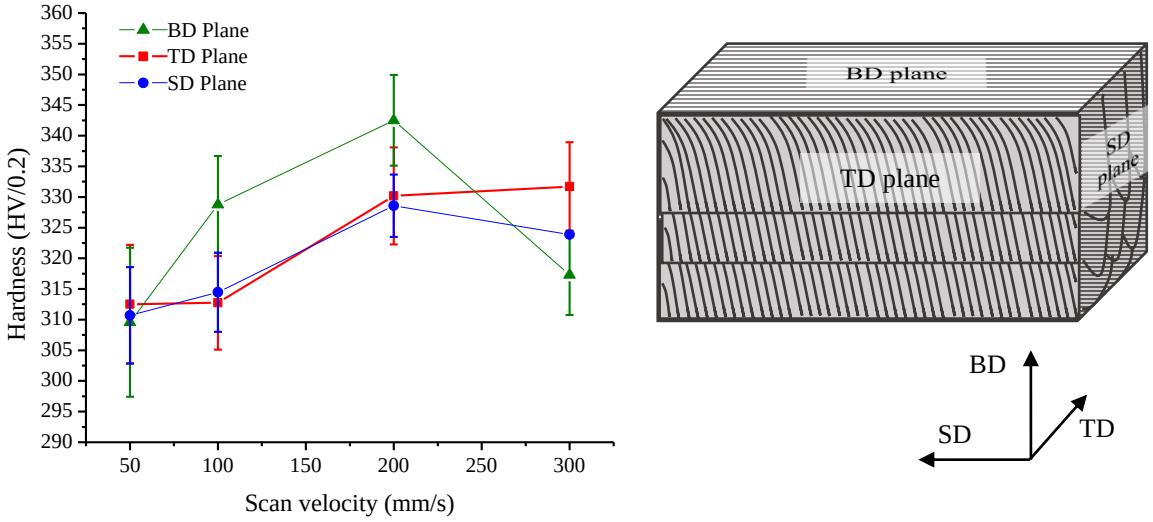

Figure 4-10: Plot of hardness averages for the three different surfaces of four samples at increasing laser velocities along with orientation of LPBF processed samples and planes that were tested.

Although the average hardness values of the LPBF samples appear to vary greatly, some trends may still be distinguished from the plot in **Figure 4-10**. First, the overall trend of the build direction plane follows that of the line scan samples, where a peak hardness is found at samples processed with a scan velocity of 200 mm/s, after which the hardness values begin to decline. That said, the hardness values for the build direction plane in the LPBF samples are all around lower than those tested in the line scans. This is most likely due to polishing that took place to flatten the surface of these samples which removed the true surface of the sample. Thus the microstructure that solidified at the highest velocities was likely not present. Likewise, the scan direction and translation direction planes contained only the lower portion of the melt pools which solidify at slower rates due to remelting that occurs with each layer made in the LPBF process. Thus both of these planes show lower hardness values, that is until 300 mm/s, at which the build direction plane (surface of melt pool) contains dendritic like microstructures, while the lower parts of the melt pool still contain fine lamellar microstructures due to the slower

solidification velocities. This explains why both the scan direction and translation direction planes have a higher average hardness than the build direction plane at 300 mm/s. Overall, the anisotropy of the LPBF builds in terms of hardness may be mostly attributed to the difference in the solidification velocity throughout the melt pool rather than the orientation of the lamellar microstructure in these samples. This is not to say that anisotropy within these samples doesn't exist, simply that on the scale of the Vicker's microhardness measurements the mechanical anisotropy of the lamellae orientation are too fine to be detected, and the bulk anisotropies introduced by melt pool orientations are too large. Previous work by Okayasu, et al., showed that a difference in the solidification orientation of continuous cast Al-Cu eutectic samples can have up to a 30% difference in the tensile and fatigue properties [20]. Yet, this was largely attributed to the orientation of the colony and grain boundaries within the samples rather than the lamellar orientation. Similarly in LPBF, the orientation of melt pool boundaries are most likely to be the source of detectable anisotropy within bulk samples rather than the orientation of the microstructure.

4.3.2.3: Mechanical properties of melt pool boundaries

Hardness measurements were made on the melt pool boundaries within the LPBF processed samples and compared with values obtained between these boundaries. These comparisons showed a significant difference in hardness, especially in samples that contained very fine lamellar microstructures within the bulk. An example of this comparison is showed in **Figure 4-11** where the difference in flow strength between the two indents is approximated from the hardness values to be 160 MPa.

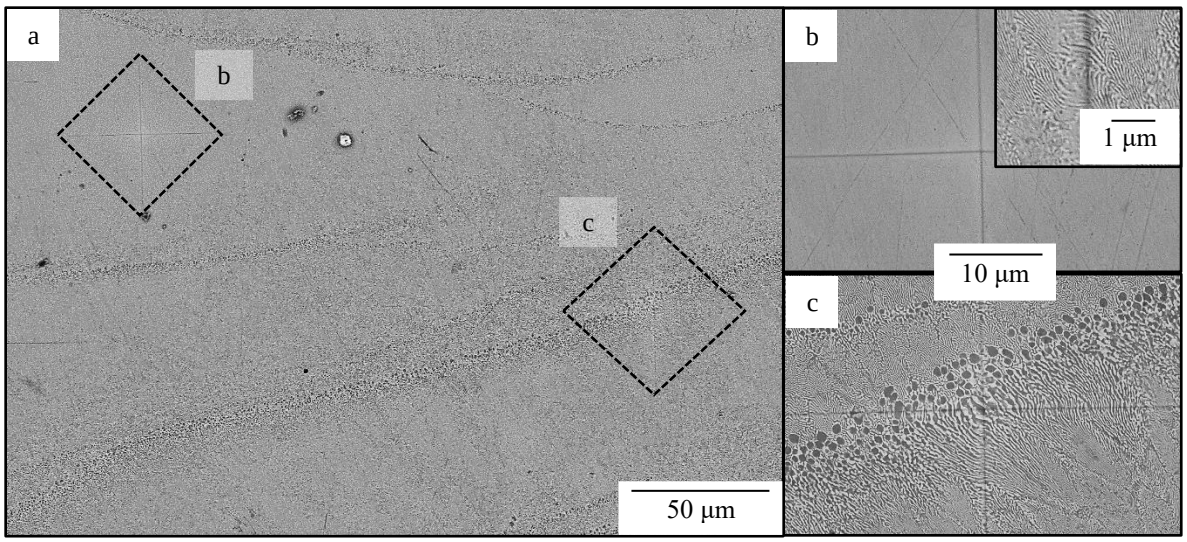

Figure 4-11: Longitudinal cross-section of a LPBF processed sample (a) showing two indents (dotted lines); one in the bulk of the sample (b), and one centered on a melt pool boundary (c). Difference in the length scales of the eutectic microstructure can be seen between the inset in (b) and (c). The hardness difference between the two indents was approximately 500 MPa, giving an approximate difference in flow strength of 160 MPa, with the microstructure in the bulk (b) being the harder of the two.

The change in length scale of the microstructure between the bulk (**Figure 4-11b**) and the melt pool boundary (**Figure 4-11c**) in can be attributed to two factors: first, the heat affected zone (HAZ) directly under the solid liquid interface contains coarsened lamellar due to the increase in diffusion rates at high temperatures; second, the solidification velocity is at its lowest at the edge of the melt pool due to the angle of solidification. Along with this, the specific method by which the new LPBF layer forms on top of the old, e.g. whether epitaxial growth is disrupted due to the solidification direction of each layer, may contribute significantly to the mechanical properties of these regions.

Because the location within the melt pool could not be distinguished in the cross-sections of the LPBF samples, and due to the overlapping of melt pool boundaries that often occur in these samples, line scans made in a bulk sample were again used as a way to simplify the system. These samples were made so that an overlap of approximately 25-50% was obtained between

parallel line scans. Line scans running perpendicular to each other were then made, allowing two different orientations of melt pool boundaries to be tested. These line scans were made at constant power (150 W) and increasing velocity, as shown in Set 1 of **Table 4-2**. The orientation of these line scans, location of hardness measurements, and recorded average hardness values of the melt pool boundaries compared with those found in the center of the line scans are shown in **Figure 4-12**.

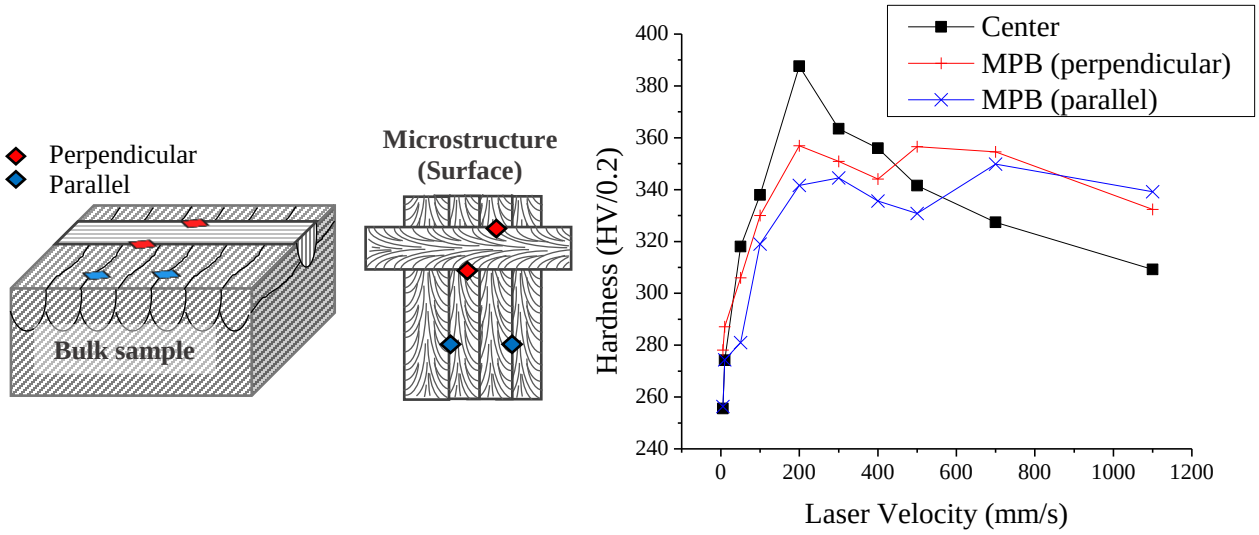

Figure 4-12: Schematic of line scans made in bulk sample and location of hardness measurements taken of MPBs. Average hardness plot of both perpendicular and parallel MPBs are shown on the plot to the left, and compared with values obtained in the center of the line scans.

It can be seen by the plotted hardness values that the microstructure on average at the melt pool boundaries is softer, that is until scan velocities of approximately 500 mm/s are reached. At these scan velocities, the microstructure within the center of the melt pool is dendritic, yet at the edge of the melt pool where the solidification velocity is slower, the microstructure is still a fine lamellar eutectic. An example of this is shown in **Figure 4-13** where

the microstructures of boundaries between parallel line scans are shown at two different velocities; one where the finest lamellae is located in the center of the line scan (**Figure 4-13a**), and one where a dendritic microstructure is located in the center of the line scan and a fine lamellar microstructure is located at the boundary (**Figure 4-13b**).

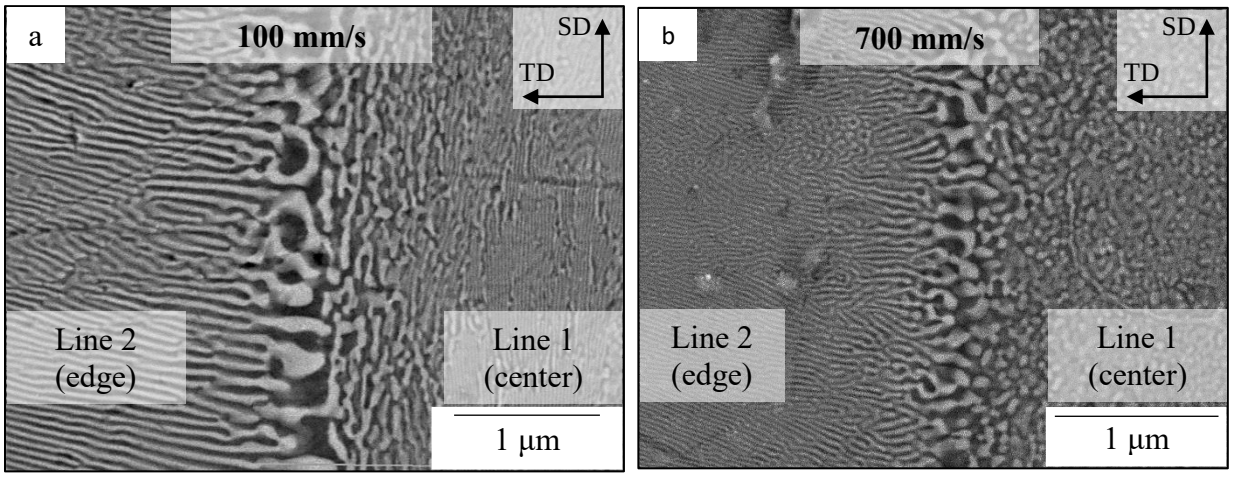

Figure 4-13: Two examples of melt pool boundaries between parallel line scans made at different scan velocities. The boundary between the line scans made at 100 mm/s (a) contain fine lamellae in the center of line 1, but coarse lamellae at the edge of line 2. In comparison, the boundary between line scans made at 700 mm/s (b) contain fine dendritic microstructure in the center of line 1, and fine lamellae at the edge of line 2.

These results indicate that samples made in this system at laser scan velocities higher than 500 mm/s will have melt pool boundaries that are harder than the bulk of the line scans. This suggests that, instead of being weak points within a bulk LPBF processed part, melt pool boundaries could possibly be engineered so that they acted as stiffeners within a softer matrix. Along with this, the plot in **Figure 4-12** shows a clear distinction in hardness between melt pool boundaries of parallel line scans, and those between perpendicular line scans. The reason for this difference is not obvious, yet it may in part have to do with the orientation of the microstructures of the two line scans. Because the solidification angle of the microstructure with respect to the scan

direction changes from close to 90° at the edge of the melt pool, to parallel with the scan direction in the center, the microstructure orientation of two parallel line scans will only be similar at minimum overlaps. When parallel line scans overlap so that the edge of second melt pool is close to the center of the first, the orientation of the microstructures will be orthogonal to each other. In contrast, perpendicular line scans will have the microstructures oriented in the same direction within the vicinity of the melt pool boundary. The surface schematic in **Figure 4-12** shows how the solidification angle within the line scans causes this effect. Having the microstructure oriented in the same direction at the melt pool boundary may facilitate epitaxial growth across line scans, which could in turn improve the strength of the boundary.

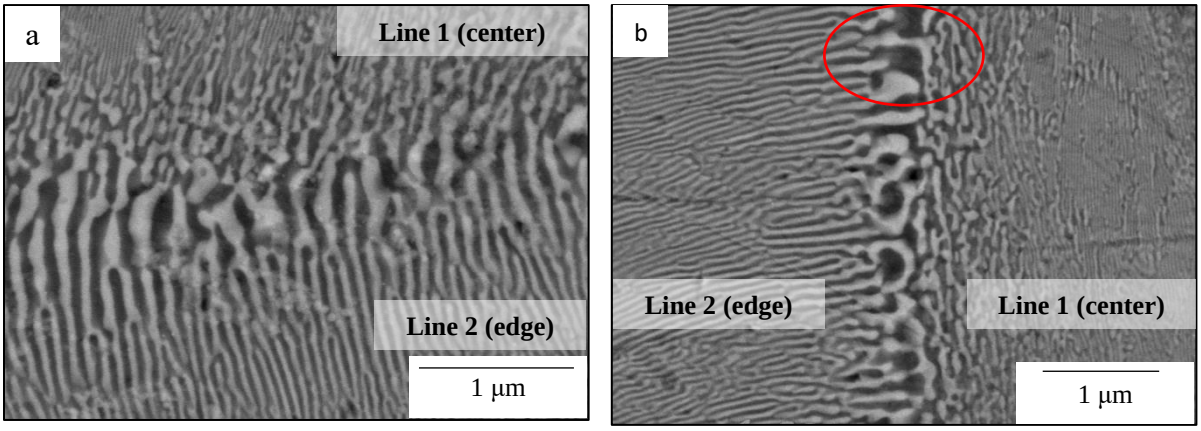

Figure 4-14: Melt pool boundary between perpendicular line scans (a) and parallel line scans (b). Lamellae between perpendicular line scans (a) appear to cross over the melt pool boundary, suggesting continual growth, while lamellae between parallel line scans (b) appear to grow at right angles form the previous lamellae (red circle). Both sets of line scans were made at a scan velocity of 100 mm/s.

A comparison of both the boundary between perpendicular and parallel line scans is made in **Figure 4-14**. The lamellar microstructure appears to somewhat more continuous in the perpendicular boundary where the orientation of the lamellae are the same than in the parallel boundary where they are orthogonal to each other. It is believed that the continuous growth of

the lamellae across the melt pool boundary is a strong indicator of epitaxial growth occurring which may lead to a stronger boundary. At higher solidification velocities (above 700 mm/s), the difference in hardness between the two boundary orientations appears to diminish, possibly due to the difficulty of epitaxial growth to occur at these velocities no matter the orientation of the microstructure. It may also be that epitaxial growth of the lamellar microstructure may not occur as easily on the edge of a new line when the center of the previous line contains a dendritic microstructure.

4.3.3: Conclusions

The mechanical properties of various microstructures formed in both LPBF and line scan samples were measured, specifically in terms of their average hardness. Variation of the laser power was shown to have little effect of the hardness values of samples, especially when compared to the change in hardness that was achieved with variations in the scan velocity parameter. Refinement of the lamellar microstructure produced by increasing scan velocities yielded a Hall-Petch like trend when measured by Vicker's microhardness on the surface of the line scans. A similar decreasing trend in hardness was also observed as the microstructure of the laser processed Al-Cu eutectic samples changed from lamellar to dendritic, and then finally to a metastable solid-solution phase. Due to the difficulty of measuring dendritic length scales, this decreasing trend was plotted against $v^{1/4}$ to yield a linear relation similar to the Hall-Petch like trend found with the refinement of the lamellar microstructure. The hardness values of different planes within LPBF processed samples were compared and differences were found to be largely due to the solidification angle and change in solidification velocity from the bottom of the melt

pool to the top. Finally the hardness values of MPBs were analyzed between both parallel and perpendicular line scans and compared with the hardness measured at the center of the line scans, all at a range of scan velocities. This analysis showed that melt pool boundaries are on average softer than the center of the line scans in scan velocity ranges where lamellar microstructure forms due to the coarser microstructure present at these interfaces. At higher scan velocities (> 500 mm/s) melt pool boundaries have on average a harder microstructure than the center of the line scans due to the fine lamellar microstructure that forms at the edges compared to the dendritic or metastable solid-solution microstructure that forms in the center. Along with this, the orientation of the line scans appears to affect the hardness of the melt pool boundary between them, possibly caused by the difference in orientation between the microstructure on either side of the interface. These results help lay the foundation for controlling mechanical properties of LPBF processed parts through processing parameters and scan strategies, enhancing the degree of material design that can be achieved.

4.4: Solidification of Al-Cu eutectic across melt pool boundaries in LPBF

4.4.1: Motivation

The layer-by-layer processing method used by LPBF allows this technique to create a wide range of geometries and part designs, from intricate lattices to custom made implants[174,175,176]. Yet this design freedom comes at the cost of having many melt pool boundaries throughout the entirety of the built part, introducing possible weak points within the microstructure. These interfaces have been shown to cause significant anisotropy in the mechanical properties of built parts depending on their orientation relative to the force applied to them [147]. Some of the obvious reasons these boundaries are detrimental to the mechanical properties of an LPBF built part are due to defects such as lack of fusion pores or oxides [77,147]. Along with this, the microstructure at the melt pool boundaries often differs from the bulk due to coarsening that occurs at the interfaces as a result of transient high temperatures this region experiences in the solid state [177]. In most systems, epitaxial growth will occur across melt pool boundaries when the heat flow is parallel between the two layers, yet when scan directions and thus heat flows are different between layers, new grains are often nucleated that are better oriented to the heat flow [177]. An accumulation of grain boundaries will locate at the melt pool boundary that could lead to crack propagation at these sites [154,178].

In terms of eutectic solidification, growth at the melt pool boundaries may be more complex due to the coupled growth of the two-phase system that occurs. In faceted/non-faceted eutectic systems, the anisotropy of the faceted phase may lead to a more preferred growth orientation [179]. Along with this, specific orientation relationships between the two phases have been shown to occur, specifically when one phase is faceted [23]. Both of these crystallographic restrictions greatly influence the microstructure until the a low energy orientation is reached

[179,180]. It was shown by Kraft that orientation relationships between the alpha (Al) and theta (Al_2Cu) phases existed within the Al-Cu system, and that these took time to reach the preferred orientation during the growth [23,164]. During remelting experiments, Kraft observed that the θ-phase quickly oriented so that the lamellae were bounded by (211) planes in the [120] direction, while the α-phase oriented after a few centimeters of growth so that it was bounded by (111) planes in the [101] direction. Further remelting experiments were carried out by Chadwick, who used a single crystal of Al-Cu with a lamellar microstructure and partially remelted it in different directions. It was observed from these experiments that the lamellar microstructure appeared to maintain registry through the remelt boundary, even at angles of 15°. It was proposed by Chadwick these "bends" in the lamellae either changed the crystallographic orientation of the two phases, or that the lamellae formed a stepwise boundary and maintained their preferred orientation [23]. Recently, Wang, et al., performed an investigation using TEM and EBSD to characterize the orientation relationships in nano scale Al-Cu eutectic lamellae [181]. Through this study it was shown Chadwick's assumption was correct and that steps or terraces do indeed form on the interfaces between the lamellae, allowing the crystallographic orientation to stay the same even through bends in the lamellae.

In this study the solidification of the Al-Cu model eutectic system at the melt pool boundary of a LPBF processed sample is characterized. This research extends past studies by examining the growth of the two-phase system at solidification velocities nearing the rapid solidification regime. Although Wang, et al., were the first to study orientation relationships of fine lamellae in this system at similar solidification velocities, they did not examine how the two-phase system grows from an interface where the seed layer also contains a very fine lamellar microstructure [181]. Likewise, although Chadwick was the first to examine growth of the lamellar

microstructure from a seed layer, further studies have not been carried out to examine if similar results are obtained at very high solidification velocities [23,165]. Along with building off of previous research, results from this study may also be applicable to other facted/non-faceted eutectic systems that are currently being studied as potential alloys to be processed through LPBF [9,142,182].

4.4.2: Results and Discussion

4.4.2.1: Eutectic microstructure at melt pool boundaries

The microstructure present at the melt pool boundaries within LPBF samples can often be divided into two regions. First, there is the heat affected zone (HAZ) that forms below the solid-liquid interface which consists of coarsened microstructure. Second, there is the area directly above the HAZ, which is also often coarse due to the solidification direction with respect to the laser scan direction. Thijs, et al., refer to this second region as the "melt pool coarse" (MP coarse), while Xiong, et al., refer to this region as the "remelted zone", with both referring to the first region as just the HAZ [147,177]. Both of these studies were performed in the Al10SiMg system, yet a similar distinction can be made between two regions found at the melt pool boundaries in the Al-Cu eutectic system studied here. **Figure 4-15** shows an example of a melt pool boundary within a longitudinally cross-sectioned single-track wall where both a HAZ and a MP coarse region are outlined. The microstructure of the HAZ can be attributed to the high temperatures that are reached directly under the liquid melt pool which allow higher rates of diffusion and thus a reduction of the interfacial energy through coarsening of the lamellae. It should be noted that the coarsening in the HAZ occurs further into the microstructure of the previous layer along the colony boundaries, which is most likely due to the increased mass

diffusion rates at these interfaces. The formation of the MP coarse region on the other hand is a bit more difficult to explain. It may at first appear that this region is part of the HAZ as well, and that the coarsened microstructure with the spheroidized α-phase occurs due to a further reduction of the interfacial energy, yet some of the spheroidized α-phase appear above finer lamellar microstructure (white arrows) which cannot be explained by this theory. Beyond this, results in the next section provide evidence that the solid-liquid interface occurs below this region as indicated by the red dashed line in **Figure 4-15**.

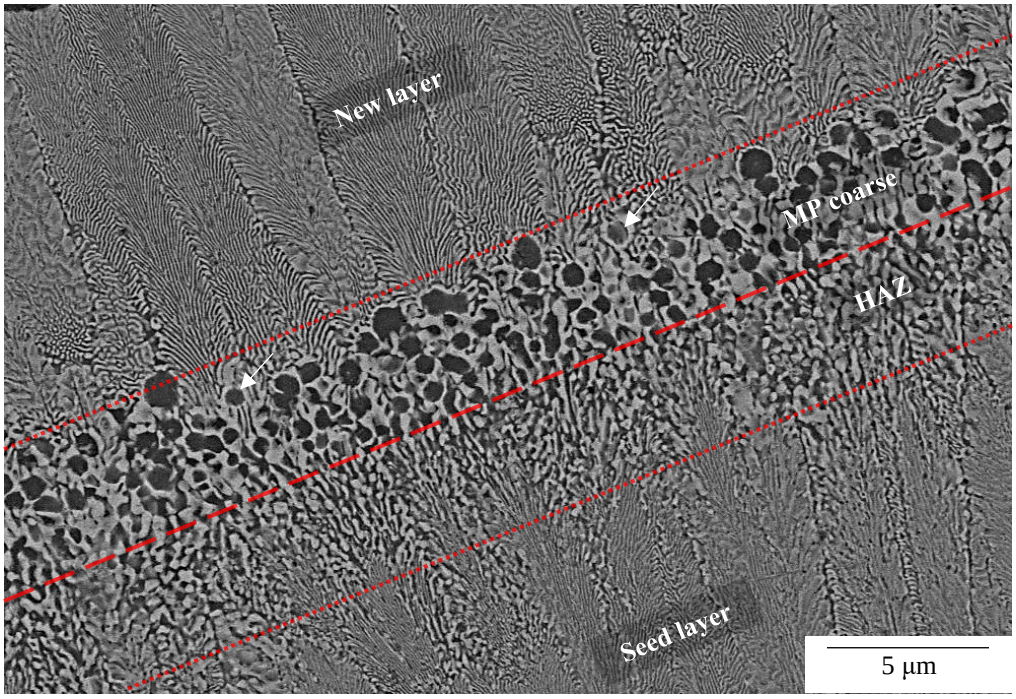

Figure 4-15: Melt pool boundary shown within a longitudinal cross-section of a LPBF processed sample. The melt pool boundary can be separated into two distinct regions; the HAZ and the MP coarse regions. The α-phase within the MP coarse region appears to have formed into spheroids, with some occurring above a finer lamellar microstructure (white arrows).

Another possibility could be that the microstructure in MP coarse region is the result of dendritic growth of the α-phase, and that the micrograph is showing a cross-section of the secondary dendritic arms. An example of α-phase dendrites growing ahead of the eutectic

coupled growth have been shown to occur within laser melted particles (**Figure 3-12**). If this was the case though, the MP coarse region would be expected to contain α-phase that appeared more elliptical, representing dendrite arms not growing orthogonal to the cross-section. Lastly, the microstructure in the MP coarse region could be the result of fragmentation of the α-phase lamellae which then grew into spherical particles within the liquid.

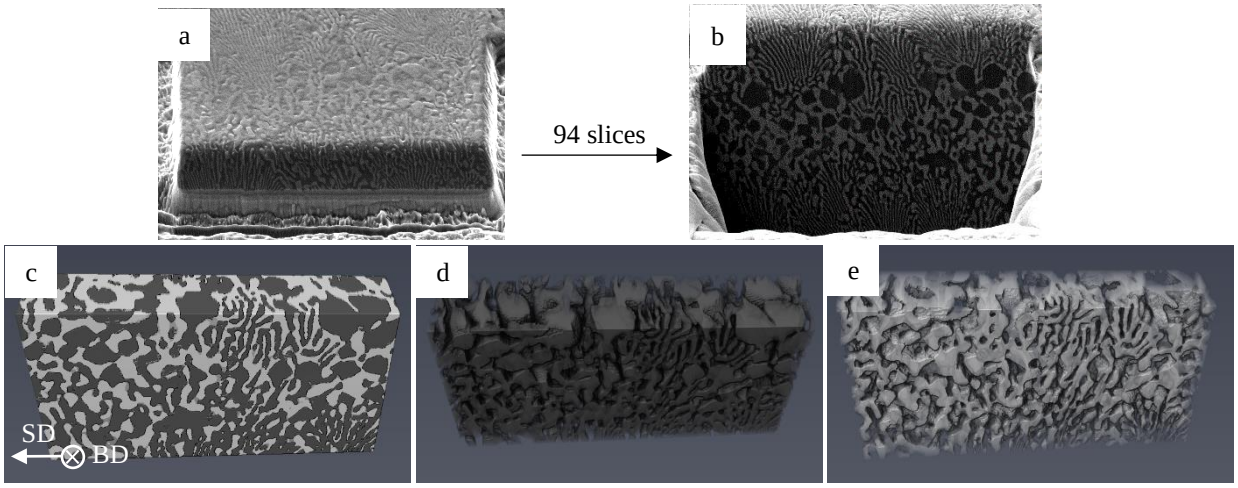

Figure 4-16: Sample prepared for FIB serial cross-sectioning (a) and after 94 slices of the sample had been made (b). A reconstruction of the microstructure at the melt pool boundary was then made (c), allowing both the alpha phase (d) and the theta phase (e) to be separated and their morphologies analyzed.

To gain a better understanding formation of the MP coarse region, FIB serial cross-sectioning was employed so that a 3D representation of the microstructure could be obtained. This was performed on a longitudinal cross-section of a single-track wall, where a U-shaped trench approximately and 3 μm deep was milled away below the melt pool boundary with the FIB. The FIB was then used to mill away 50 nm slices of the area within the U-shaped trench, and an image was taken each time of the newly exposed face. This procedure was repeated automatically with the Auto Slice and View software through the use of fiducial markers that allowed for the software to realign the sample after each section was milled (as explained in

section 2.3.1.1: FIB Cross-sectioning). **Figure 4-16a** shows the U-shaped trench in the sample with the melt pool boundary seen on the surface, while **Figure 4-16b** shows what the sample looked like at the end of the serial cross-sectioning. **Figure 4-16c-e** show the reconstruction of the microstructure made through Avizo software. By separating the two phases, the morphology of the α-phase within the MP coarse region was found to be spherical and not dendritic, while the θ-phase appeared to grow around it. The actual interface between the melt pools could not be determined even within the 3D reconstruction as there was no observed discontinuity of the lamellae, specifically with the θ-phase. This suggests that continuous growth of the individual phases occurs at the melt pool interface similar to what Chadwick observed in his remelting experiments [23].

4.4.2.2: Crystal orientation of eutectic microstructure at MPB

The formation of anomalous eutectic microstructure at the boundary between two laser remelt tracks was studied by Lin, et al., in the Ni-30wt%Sn system [183]. The anomalous eutectic shown in that study near the melt pool boundary appears to have a similar morphology to what is shown in **Figure 4-15**, specifically the presence what appeared to be a spherical Ni (FCC) phase. After performing EBSD on their samples, Lin, et al., showed that the intermetallic Ni_3Sn phase near the melt pool boundary was of one crystal orientation, while the Ni (FCC) face was of various orientations. Some groupings of the Ni spherical phase were found to have the same orientation and were thought to be the cross-section of dendrite arms. It was concluded from this research that the anomalous microstructure was a result of Ni (FCC) phase dendrites being fractured into pieces in the region by the melt pool boundary.

An analogous study was performed in this research, where the crystal orientation of the microstructure at the melt pool boundary was characterized to better understand the solidification mechanism. To do this, a FIB lift out was made spanning the microstructure across a melt pool boundary, including both the HAZ and the MP course regions, as shown in **Figure 4-17**. The FIB lift out was then thinned until the resulting sample in **Figure 4-17b** was produced.

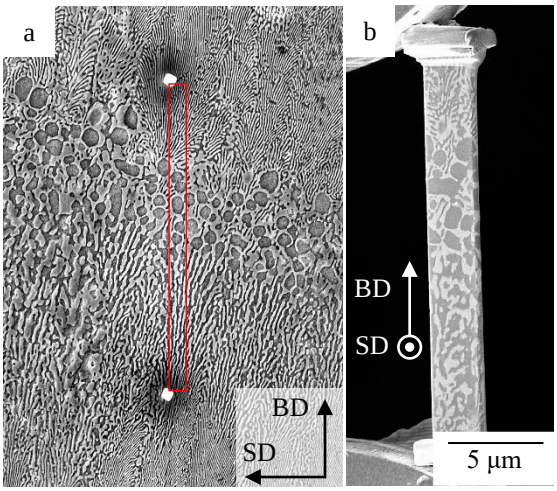

Figure 4-17: Area where a FIB lift out was performed on a longitudinal cross-section of a single-track wall outlined in red (a). Image of the FIB lift out after milling and thinning (b).

TKD was then performed on this sample to obtain the crystallographic orientation of the two phases. Because transmission of the electron beam occurs within this technique, a high spatial resolution was achieved due to the smaller interaction volume, thus allowing a step size of 15 nm to be used. Results of this technique are shown in the form of an Euler map in **Figure 4-18**. In this map it can be see that the crystal orientation of the θ-phase stays consistent across the melt pool boundary while that of the α-phase changes between the HAZ and the MP coarse regions, and then again as it returns to a regular lamellar microstructure. Within the MP coarse region, the α-phase spherical microstructure is oriented in various crystallographic directions,

suggesting that these spheroids grew within the melt pool before epitaxial growth occurred at the melt pool boundary. It is unlikely that these spheroids underwent nucleation within the liquid due to the high amount of undercooling that is necessary for this process to occur, compared to the very low amount of undercooling that is needed for epitaxial growth. It is suspected that the spheroids grow from fragmentation of the α-phase, similar to what is proposed by Lin, et al., although here the fragmentation would be occurring from lamellar rather than dendritic microstructures [183]. Zhang, et al., proposed a similar mechanism of fragmentation of fine lamellae to explain anomalous eutectic growth in the Ni-Si eutectic system [184]. It should be noted that misorientation of the α-phase spheroids does not completely rule out the theory that the MP coarse region is still part of the HAZ since coarsening could also produce this morphology and grains have been observed to rotate at temperatures close to the melting point in the Al-Cu system [185]. That said, the time frames that the grain rotations have been observed at is approximately six orders of magnitude larger than the time scale of the laser exposure and melt pool solidification. This explanation for the misorientation is very unlikely then and implies that rotation or nucleation of the spheroids occurred within the melt pool.

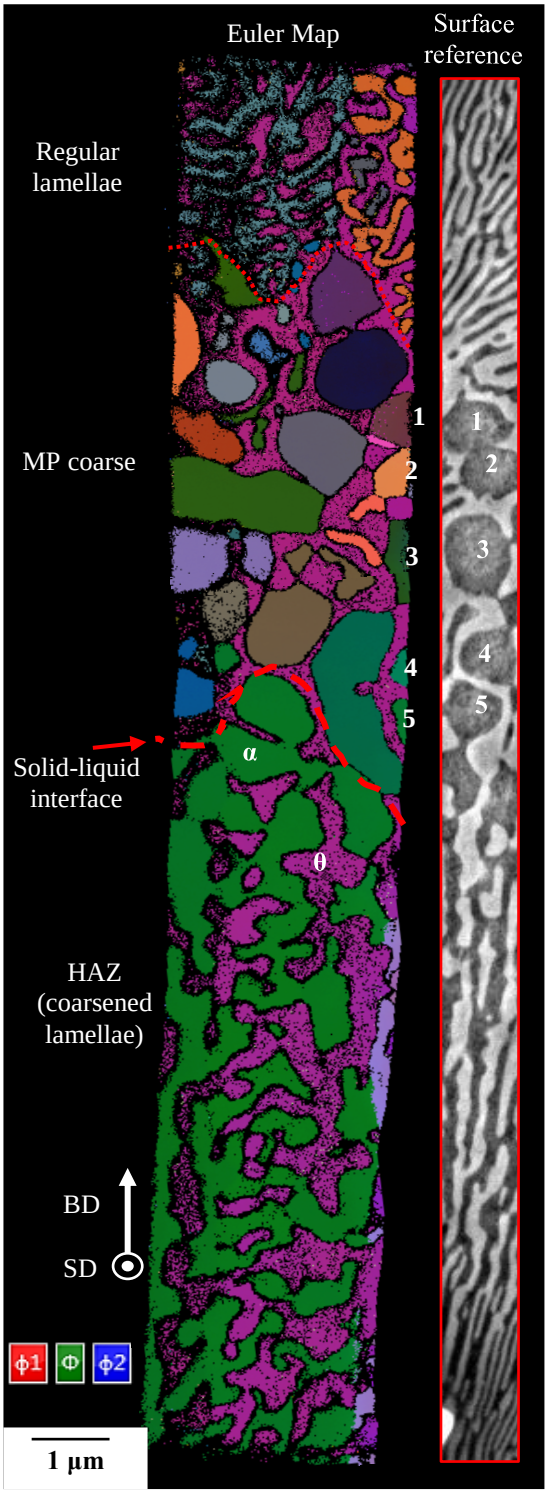

Figure 4-18: Euler map of melt pool boundary showing three distinct regions labeled as the HAZ, MP coarse, and regular lamellae. What appears to be the interface where the solid-liquid interface existed is shown (red dashed line) and a reference image of the surface is shown (red rectangle) with specific α-phase particles numbered for comparison. Epitaxial growth of the θ-phase (purple) can be clearly seen across the melt pool boundary.

The continuation of a single crystallographic orientation of the θ-phase across the melt pool boundary (**Figure 4-18**) shows epitaxial growth is occurring within this phase. It is hypothesized that decoupled growth of the θ-phase occurs at the solid-liquid interface due to growth of the α-phase spheroids changing the local composition of the liquid to be more hypereutectic. Because of the anisotropy within the tetragonal θ-phase, there is a higher driving force then the FCC α-phase to grow along a specific preferred direction, as shown by Chadwick [23]. This, along with the fact that growth of the α-phase spheroids in the melt reduced the local Al concentration, are most likely the causes of why the α-phase is not seen to grow epitaxially across the melt pool boundary. Epitaxial growth of the θ-phase may not have occurred if the growth direction of the seed layer and the new layer had not been in similar orientations, i.e. if the direction of the heat flow had been different between the two layers [186].

When considering the mechanical properties of the melt pool boundary, the epitaxial growth of the θ-phase would eliminate grain boundaries at the interface, and thus mitigate the chances of crack propagation at that location. This may lead to the difference in hardness values shown in **Figure 4-12** of the melt pool boundaries located between parallel and perpendicular line scans. Further research would be needed to better understand what misorientation between the orientation of the seed layer and the direction of the heat flow in the new layer could be reached that would still allow epitaxial growth to occur of the θ-phase in this system.

A schematic of the proposed mechanism of how the microstructure at the melt pool boundary is formed is given in **Figure 4-19**. Upon remelting of the previous layer, a temperature gradient will be present near the solid-liquid interface. The lamellar microstructure directly under

the melt pool will begin to coarsen due to the high temperatures in this region thus creating the HAZ.

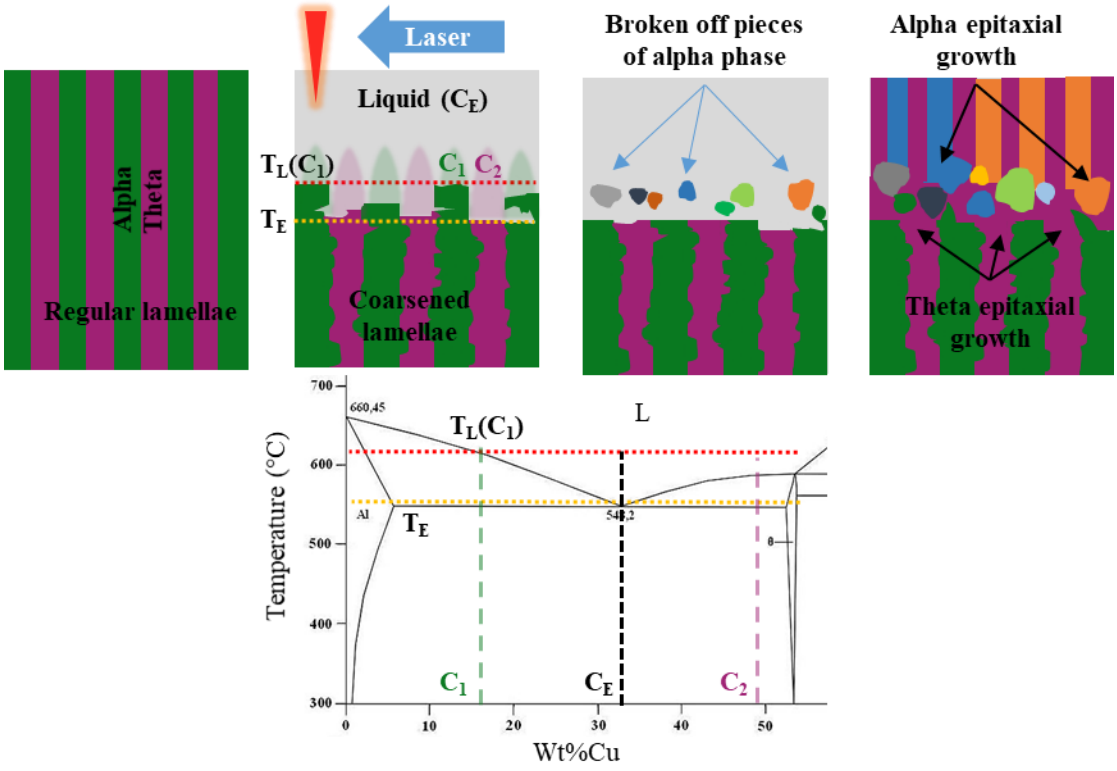

Figure 4-19: Schematic showing mechanism of alpha phase fragmentation and formation of microstructure at melt pool boundary. It is proposed that fragmentation occurs due to both the temperature gradient at the solid-liquid and local fluctuations of the composition.

Immediately after the melt pool is formed, it is proposed that local fluctuations in the composition will occur, with hypoeutectic and hypereutectic compositions being located above the alpha and theta phases respectively. This is due to the different compositions between the two phases and the diffusion that must occur to bring the liquid to a homogenous composition. These compositional fluctuations are denoted by the faded green and purple hemispheres above the lamellae and by the lines C_1 (hypoeutectic) and C_2 (hypereutectic) on the phase diagram.

Because the α-phase can be at equilibrium within a hypoeutectic liquid at higher temperatures than the θ-phase can exist in a hypereutectic liquid, it is proposed that the α-phase lamellae will protrude into the liquid further than the θ-phase lamellae. This protrusion will be dependent on the thermal gradient (G) of the melt pool, with longer protrusions occurring with a lower G. Fragmentation of the α-phase lamellae protrusions is likely to occur as hypereutectic liquid erodes the base of these protrusions. Similar fragmentation scenarios have been observed in dendritic microstructures in both experimental and phase field modelling studies [187,188]. Thus fragmentation and melting of the broken pieces would occur until the melt pool decreases in temperature to where growth of the alpha particles begin to occur creating the α-phase spheroids observed in the MP coarse region. As the melt pool continues to decrease in temperature below the eutectic liquidus line (T_E) the θ-phase will begin to grow epitaxially from the seed layer, and lock the α-phase spheroids into their various orientations. As the θ-phase moves past the α-phase spheroids coupled growth will begin to occur between the two phases forming a regular lamellar microstructure, with the α-phase likely growing epitaxially from one spheroids oriented close to the growth direction.

4.4.3: Conclusions

Characterization of the morphology and crystallographic orientation of the microstructure at melt pool boundaries were performed in this study to better understand the solidification mechanism. Both a HAZ and MP coarse region were distinguished at the melt pool boundary within this system and compared with similar microstructures observed in LPBF processed AlSi10Mg samples found in the literature. The 3-dimensional morphology of the MP coarse

region was characterized through FIB serial cross-sectioning which showed that the α-phase forms spheroids near the interface rather than dendrites as has been reported in other eutectic systems. Further characterization was performed through TKD of a FIB lift out sample that spanned the microstructure at the melt pool boundary within an LPBF made sample. The crystallographic information gained from this technique showed that epitaxial growth occurs between the two layers in the θ-phase but not in the α-phase, and that the α-phase spheroids consisted of various orientations. These results suggest that decoupled growth occurs at the melt pool boundary, but changes to coupled growth after the MP coarse region. The mechanism that caused the formation of the α-phase spheroids was then proposed involving local composition fluctuations in the melt pool that lead to the fragmentation of α-phase lamellae. These fragments were then thought to grow into the spheroids observed in the MP coarse region and get locked into their various orientations once the θ-phase solidification front moves past them. These findings provide a fundamental understanding of how the microstructure at the melt pool boundary forms which may lead to the ability to improve or even utilize the properties at these boundaries within materials.

Chapter 5 : Summary and future work

5.1: Summary of research

The solidification of Al-Cu eutectic alloy after laser melting is studied in this dissertation with a specific focus on the microstructures formed through the LPBF processing method. The work performed here can be divided into two main ideas: the use of the Al-Cu eutectic microstructure as a recording device for solidification phenomena that occur within the LPBF process, and the use of the LPBF processing parameters to control the eutectic microstructure and mechanical properties of the Al-Cu system. The $L \rightarrow S_1+S_2$ eutectic reaction is here used as both an in-situ detector of the thermal history and composition of the powder and melt pool, as well as a method to modulate the mechanical properties of the system due to the direct correlation between the steady-state solidification velocity of the melt pool and the interlamellar spacing of the bulk microstructure. Thus, the overarching goals of this research were two-fold: employ the eutectic microstructure within the LPBF process to elucidate specific information that would otherwise require extensive in-situ characterization to obtain; and to lay the ground work for functional gradient and hierarchical designs by further establishing the relationships between processing parameters, microstructure and mechanical properties.

The first half of this research goal was met by identifying three specific situations where the Al-Cu eutectic microstructure could be used to better understand processing phenomena that were occurring during LPBF. These situations included:

1) Morphology changes that were observed to occur in recycled Al-Cu and Al powder after laser irradiation in LPBF.

2) Quantifying compositional fluctuations within in-situ alloyed Al-Cu during LPBF.
3) Correlating melt pool fluctuations with microstructure variations and laser power instabilities.

Significant results concluded from these studies can be summarized in the following:

1) First, a mechanism of powder degradation within LPBF was discovered that has not been previously reported in the literature. It was shown here that low power irradiation can melt Al-Cu particles without sintering or agglomeration, and that this can occur along the edges of the laser beam at standard processing conditions within LPBF. Characterization of particles both before and after laser irradiation showed that dent and rift like morphologies formed in the remelted particles, decreasing their sphericity, and potential flowability if recycled. The eutectic microstructure was used in this study to show whether melting occurred in laser irradiated particles, as well as to relate the direction of the solidification to the formed dent and rift features. From these results, it was deduced that the oxide shell of the particles retains its continuity throughout the melting and thermal expansion of the particle, and that the observed collapsed and dented features were products of buckling within this oxide shell as the particle contracted during cooling and solidification. This work provides an explanation for some of the morphologies of LPBF recycled powder that have previously appeared in the literature [67,78].
2) Next, a novel approach to quantifying the degree of elemental mixing within in situ alloyed Al-33wt%Cu was developed by leveraging the narrow composition range required to produce the eutectic microstructure. This was performed through the use of SEM and image analysis, and qualitatively through the use of Vickers microhardness

testing, on samples made with four different powder blends of varying particle size. Results showed that more compositionally homogenous microstructures occurred in samples made from blends of smaller powder sizes (2-9 um). For all samples, it was shown that increasing the laser power, and thus the melt pool size, decreased the amount of hypo- or hypereutectic regions within the sample. Dry segregation of elemental powder within the spread powder layer was observed to be the primary cause of large regions of hypo- and hypereutectic microstructures. Blends with larger powder were shown to be more adversely affected by dry segregation due to the relative size of the particles with respect to the dimensions of the melt pool as well as their lower surface area to volume ratio. The selection of elemental particle sizes for blends should also be balanced with the rheology of the powder blend, specifically the compression and flowability of the feedstock powder. It was shown in this study that blends with larger elemental particles produced a better flowability and compressibility than blends with smaller particles. These results provided the groundwork for a rational design of elemental powder blends made to optimize mixing during in situ alloying at a given set of laser parameters.

3) Lastly, banded microstructures in the Al-Cu eutectic alloy were correlated to fluctuations in laser induced melt pools, providing information on the change in the velocity of the solid-liquid interface and the location where these fluctuations occurred. Causes of melt pool fluctuations were linked to sudden changes in the melt pool depth caused by underlying pores or changes in the microstructure of the bulk that was being remelted. External sources of melt pool fluctuations were also investigated, such as power instabilities in the laser beam. To do this, the distance between banded microstructures

was measured for line scans made at three different laser velocities, and the frequency of occurrence was found to be comparable with power instabilities known to occur in the laser system used.

The second half of the overarching goal of this work was met by studying the relationship between the processing parameters and the various eutectic microstructures formed, as well as the hardness values obtained from these microstructures. Key results from these studies include a verification that increasing laser scan velocities decreases the interlamellar spacing according to the Jackson and Hunt model, indicating that the melt pool undergoes stead-state solidification regardless of the laser power, within the parameter matrix studied. It was then shown that the widths of the eutectic colonies within these samples did not deviate from between 1-3 μm with either changes in laser power or scan velocity. Characterization of a colony boundary using STEM EDS showed that Si was present within the sample, specifically within the θ-phase, suggesting that the colony boundary width may have been controlled by the degree of constitutional supercooling that was caused by the tertiary element. The microstructures formed at laser scan velocities that induce rapid solidification of the Al-Cu system were then characterized along with the hardness values of these microstructures. It was shown from these experiments that the hardness increases according to a Hall-Petch relationship as the lamellar microstructure is refined at higher scan velocities, but then decreases in a similar trend as the lamellar microstructure decomposes into a dendritic microstructure, and finally a metastable solid-solution phase, as the scan velocity increased.

Microhardness measurements were taken of melt pool boundaries between line scans made at a range of velocities, and at different orientations to each other. The average hardness of the melt

pool boundaries were found to be less than that of the bulk up until a scan velocity of approximately 500 mm/s, after which the melt pool boundaries were found to be harder than the center of the line scan. This was shown to be due to the difference in solidification velocity between the edge of the melt pool and the center of the melt pool; when the microstructure at the center of the line scan consisted of fine lamellae, the edge would have a coarse lamellar microstructure and thus be softer, but when the center consisted of a dendritic microstructure, the edge of the line scan contained a fine lamellar microstructure. A distinction between the hardness of the boundaries between line scans oriented parallel and those oriented perpendicular to each other was also observed, with melt pool boundaries between perpendicular line scan containing a higher average hardness than the parallel line scans. This is believed to be due to the fact that perpendicular line scans have the same solidification direction in the center of one line and the edge in the other, thus making it conducive for epitaxial growth to occur. Boundaries between overlapped parallel line scans would have different growth directions at the edge and middle, and therefor would be more likely to nucleate grains that are aligned to the growth direction. Because epitaxial growth would reduce the grain boundaries at the melt pool interface, it is expected that these boundaries would be stronger.

Lastly, the melt pool boundaries formed within LPBF process Al-Cu eutectic samples were further characterized to better understand the how the microstructure is formed at these interfaces. To do this, the morphology of the microstructure was first characterized through serial cross-sectioning so that a 3D reconstruction of the microstructure could be made. This showed that spherical α-phase particles were present directly below the regular lamellae of the new layer. The crystal orientation of the two phases at the melt pool boundary were then characterized through TKD of a FIB lift out sample. The results of this analysis showed that the crystal

orientation of the θ-phase was consistent across the melt pool boundary, while the orientation of the α-phase changed between the HAZ and the regular lamellae in the new layer. The spherical α-phase was oriented in various crystallographic directions suggesting that these particles either nucleated and grew in an undercooled liquid, or were fragmentations of the α-phase lamellae that spheroidized in the liquid. Because only a minimum undercooling would be needed for epitaxial growth of the θ-phase to occur, fragmentation was selected as the more likely explanation, and a mechanism of how α-phase fragmentation could occur within a lamellar microstructure was proposed.

The results of this work will aid in the continued research of LPBF by not only providing detailed insight into specific aspects of the process such as showing a new mechanism of recycled powder degradation, or providing guidelines to powder blend design for in-situ alloying, but also by showing how the eutectic microstructure can be used for alternative methods of characterization. Along with this, it has been demonstrated how multiple microstructures with different mechanical properties might be formed from the eutectic composition simply through changes in the laser parameters and scan strategies. These results help establish a foundation for further research focused on creating functional gradient material and internal designs with eutectic alloys.

5.2: Future work

Although funding has ended for this project, continued research in several specific areas may provide valuable results that could improve the LPBF processing method. These include:

- Quantifying the percentage of particles that undergo melting and morphology changes with respect to area scanned within an LPBF build layer using the change in eutectic microstructure of Al-Cu powder, and then relate this to changes in the flowability of the powder sample.
- Investigating whether the dent and rift morphologies observed in Al and Al-Cu powder occur in more commonly used Al-based feedstock powders such as Al-10wt%Si-Mg.
- Correlating direct observations of melt pool fluctuations in laser irradiated Al-Cu with eutectic banding events through high-speed X-ray imaging technique established at the I-32 beam line at Argonne National Lab.
- Processing bulk samples to test mechanical properties (tension or compression) of various microstructures available in this system, along with anisotropy caused by different orientations of melt pool boundaries within the sample.

Beyond these studies, further investigation into the mechanical properties of various microstructure designs should be performed to take full advantage of the 3-dimensional control of the Al-Cu microstructure through LPBF as established in this work. This may be performed in the characterization of the mechanical properties achieved through three possible designs approaches: functional gradients, internal geometries and hierarchical structures. A brief discussion and example of each of these designs within the Al-Cu system are given below.

5.2.1: Functional gradients

Eutectic alloys have been used to produce functional gradients ever since the early 19th century, when ploughshares were first made out of cast iron, with one side being cooled faster than the other so a hard and soft surface were formed, thus causing the tool to be continuously sharp as one side wore away faster than the other [189]. Today, the LPBF process has the potential to take advantage of the variation of mechanical properties possible in eutectic alloys by forming functional gradients throughout the volume of a built part. A schematic of the different microstructures and hardness values available within LPBF processed Al-Cu, along with an example of different layers produced in a sample that were made at different scan velocities and directions are both shown in **Figure 5-1**.

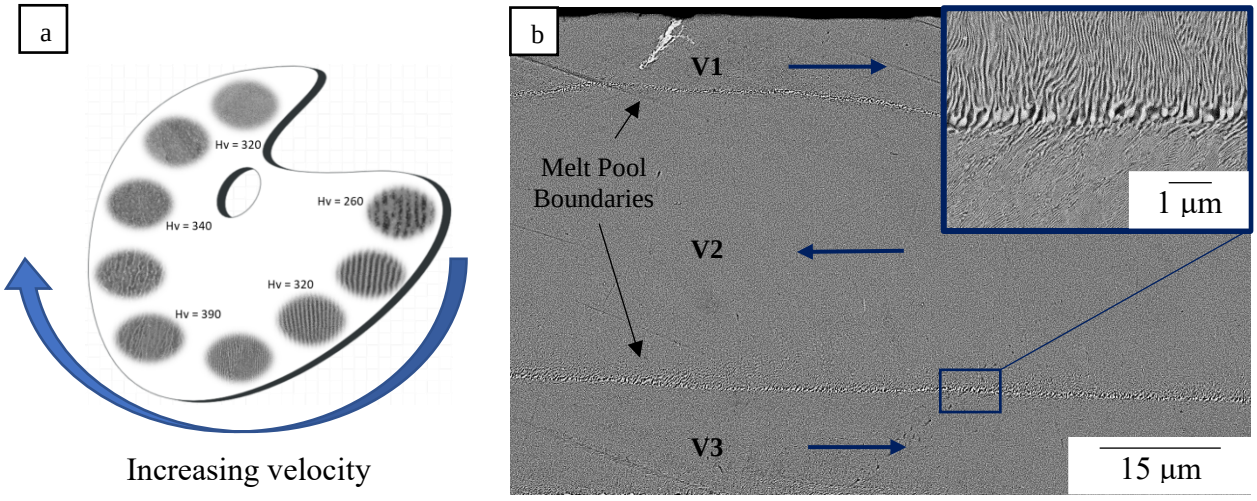

Figure 5-1: "Pallet" of microstructures and range of hardness values that can be achieved in LPBF processed Al-Cu eutectic alloy (a). Longitudinal cross-section of three line scans performed at different velocities and different directions with inset showing the difference in interlamellar spacing between two of the layers.

5.2.2: Internal geometries

Given the freedom of possible scan strategies within LPBF, secondary geometries can be overlaid on the first, causing the laser to remelt the built part in specified areas at each build layer. Due to the directional solidification of Al-Cu eutectic, along with the unique microstructures that form at the melt pool boundaries within this system, internal geometries may provide significant design freedoms in regards to the specific mechanical response of the built part. An example of this type of design is shown in **Figure 5-2**.

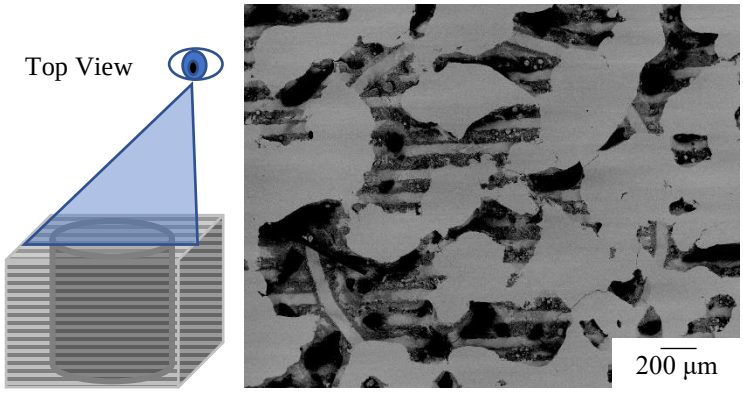

Figure 5-2: Internal tube geometry made within a unidirectional scanned rectangle by remelting the secondary geometry after each layer. Micrograph shows a view of the top surface where the remelted circular geometry can clearly be seen within the parallel line scans.

5.2.3: Hierarchical structures

Motifs for hierarchical structures have often been inspired by designs found in nature, such as the microstructure within the shell of the *Lobats gigas*, or conch [190]. These designs have been shown to provide superrerior fracture toughness by diverting crack propagation [157]. The Al-Cu lamellar microstructure provides two levels of structrure in the form of both colonies and the lamellae within them. When paired with LPBF, the melt pools boundaries add a third level of structure, all

of which can be produced within wide range of geometries available to the LPBF process. An example of these different level of structures within a LPBF processed sampel, along with a comparison of the hierarchical structure found in the conch shell, are shown in **Figure 5-3**.

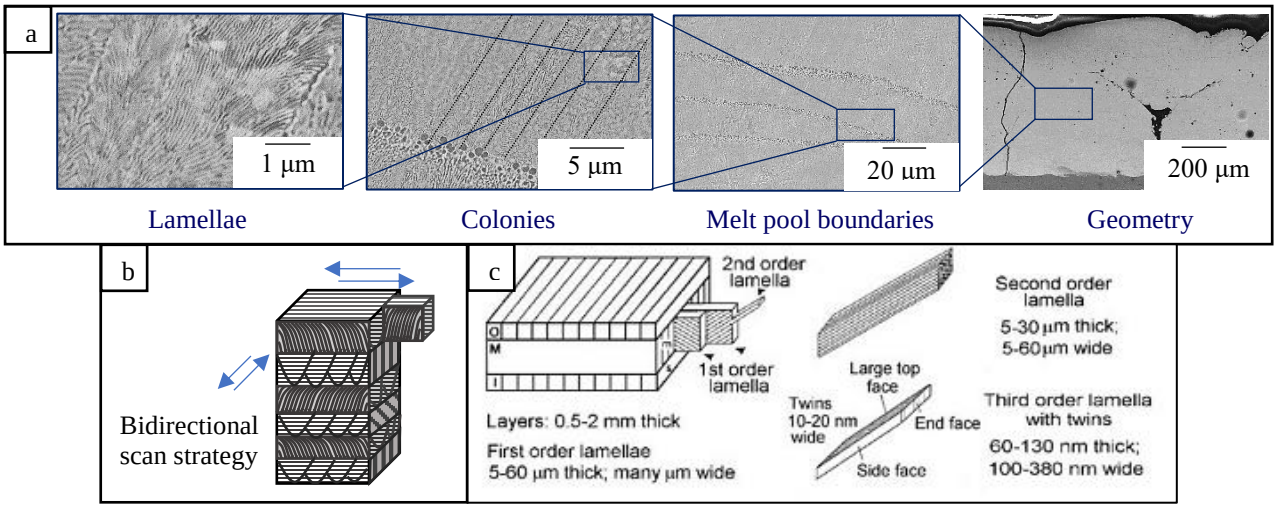

Figure 5-3: Hierarchical structure within an Al-Cu eutectic sample processed through LPBF showing three layers of structure including: lamellae, colony boundaries (black lines) and melt pool boundaries (a). Hypothetical design that could be used to mimic hierarchical structure found in the conch shell (b). Schematic of microstructure observed in the conch shell (c)[190].

In summary the processing of eutectic alloys within LPBF provides a rich area of research where the relation between the laser parameters and the eutectic microstructure can be leveraged as both a tool to better understand solidification phenomenon, and as a method to create advance material designs. Further research in this area may lead to both improvements in the LPBF process as well as an expansion of the design freedoms in LPBF built parts.

References

1. Park, S. & Yoon, H. J. New Approach for Large-Area Thermoelectric Junctions with a Liquid Eutectic Gallium–Indium Electrode. *Nano Lett.* **18**, 7715–7718 (2018).

2. Wu, H.-J., Foo, W.-J., Chen, S.-W. & Snyder, G. J. Ternary eutectic growth of nanostructured thermoelectric Ag-Pb-Te materials. *Cit. Appl. Phys. Lett* **101**, 143906 (2012).

3. Norizan, M. N. *et al.* Fabrication and thermoelectric property of nanostructured Si/Cr0.8Mn0.2Si2 eutectic alloy by melt-spinning. *Mater. Res. Express* **6**, (2019).

4. Pawlak, D. A. *et al.* How far are we from making metamaterials by self-organization? the microstructure of highly anisotropic particles with an SRR-like geometry. *Adv. Funct. Mater.* **20**, 1116–1124 (2010).

5. Kim, J. *et al.* Template-Directed Directionally Solidifi ed 3D Mesostructured AgCl-KCl Eutectic Photonic Crystals. *Adv. Mater.* **27**, 4551–4559 (2015).

6. Zehetbauer, M. J. & Zhu, Y. T. *Bulk Nanostructured Materials*. (Wiley-VCH Verlag GmbH & Co., 2009).

7. Zimmermann, M., Karma, A. & Carrard, M. Oscillatory lamellar microstructure in off-eutectic Al-Cu alloys. *Phys. Rev. B* **42**, 833–837 (1990).

8. Zimmermann, M., Carrard, M. & Kurz, W. Rapid solidification of Al-Cu eutectic alloy by laser remelting. *Acta Met.* **37**, 3305–3313 (1989).

9. Kang, N., Coddet, P., Dembinski, L., Liao, H. & Coddet, C. Microstructure and strength analysis of eutectic Al-Si alloy in-situ manufactured using selective laser melting from elemental powder mixture. *J. Alloys Compd.* **691**, 316–322 (2017).

10. Trevisan, F. *et al.* On the selective laser melting (SLM) of the AlSi10Mg alloy: Process, microstructure, and mechanical properties. *Materials (Basel).* **10**, (2017).

11. Vora, P., Mumtaz, K., Todd, I. & Hopkinson, N. AlSi12 in-situ alloy formation and residual stress reduction using anchorless selective laser melting. *Addit. Manuf.* (2015) doi:10.1016/j.addma.2015.06.003.

12. Dadbakhsh, S. & Hao, L. Effect of Al alloys on selective laser melting behaviour and microstructure of in situ formed particle reinforced composites. *J. Alloys Compd.* (2012) doi:10.1016/j.jallcom.2012.06.097.

13. Pauly, S., Wang, P., Kühn, U. & Kosiba, K. Experimental determination of cooling rates in selectively laser-melted eutectic Al-33Cu. *Addit. Manuf.* **22**, 753–757 (2018).

14. Liu, G., Xie, D., Wang, S., Misra, A. & Wang, J. Mesoscale crystal plasticity modeling of

nanoscale Al-Al2Cu eutectic alloy. *Int. J. Plast.* **121**, 1–19 (2019).

15. Tiwary, C. S., Roy Mahapatra, D. & Chattopadhyay, K. Effect of length scale on mechanical properties of Al-Cu eutectic alloy. *Appl. Phys. Lett.* **101**, (2012).

16. Gladman, T. Precipitation hardening in metals. *Mater. Sci. Technol.* **15**, 30–36 (1999).

17. Polmear, I. J., StJohn, D., Nie, J.-F. & Qian, M. *Light alloys : metallurgy of the light metals*.

18. Vasudévan, A. K., Przystupa, M. A. & Fricke, W. G. Effect of composition on crystallographic texture in hot-rolled Al-Li-Cu alloys. *Mater. Sci. Eng. A* **208**, 172–180 (1996).

19. Hargarter, H., Lyttle, M. T. I. & Starke, E. A. Effects of preferentially aligned precipitates on plastic anisotropy in Al-Cu-Mg-Ag and Al-Cu alloys. *Mater. Sci. Eng. A* **257**, 87–99 (1998).

20. Okayasu, M., Sato, R. & Takasu, S. Effects of anisotropic microstructure of continuous cast Al-Cu eutectic alloys on their fatigue and tensile properties. *Int. J. Fatigue* **42**, 45–56 (2012).

21. Guthrie, F. On eutexia. *Proc. Phys. Soc. London* **6**, 124–146 (1884).

22. Kerr, H. W. & Winegard, W. C. Solidification of eutectic alloys. *Jom* **18**, 563–569 (1966).

23. Chadwick, G. A. Eutectic alloy solidification. *Prog. Mater. Sci.* **12**, 99–182 (1963).

24. Winegard, W. C., Majka, S., Thall, B. M. & Chambers, B. Eutectic Solidification in Metals. *Can. J. Chem.* **29**, 320 (1951).

25. Chilton, J. P. & Winegard, W. C. Solidification of a Eutectic Made from Zone-Refined Lead and Tin. *J. Inst. Met.* **89**, 162–164 (1961).

26. Tiller, W. A., Jackson, K. A., Rutter, J. W. & Chalmers, B. The redistribution of solute atoms during the solidification of metals. *Acta Metall.* **1**, 428–437 (1953).

27. Jackson, K. A. & Hunt, J. D. Lamellar and Rod Eutectic Growth. *Dyn. Curved Front.* 363–376 (1988) doi:10.1016/B978-0-08-092523-3.50040-X.

28. Porter, D. A. & Easterling, K. E. *Phase Transformations in Metals and Alloys*. (Chapman & Hall, 1992).

29. Livingston, J. D., Cline, H. E., Koch, E. F. & Russell, R. R. High-speed solidification of several eutectic alloys. *Acta Metall.* **18**, 399–404 (1970).

30. Su, Y., Lin, X., Wang, M., Xue, L. & Huang, W. Lamellar structures in laser surface remelted Zn–Cu peritectic alloy under ultra-high temperature gradient. *Scr. Mater.* **51**,

397–403 (2004).

31. Gill, S. C., Zimmermann, M. & Kurz, W. Laser resolidification of the AlAl2Cu eutectic: The coupled zone. *Acta Metall. Mater.* **40**, 2895–2906 (1992).

32. Mcalister, A. J. *Al (Aluminum) Binary Alloy Phase Diagrams*. *Alloy Phase Diagrams* vol. 5 (2018).

33. Bogno, A.-A. A., Khatibi, P. D., Henein, H. & Gandin, C.-A. A. Quantification of Primary Dendritic and Secondary Eutectic Nucleation Undercoolings in Rapidly Solidified Hypo-Eutectic Al-Cu Droplets. *Metall. Mater. Trans. A Phys. Metall. Mater. Sci.* **47**, 4606–4615 (2016).

34. Wang, S. & Fan, C. Crystal structures of Al2Cu revisited: Understanding existing phases and exploring other potential phases. *Metals (Basel).* **9**, (2019).

35. Chadwick, G. A. Yield Point Analyses in Eutectic Alloys. *Acta Metall.* **24**, 1137–1146 (1976).

36. Trivedi, R., Magnin, P. & Kurz, W. Theory of eutectic growth under rapid solidification conditions. *Acta Metall.* **35**, 971–980 (1987).

37. Gill, S. C. & Kurz, W. Rapidly solidified AlCu alloys-I. experimental determination of the microstructure selection map. *Acta Metall. Mater.* **41**, 3563–3573 (1993).

38. Irrinki, H., Nath, S. D., Akilan, A. A. & Atre, S. V. Laser Powder Bed Fusion. in *Additive Manufacturing Processes* vol. 24 209–219 (2020).

39. Leong Sing, S., An, J., Yeong, W. Y. & Wiria, F. E. Laser and Electron-Beam Powder-Bed Additive Manufacturing of Metallic Implants: A Review on Processes, Materials and Designs. *J Orthop Res* **34**, 369–385 (2016).

40. Wilkes, J., Hagedorn, Y. C., Meiners, W. & Wissenbach, K. Additive manufacturing of ZrO2-Al2O3ceramic components by selective laser melting. *Rapid Prototyp. J.* **19**, 51–57 (2013).

41. Spears, T. G. & Gold, S. A. In-process sensing in selective laser melting (SLM) additive manufacturing. *Integr. Mater. Manuf. Innov.* **5**, 2 (2016).

42. Yang, L. *et al. Additive Materials, Design and Metals: The Technology, Manufacturing of Production*. (2017). doi:10.1007/978-3-319-55128-9_4.

43. Scipioni Bertoli, U., Wolfer, A. J., Matthews, M. J., Delplanque, J.-P. R. & Schoenung, J. M. On the limitations of Volumetric Energy Density as a design parameter for Selective Laser Melting. *Mater. Des.* **113**, 331–340 (2017).

44. Prashanth, K. G., Scudino, S., Maity, T., Das, J. & Eckert, J. Is the energy density a

reliable parameter for materials synthesis by selective laser melting? *Mater. Res. Lett.* **5**, 386–390 (2017).

45. Guo, Q. *et al.* In-situ characterization and quantification of melt pool variation under constant input energy density in laser powder bed fusion additive manufacturing process. *Addit. Manuf.* **28**, 600–609 (2019).

46. Qin, H. *et al.* Solidification pattern, microstructure and texture development in Laser Powder Bed Fusion (LPBF) of Al10SiMg alloy. *Mater. Charact.* **145**, 29–38 (2018).

47. Mazzoli, A. & Favoni, O. Particle size, size distribution and morphological evaluation of airborne dust particles of diverse woods by Scanning Electron Microscopy and image processing program. *Powder Technol.* **225**, 65–71 (2012).

48. Igathinathane, C., Pordesimo, L. O., Columbus, E. P., Batchelor, W. D. & Methuku, S. R. Shape identification and particles size distribution from basic shape parameters using ImageJ. *Comput. Electron. Agric.* **63**, 168–182 (2008).

49. Seiler, H. Secondary electron emission in the scanning electron microscope. *J. Appl. Phys.* **54**, (1983).

50. Tryblom, A. Optimizing Transmission Kikuchi Diffraction for Analysing Grain Size and Orientation of Nanocrystalline Coatings. (2015).

51. Søgaard, S., Bryder, M., Allesø, M. & Rantanen, J. Characterization of powder properties using a powder rheometer. *Proc. Electron. Conf. Pharm. Sci.* **2**, (2012).

52. ASTM E93-17. Vickers Hardness and Knoop Hardness of Metallic Materials. vol. E92 − 17 1–27 (2017).

53. Trivedi, R., Jin, F. & Anderson, I. E. E. Dynamical evolution of microstructure in finely atomized droplets of Al-Si alloys. *Acta Mater.* **51**, 289–300 (2003).

54. Prasad, A., Mosbah, S., Henein, H. & Gandin, C.-A. A Solidification Model for Atomization. *ISIJ Int.* **49**, 992–999 (2009).

55. Prasad, A. *Microsegregation studies of rapidly solidified binary Al-Cu alloys*. (University of Alberta, 2006).

56. Srivastava, R. M., Eckert, J., Löser, W., Dhindaw, B. K. & Schultz, L. Cooling rate evaluation for bulk amorphous alloys from eutectic microstructures in casting processes. *Mater. Trans.* **43**, 1670–1675 (2002).

57. Takeshita, K. & Shingu, P. H. The Undercooling Attainable by the Rapid Quenching of Al-CuAl2 Eutectic Alloy Melt argon atmosphere and converted to a thin film. *Trans. Japan Inst. Met.* **27**, 180–186 (1986).

58. Kurz, W. & Trivedi, R. Banded solidification microstructures. *Metall. Mater. Trans. A Phys. Metall. Mater. Sci.* **27**, 625–634 (1996).

59. Garland JG & Davies GJ. Surface Rippling and Growth Perturbations During Weld Pool Solidification. *Metal Constr Brit Weld J* vol. 2 171–175 (1970).

60. Kotecki, D., Cheever, D. & Howden, D. Mechanism of Ripple Formation During Weld Solidification. *Weld. J.* **51 N**, (1972).

61. Bennett, W. S. & Mills, G. S. Gta Weldability Studies on High Manganese Stainless Steel. *Weld. J. (Miami, Fla)* **53**, (1974).

62. Cunningham, R. *et al.* Keyhole threshold and morphology in laser melting revealed by ultrahigh-speed x-ray imaging. *Science (80-.).* **363**, 849–852 (2019).

63. Ewald, S. *et al.* Rapid alloy development of extremely high-alloyed metals using powder blends in laser powder bed fusion. *Materials (Basel).* **12**, 1–15 (2019).

64. Haase, C., Tang, F., Wilms, M. B., Weisheit, A. & Hallstedt, B. Combining thermodynamic modeling and 3D printing of elemental powder blends for high-throughput investigation of high-entropy alloys – Towards rapid alloy screening and design. *Mater. Sci. Eng. A* **688**, 180–189 (2017).

65. Strondl, A., Lyckfeldt, O., Brodin, H. & Ackelid, U. Characterization and Control of Powder Properties for Additive Manufacturing. *Miner. Met. Mater. Soc.* **37**, 549–554 (2015).

66. Maamoun, A. H., Elbestawi, M., Dosbaeva, G. K. & Veldhuis, S. C. Thermal post-processing of AlSi10Mg parts produced by Selective Laser Melting using recycled powder. *Addit. Manuf.* **21**, 234–247 (2018).

67. Lutter-Günther, M. *et al.* Spatter formation during laser beam melting of AlSi10Mg and effects on powder quality. *Procedia CIRP* **74**, 33–38 (2018).

68. Gunenthiram, V. *et al.* Experimental analysis of spatter generation and melt-pool behavior during the powder bed laser beam melting process. *J. Mater. Process. Technol.* **251**, 376–386 (2018).

69. Wang, D. *et al.* Mechanisms and characteristics of spatter generation in SLM processing and its effect on the properties. *Mater. Des.* **117**, 121–130 (2017).

70. Leung, C. L. A. *et al.* The effect of powder oxidation on defect formation in laser additive manufacturing. *Acta Mater.* **166**, 294–305 (2019).

71. Slotwinski, J. A. & Garboczi, E. J. Metrology Needs for Metal Additive Manufacturing Powders. *Jom* **67**, 538–543 (2015).

72. Slotwinski, J. A. *et al.* Characterization of Metal Powders Used for Additive Manufacturing. *J. Res. Natl. Inst. Stand. Technol.* **119**, 460–93 (2014).

73. Ardila, L. C. *et al.* Effect of IN718 recycled powder reuse on properties of parts manufactured by means of Selective Laser Melting. *Phys. Procedia* **56**, 99–107 (2014).

74. Wang, D. *et al.* Influence of spatter particles contamination on densification behavior and tensile properties of CoCrW manufactured by selective laser melting. *Opt. Laser Technol.* **121**, 105678 (2020).

75. Clayton, J., Millington-Smith, D. & Armstrong, B. The Application of Powder Rheology in Additive Manufacturing. *Jom* **67**, 544–548 (2015).

76. Tan, J. H., Wong, W. L. E. & Dalgarno, K. W. An overview of powder granulometry on feedstock and part performance in the selective laser melting process. *Addit. Manuf.* **18**, 228–255 (2017).

77. Louvis, E., Fox, P. & Sutcliffe, C. J. Selective laser melting of aluminium components. *J. Mater. Process. Technol.* **211**, 275–284 (2011).

78. Asgari, H., Baxter, C., Hosseinkhani, K. & Mohammadi, M. On microstructure and mechanical properties of additively manufactured AlSi10Mg_200C using recycled powder. *Mater. Sci. Eng. A* **707**, 148–158 (2017).

79. Simonelli, M. *et al.* A Study on the Laser Spatter and the Oxidation Reactions During Selective Laser Melting of 316L Stainless Steel, Al-Si10-Mg, and Ti-6Al-4V. *Metall. Mater. Trans. A* **46**, 3842–3851 (2015).

80. Popov, V. V., Katz-Demyanetz, A., Garkun, A. & Bamberger, M. The effect of powder recycling on the mechanical properties and microstructure of electron beam melted Ti-6Al-4 V specimens. *Addit. Manuf.* **22**, 834–843 (2018).

81. Taheri Andani, M., Dehghani, R., Karamooz-Ravari, M. R., Mirzaeifar, R. & Ni, J. A study on the effect of energy input on spatter particles creation during selective laser melting process. *Addit. Manuf.* **20**, 33–43 (2018).

82. Ahmed, F. *et al.* Study of powder recycling and its effect on printed parts during laser powder-bed fusion of 17-4 PH stainless steel. *J. Mater. Process. Technol.* **278**, 116522 (2020).

83. Gruber, H., Karimi, P., Hryha, E. & Nyborg, L. Effect of Powder Recycling on the Fracture Behavior of Electron Beam Melted Alloy 718. *Powder Metall. Prog.* **18**, 40–48 (2018).

84. Yablokova, G. *et al.* Rheological behavior of β-Ti and NiTi powders produced by atomization for SLM production of open porous orthopedic implants. *Powder Technol.* **283**, 199–209 (2015).

85. Simonelli, M. *et al.* A comparison of Ti-6Al-4V in-situ alloying in Selective Laser Melting using simply-mixed and satellited powder blend feedstocks. *Mater. Charact.* **143**, 118–126 (2018).

86. Mueller, B. A. & Perepezko, J. H. Microstructure development in undercooled Al□Al2Cu alloys. *Mater. Sci. Eng.* **98**, 153–156 (1988).

87. Martin, J. H. *et al.* 3D printing of high-strength aluminium alloys. *Nature* **549**, 365–369 (2017).

88. Kurz, W. & Fisher, D. J. *Fundamentals of Solidification*. (Trans Tech Publications LTD, 1998).

89. Saif, M. T. A., Zhang, S., Haque, A. & Hsia, K. J. Effect of native Al 2 O 3 on the elastic response of nanoscale Al films. *Acta Mater.* **50**, 2779–2786 (2002).

90. Smeltzer, W. W. Oxidation of Aluminum in the Temperature Range 400°−600°C. *J. Electrochem. Soc.* **103**, 209–214 (1956).

91. Son, K. A. *et al.* Growth and Oxidation of Thin Film Al 2Cu. *J. Electrochem. Soc.* **148**, 260–263 (2001).

92. Leitner, M., Leitner, T., Schmon, A., Aziz, K. & Pottlacher, G. Thermophysical Properties of Liquid Aluminum. *Metall. Mater. Trans. A* **48**, 3036–3045 (2017).

93. Miller, D. C. *et al.* Thermo-mechanical properties of alumina films created using the atomic layer deposition technique. *Sensors Actuators, A Phys.* **164**, 58–67 (2010).

94. Storaska, G. A. & Howe, J. M. In-situ transmission electron microscopy investigation of surface-oxide, stress-relief mechanisms during melting of sub-micrometer Al-Si alloy particles. *Mater. Sci. Eng. A* **368**, 183–190 (2004).

95. Mavrič, A., Valant, M., Cui, C. & Wang, Z. M. Advanced applications of amorphous alumina: From nano to bulk. *J. Non. Cryst. Solids* **521**, 119493 (2019).

96. Yang, Y., Kushima, A., Han, W., Xin, H. & Li, J. Liquid-Like, Self-Healing Aluminum Oxide during Deformation at Room Temperature. *Nano Lett.* **18**, 2492–2497 (2018).

97. Ksiazek, M., Sobczak, N., Mikulowski, B., Radziwill, W. & Surowiak, I. Wetting and bonding strength in Al/Al2O3 system. *Mater. Sci. Eng. A* **324**, 162–167 (2002).

98. Klinter, A. J., Mendoza-Suarez, G. & Drew, R. A. L. Wetting of pure aluminum and selected alloys on polycrystalline alumina and sapphire. *Mater. Sci. Eng. A* **495**, 147–152 (2008).

99. Coker, E. N. The oxidation of aluminum at high temperature studied by Thermogravimetric Analysis and Differential Scanning Calorimetry. *Sandia Rep. Sandia*

Natl. Lab. 1–22 (2013).

100. Hutchinson, J. W. Buckling of spherical shells revisited. *Proc. R. Soc. A Math. Phys. Eng. Sci.* **472**, (2016).

101. Timoshenko, S. P. & Gere, J. M. *Theory of Elastic Stability*. (McGraw Hill, New York, 1961).

102. Hidnert, P. Thermal expansion of aluminum and various important aluminum alloys. *Sci. Pap. Bur. Stand.* **19**, 697 (1924).

103. Hutchinson, C. ., Fan, X., Pennycook, S. . & Shiflet, G. . On the origin of the high coarsening resistance of Ω plates in Al–Cu–Mg–Ag Alloys. *Acta Mater.* **49**, 2827–2841 (2001).

104. Błachut, J. Experimental perspective on the buckling of pressure vessel components. *Appl. Mech. Rev.* **66**, 30–33 (2014).

105. Vliegenthart, G. A. & Gompper, G. Compression, crumpling and collapse of spherical shells and capsules. *New J. Phys.* **13**, (2011).

106. Yu, Q. *et al.* Thermo-mechanical analysis of microcapsules containing phase change materials for cold storage. *Appl. Energy* **211**, 1190–1202 (2018).

107. Li, P., Petrinic, N. & Siviour, C. R. Finite element modelling of the mechanism of deformation and failure in metallic thin-walled hollow spheres under dynamic compression. *Mech. Mater.* **54**, 43–54 (2012).

108. Montross, C. S., Wei, T., Ye, L., Clark, G. & Mai, Y. W. Laser shock processing and its effects on microstructure and properties of metal alloys: A review. *Int. J. Fatigue* **24**, 1021–1036 (2002).

109. Qiu, C. *et al.* On the role of melt flow into the surface structure and porosity development during selective laser melting. *Acta Mater.* **96**, 72–79 (2015).

110. Niu, H. J. & Chang, I. T. H. Selective laser sintering of gas atomized M2 high speed steel powder. *J. Mater. Sci.* **35**, 31–38 (2000).

111. Vock, S., Klöden, B., Kirchner, A., Weißgärber, T. & Kieback, B. Powders for powder bed fusion: a review. *Prog. Addit. Manuf.* **4**, 383–397 (2019).

112. Anderson, I. E., White, E. M. H. H. & Dehoff, R. *Feedstock powder processing research needs for additive manufacturing development*. vol. 22 (Elsevier Ltd, 2018).

113. Krakhmalev, P., Yadroitsev, I., Yadroitsava, I. & de Smidt, O. Functionalization of biomedical Ti6Al4V via in situ alloying by Cu during laser powder bed fusion manufacturing. *Materials (Basel).* **10**, (2017).

114. Hanemann, T., Carter, L. N., Habschied, M. & Adkins, N. J. E. In-situ alloying of AlSi10Mg + Si using Selective Laser Melting to control the Coe ffi cient of Thermal Expansion. *J. Alloys Compd.* **795**, 8–18 (2019).

115. Montero Sistiaga, M. L. *et al.* Changing the alloy composition of Al7075 for better processability by selective laser melting. *J. Mater. Process. Technol.* **238**, 437–445 (2016).

116. Wang, P. *et al.* Microstructure and mechanical properties of Al-Cu alloys fabricated by selective laser melting of powder mixtures. *J. Alloys Compd.* **735**, 2263–2266 (2018).

117. Oh, S. H., Kauffmann, Y., Scheu, C., Kaplan, W. D. & Rühle, M. Ordered Liquid Aluminum at the Interface with Sapphire. *Science (80-.).* **310**, (2005).

118. Aversa, A. *et al.* New aluminum alloys specifically designed for laser powder bed fusion: A review. *Materials (Basel).* **12**, (2019).

119. Zhang, J., Song, B., Wei, Q., Bourell, D. & Shi, Y. A review of selective laser melting of aluminum alloys: Processing, microstructure, property and developing trends. *J. Mater. Sci. Technol.* **35**, 270–284 (2019).

120. Geng, K., Yang, Y., Li, S., Misra, R. D. K. & Zhu, Q. Enabling high-performance 3D printing of Al powder by decorating with high laser absorbing Co phase. *Addit. Manuf.* **32**, 101012 (2020).

121. Mosallanejad, M. H., Niroumand, B., Aversa, A. & Saboori, A. In-Situ Alloying in Laser-Based Additive Manufacturing Processes: A Critical Review. *J. Alloys Compd.* **872**, 159567 (2021).

122. Roberts, C. E., Bourell, D., Watt, T. & Cohen, J. A novel processing approach for additive manufacturing of commercial aluminum alloys. *Phys. Procedia* **83**, 909–917 (2016).

123. Yan, Z., Wilkinson, S. K., Stitt, E. H. & Marigo, M. Investigating mixing and segregation using discrete element modelling (DEM) in the Freeman FT4 rheometer. *Int. J. Pharm.* **513**, 38–48 (2016).

124. Schwedes, J. Review on testers for measuring flow properties of bulk solids. *Granul. Matter* **5**, 1–43 (2003).

125. Schmid, M., Amado, F., Levy, G. & Wegener, K. Flowability of Powders for Selective Laser Sintering (SLS) investigated by Round Robin Test. *ETH Zurich Conf. Pap.* (2014).

126. Lee, N. & Cahoon, J. Interdiffusion of copper and iron in liquid aluminum. *J. Phase Equilibria Diffus.* **32**, 226–234 (2011).

127. Lei, Q. *et al.* Structural refinement and nanomechanical response of laser remelted Al-Al2Cu lamellar eutectic. *Mater. Sci. Eng. A* **706**, 115–125 (2017).

128. Scharowsky, T., Osmanlic, F., Singer, R. F. & Körner, C. Melt pool dynamics during selective electron beam melting. *Appl. Phys. A Mater. Sci. Process.* **114**, 1303–1307 (2014).

129. Mazzoleni, L., Demir, A. G., Caprio, L., Pacher, M. & Previtali, B. Real-Time Observation of Melt Pool in Selective Laser Melting: Spatial, Temporal, and Wavelength Resolution Criteria. *IEEE Trans. Instrum. Meas.* **69**, 1179–1190 (2020).

130. Zhao, C. *et al.* Real-time monitoring of laser powder bed fusion process using high-speed X-ray imaging and diffraction. *Sci. Rep.* **7**, 1–11 (2017).

131. Gremaud, M., Carrard, M. & Kurz, W. Banding phenomena in AlFe alloys subjected to laser surface treatment. *Acta Metall. Mater.* **39**, 1431–1443 (1991).

132. Plotkowski, A. *et al.* Evaluation of an Al-Ce alloy for laser additive manufacturing. *Acta Mater.* **126**, 507–519 (2017).

133. Mohammadpour, P. & Phillion, A. B. Solidification microstructure selection maps for laser powder bed fusion of multicomponent alloys. *IOP Conf. Ser. Mater. Sci. Eng.* **861**, (2020).

134. Gill, S. C. & Kurz, W. Laser rapid solidification of AlCu alloys: banded and plane front growth. *Mater. Sci. Eng. A* **173**, 335–338 (1993).

135. Maraşlı, N. & Bayram, Ü. Investigations of Electrical Resistivity and Thermal Conductivity Dependences on Growth Rate in the Al–Cu–Ti Eutectic Alloy. *Int. J. Thermophys.* **42**, 1–19 (2021).

136. Bayram, Ü. & Maraşlı, N. Thermal conductivity and electrical resistivity dependences on growth rate in the directionally solidified Al–Cu–Ni eutectic alloy. *J. Alloys Compd.* **753**, 695–702 (2018).

137. Sullivan, E. J. *et al.* Lamellar instabilities during scanning laser melting of Al–Cu eutectic and hypoeutectic thin films. *J. Alloys Compd.* **865**, 158800 (2021).

138. Anthony, T. R. & Cline, H. E. Surface rippling induced by surface-tension gradients during laser surface melting and alloying. *J. Appl. Phys.* **48**, 3888–3894 (1977).

139. Wei, P. S., Chen, Y. H., Ku, J. S. & Ho, C. Y. Active solute effects on surface ripples in electron-beam welding solidification. *Metall. Mater. Trans. B Process Metall. Mater. Process. Sci.* **34**, 421–432 (2003).

140. Volkov, A. N. & Zhigilei, L. V. Melt dynamics and melt-through time in continuous wave laser heating of metal films: Contributions of the recoil vapor pressure and Marangoni effects. *Int. J. Heat Mass Transf.* **112**, 300–317 (2017).

141. Otto, H.-J. *et al.* Temporal dynamics of mode instabilities in high-power fiber lasers and

amplifiers. *Opt. Express* **20**, 15710 (2012).

142. Rödler, G. *et al.* Additive manufacturing of high-strength eutectic aluminium-nickel alloys – Processing and mechanical properties. *J. Mater. Process. Technol.* **298**, (2021).

143. Gussone, J. *et al.* Ultrafine eutectic Ti-Fe-based alloys processed by additive manufacturing – A new candidate for high temperature applications. *Appl. Mater. Today* **20**, 1–11 (2020).

144. Lorusso, M., Trevisan, F., Calignano, F., Lombardi, M. & Manfredi, D. A357 alloy by lpbf for industry applications. *Materials (Basel).* **13**, 1–12 (2020).

145. Kakitani, R., Reyes, R. V., Garcia, A., Spinelli, J. E. & Cheung, N. Relationship between spacing of eutectic colonies and tensile properties of transient directionally solidified Al-Ni eutectic alloy. *J. Alloys Compd.* **733**, 59–68 (2018).

146. Plapp, M. & Karma, A. Eutectic colony formation: A phase-field study. *Phys. Rev. E - Stat. Physics, Plasmas, Fluids, Relat. Interdiscip. Top.* **66**, 17 (2002).

147. Xiong, Z. H. *et al.* Role of melt pool boundary condition in determining the mechanical properties of selective laser melting AlSi10Mg alloy. *Mater. Sci. Eng. A* **740**–**741**, 148–156 (2019).

148. Cahn, J. W., Hillig, W. B. & Sears, G. W. The molecular mechanism of solidification. *Acta Metall.* **12**, 1421–1439 (1964).

149. Jackson, K. A. Mechanism of Growth. *Liq. Met. Solid A.S.M.* 174–186 (1958).

150. Starr, T. L., Rafi, K., Stucker, B. & Scherzer, C. M. Controlling phase composition in selective laser melted stainless steels. *Proc. Solid Free. Fabr. Symp* 439–446 (2012).

151. Song, B. *et al.* Differences in microstructure and properties between selective laser melting and traditional manufacturing for fabrication of metal parts : A review. *Front. Mech. Eng.* **10**, 111–125 (2015).

152. Jadhav, S. D. *et al.* Influence of selective laser melting process parameters on texture evolution in pure copper. *J. Mater. Process. Technol.* **270**, 47–58 (2019).

153. Arabi-Hashemi, A. *et al.* 3D magnetic patterning in additive manufacturing via site-specific in-situ alloy modification. *Appl. Mater. Today* **18**, 100512 (2020).

154. Krakhmalev, P. *et al.* Microstructure, solidification texture, and thermal stability of 316 L stainless steel manufactured by laser powder bed fusion. *Metals (Basel).* **8**, (2018).

155. Yadroitsev, I., Krakhmalev, P. & Yadroitsava, I. Hierarchical design principles of selective laser melting for high quality metallic objects. *Addit. Manuf.* **7**, 45–56 (2015).

156. Velasco-Hogan, A., Xu, J. & Meyers, M. A. Additive Manufacturing as a Method to Design and Optimize Bioinspired Structures. *Adv. Mater.* **30**, (2018).

157. Gu, G. X., Takaffoli, M. & Buehler, M. J. Hierarchically Enhanced Impact Resistance of Bioinspired Composites. *Adv. Mater.* **29**, 1–7 (2017).

158. Fratzl, P. Biomimetic materials research: What can we really learn from nature's structural materials? *J. R. Soc. Interface* **4**, 637–642 (2007).

159. du Plessis, A. *et al.* Beautiful and Functional: A Review of Biomimetic Design in Additive Manufacturing. *Addit. Manuf.* **27**, 408–427 (2019).

160. Sutcliffe, C. *et al.* The rapid manufacture of micro hierarchical structures by selective laser melting. 2102 (2005) doi:10.2351/1.5060471.

161. Lejček, P. *et al.* Selective laser melting of pure iron: Multiscale characterization of hierarchical microstructure. *Mater. Charact.* **154**, 222–232 (2019).

162. Gong, H., Christiansen, D., Beuth, J. & Lewandowski, J. J. Melt Pool Characterization for Selective Laser Melting of Ti-6Al-4V Pre-alloyed Powder. *Solid Free. Fabr. Symp.* 256–267 (2014).

163. Kraft, R. W. & Albright, D. L. Microstructure of Unidirectionally Solidified Al-CuAl2 Eutectic. *Trans. Metall. Soc. AIME* **221**, 95-102q (1961).

164. Kraft, R. W. Controlled Eutectics. *J. Met.* **18**, 192–200 (1966).

165. Chadwick, G. A. Solidifcation of CuAl2-Al Eutectic Alloys. *J. Inst. Met.* **91**, 169–173 (1963).

166. Wang, T., Zhu, Y. Y., Zhang, S. Q., Tang, H. B. & Wang, H. M. Grain morphology evolution behavior of titanium alloy components during laser melting deposition additive manufacturing. *J. Alloys Compd.* **632**, 505–513 (2015).

167. Products, M. *et al.* Standard Specification for Aluminum and Aluminum-Alloy Sheet and Plate 1. doi:10.1520/B0209.

168. Liu, S. *et al.* Strengthening mechanism and micropillar analysis of high-strength NiTi–Nb eutectic-type alloy prepared by laser powder bed fusion. *Compos. Part B Eng.* **200**, 108358 (2020).

169. Gokcekaya, O. *et al.* Unique crystallographic texture formation in Inconel 718 by laser powder bed fusion and its effect on mechanical anisotropy. *Acta Mater.* **212**, 116876 (2021).

170. Van Cauwenbergh, P. *et al.* Unravelling the multi-scale structure–property relationship of laser powder bed fusion processed and heat-treated AlSi10Mg. *Sci. Rep.* **11**, 1–15 (2021).

171. Mehta, A. *et al.* Additive manufacturing and mechanical properties of the dense and crack free Zr-modified aluminum alloy 6061 fabricated by the laser-powder bed fusion. *Addit. Manuf.* **41**, 101966 (2021).

172. Kulkarni, A. A. *et al.* Template-Directed Solidification of Eutectic Optical Materials. *Adv. Opt. Mater.* **6**, 1–20 (2018).

173. Callister, W. D. *Materials Science and Engineering An Introduction*. (John Wiley & Sons, 2007).

174. Niendorf, T. & Brenne, F. Lattice Structures Manufactured by SLM : On the Effect of Geometrical Dimensions on Microstructure Evolution During Processing. *Metall. Mater. Trans. B* **45**, 1181–1185 (2014).

175. Yadroitsava, I. *et al.* Bone Regeneration on Impants of Titanium Alloys Produced by Laser Powder Bed Fusion: A Review. in *Titanium for Consumer Applications* (Elseviewr, 2019). doi:10.13140/RG.2.2.36780.72328.

176. Osakada, K. & Shiomi, M. Flexible manufacturing of metallic products by selective laser melting of powder. *Int. J. Mach. Tools Manuf.* **46**, 1188–1193 (2006).

177. Thijs, L., Kempen, K., Kruth, J. P. & Van Humbeeck, J. Fine-structured aluminium products with controllable texture by selective laser melting of pre-alloyed AlSi10Mg powder. *Acta Mater.* **61**, 1809–1819 (2013).

178. Thijs, L. *et al.* Strong morphological and crystallographic texture and resulting yield strength anisotropy in selective laser melted tantalum. *Acta Mater.* **61**, 4657–4668 (2013).

179. Croker, M. N., Baragar, D. & Smith, R. W. Anomalous eutectic growth: II. The relationship between faceted/non-faceted eutectic structures. *J. Cryst. Growth* **30**, 198–212 (1975).

180. Hecht, U., Eiken, J., Akamatsu, S. & Bottin-Rousseau, S. Phase boundary anisotropy and its effects on the maze-to-lamellar transition in a directionally solidified Al–Al 2 Cu eutectic. *Acta Mater.* **170**, 268–277 (2019).

181. Wang, S. J., Liu, G., Wang, J. & Misra, A. Characteristic orientation relationships in nanoscale Al-Al 2 Cu Eutectic. *Mater. Charact.* **142**, 170–178 (2018).

182. Zhou, L. *et al.* Laser powder bed fusion of Al–10 wt% Ce alloys: microstructure and tensile property. *J. Mater. Sci.* **55**, 14611–14625 (2020).

183. Lin, X. *et al.* Regular eutectic and anomalous eutectic growth behavior in laser remelting of Ni-30wt%Sn alloys. *Acta Mater.* **126**, 210–220 (2017).

184. Zhang, F. *et al.* A Transition from Fine to Coarse Lamellar Eutectics in the Undercooled Ni-29.8 At. Pct Si Eutectic Alloy: Experiments and Modeling. *Metall. Mater. Trans. A*

Phys. Metall. Mater. Sci. **50**, 2847–2859 (2019).

185. Dake, J. M. *et al.* Direct observation of grain rotations during coarsening of a semisolid Al – Cu alloy. *Proc. Natl. Acad. Sci.* **113**, 5998–6006 (2016).

186. Park, J., Kang, J. & Oh, C. Phase-field simulations and microstructural analysis of epitaxial growth during rapid solidification of additively manufactured AlSi10Mg alloy. *Mater. Des.* **195**, 108985 (2020).

187. Liotti, E. *et al.* The spatial and temporal distribution of dendrite fragmentation in solidifying Al-Cu alloys under different conditions. *Acta Mater.* **121**, 384–395 (2016).

188. Wesner, E., Choudhury, A., August, A., Berghoff, M. & Nestler, B. A phase-field study of large-scale dendrite fragmentation in Al-Cu. *J. Cryst. Growth* **359**, 107–121 (2012).

189. Elliott, R. *Eutectic solidification processing: crystalline and glassy alloys.* (Elsevier, 2013).

190. Barthelat, F., Rim, J. E. & Espinosa, H. D. A Review on the Structure and Mechanical Properties of Mollusk Shells – Perspectives on Synthetic Biomimetic Materials. *Appl. Scanning Probe Methods XIII* 17–44 (2009) doi:10.1007/978-3-540-85049-6.

Appendix 1: TEM characterization eutectic lamellae and colony boundary

Relevant TEM work has been included here that may be beneficial to future research in this area. A FIB lift out was made from an LPBF processed Al-Cu single track wall (shown previously in **Figure 4-4**) so that a transverse cross-section of several colonies was made. TEM was then performed on the sample to better characterize the lamellae and the colony boundaries. The FIB lift out is shown in **Figure A1- 1** and apparent colonies are labeled 1-8 for reference purposes.

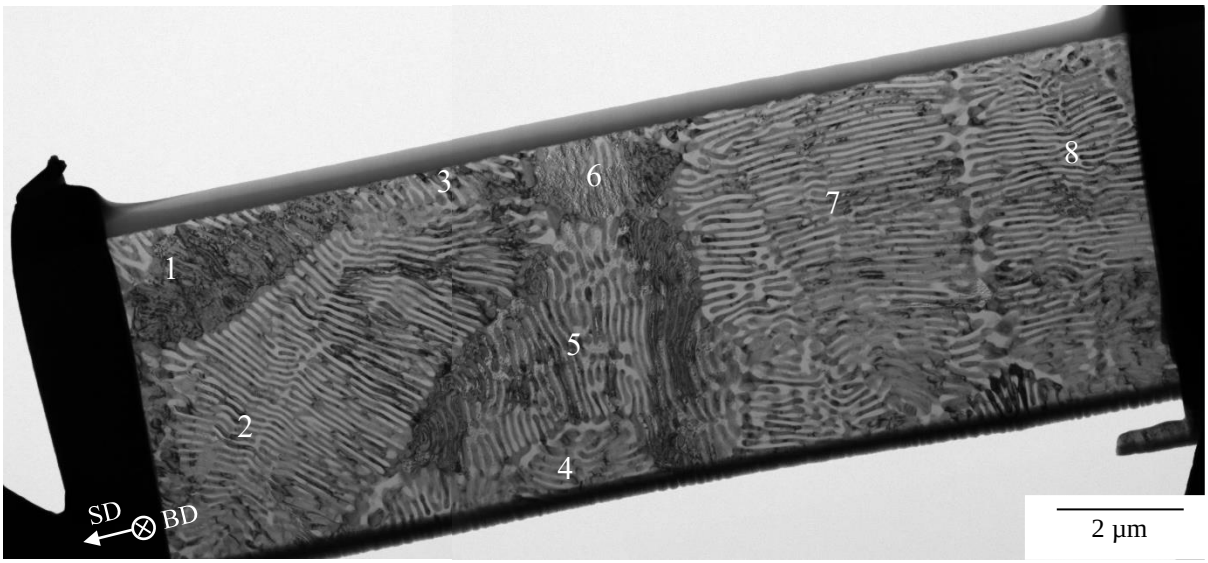

Figure A1- 1: TEM micrograph of FIB lift out (**Figure 4-4**) showing transverse cross-section of eutectic colonies formed in an LPBF processed Al-Cu single track wall sample. What appear to be distinct colonies have been labeled 1-8.

The boundaries between colonies are difficult to distinguish, especially between colonies that have similarly oriented lamellae. **Figure A1- 2a** shows a magnified micrograph of colonies 1 and 2, where the lamellae in both colonies are oriented in the same direction and even appear to be continuous across the boundary in some places. Focusing on the lamellae in colony 2, selected

area diffraction (SAD) was used to obtain a diffraction pattern of the two phase crystal. From this diffraction pattern shown in **Figure A1- 2d** a polycrystalline pattern was observed (white arrow). Dirty dark-field was performed by putting a selected area aperture (SAA) over a portion of the ring (red circle) and the resulting image showed the poly crystalline diffraction was coming from the θ-phase lamellae. The dark-field micrograph is shown in **Figure A1- 2e**.

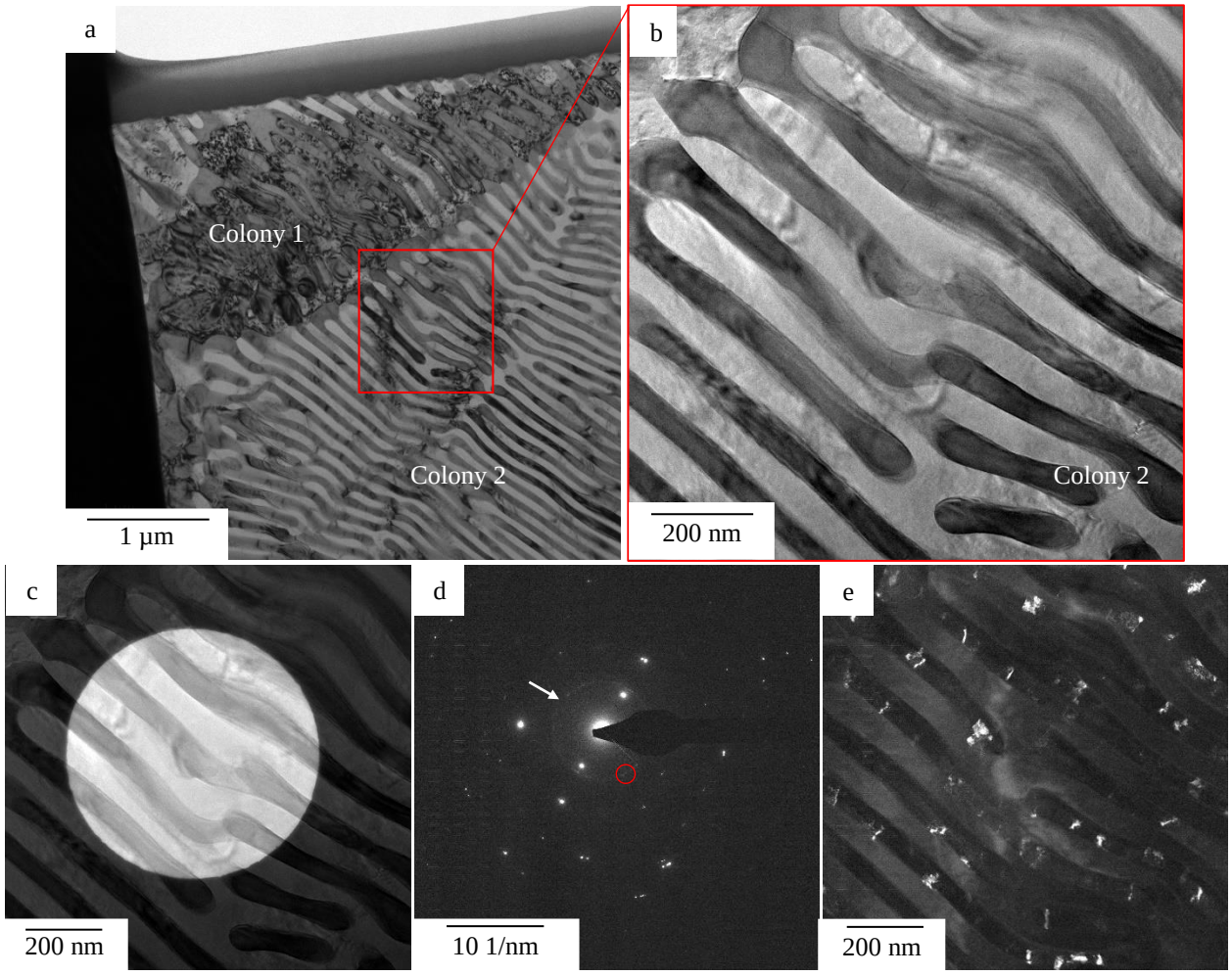

Figure A1- 2: Bright field micrograph of coloniess 1 and 2 (a), and the lamellae in colony 2 (b). SAD was taken of within colony 2 using a 40 µm SAA (c). The resulting diffraction pattern showed a polycrystalline ring (white arrow) within the two phase crystal (d). Dirty dark-field was performed by placing the aperture over the polycrystalline diffraction pattern (red circle in d), which showed highlighted regions within the θ-phase (e).

The sources of these polycrystalline regions within the θ-phase lamellae is unknown as the d-spacing of low index planes for both the FCC α-phase and the tetragonal θ-phase do not appear to match the diffraction pattern. Tilting of the sample was performed to see if the polycrystalline regions would shift, indicating that they may be crystal defects. A bright-field micrograph and corresponding dirty dark-field micrographs at two different β-tilt angles are shown in **Figure A1- 3**.Two highlighted regions in the θ-phase lamellae are marked (red circles) in the first tilt orientation, and shown again in the second. Although the sample moved during tilting, these regions within the θ-phase lamellae did not appear to move much. It should be noted that it was previously shown that low concentrations of Si were present within the sample, and that this tertiary element was found to segregate to the θ-phase lamellae (**Figure 4-5**). Although the d-spacing of Si crystal indices do not match the diffraction pattern from the sample, the presence of Si may still contribute to this polycrystalline region by possibly forming an intermetallic with the θ-phase. Yet, according to tertiary phase diagrams of Al-Cu-Si, Si is soluble in the θ-phase at low concentrations, and thus should not produce an intermetallic unless it is a metastable phase.

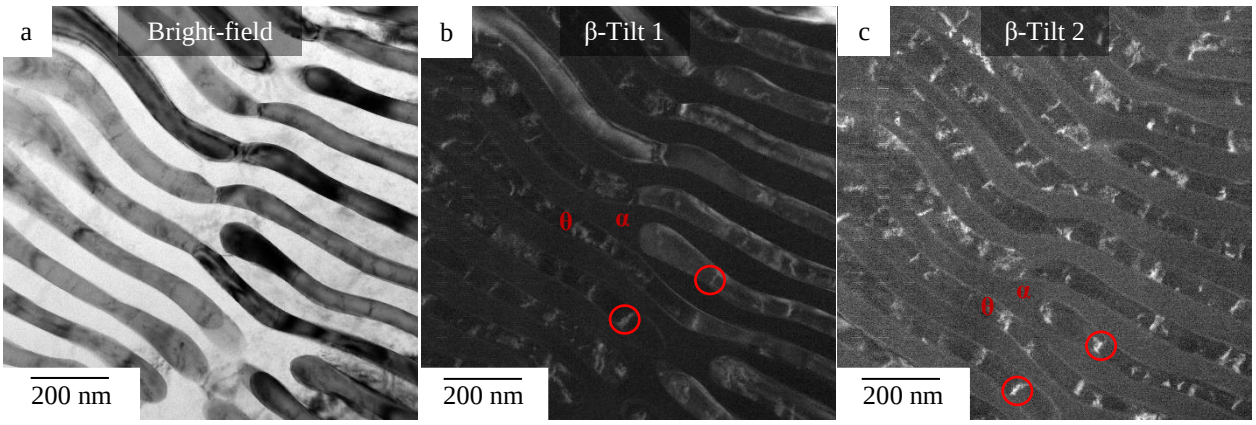

Figure A1- 3: Bright-field micrograph of colony 2 (a) and corresponding dirty dark-field micrographs at two different tilts (a&b). The highlighted polycrystalline regions in the θ-phase lamellae (red circles) do not shift.

A simpler explanation may be that the Si in the θ-phase is causing a lattice strain which is why the d-spacing does not match the Bragg spots in the polycrystalline region. The [112] plane of the θ-phase is the closest fit, but suggests that there is approximately a 4% strain within the lattice. The reason why the θ-phase would have fine sub grains within the lamellae is unknown, although it may be correlated to shifts in the direction of the lamellae, where the sub grains allow for the crystal to maintain its preferred growth direction.

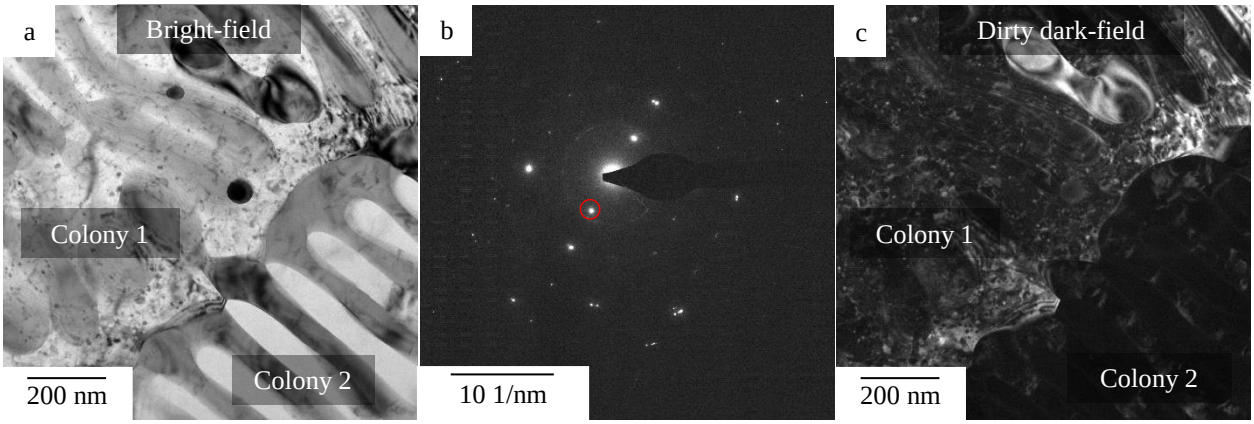

Figure A1- 4: Bright-field micrograph of region between two colonies (a) SAD pattern was obtained from the region (b) and SAA was placed over one of the Bragg spots (red circle). Corresponding dark-field micrograph clearly shows where colony boundary is located.

Dirty dark field was again used to determine the colony boundaries of this sample by first taking an SAD pattern of an area between two colonies, and then using an SAA to select a diffraction point of one of the known phases. An example of this is shown **Figure A1- 4** where the diffraction point of the α-phase was selected and the corresponding α lamellae is highlighted, clearly showing the boundary between colonies. Small highlighted regions can be observed in the θ-phase in colony 2, but in both phases in colony 1 (**Figure A1- 4c**) due to the inclusion of the polycrystalline diffraction ring with the Al (FCC) Bragg spot within the SAA (**Figure A1- 4b**, red circle).

In conclusion, these results suggest that small polycrystalline regions form within the lamellae due to either an impurity element within the alloy or due to the fast solidification velocities at which the microstructure formed. Previous STEM-EDS results showed that Si is present within the θ-phase, yet the d-spacing of pure Si does not match with the Bragg spots on the diffraction pattern. Equilibrium ternary phase diagrams suggest that Si can be soluble within the θ-phase up to a few weight percent, which may explain the 4% strain observed between the [112] plane of the θ-phase and the polycrystalline ring on the diffraction pattern. Further analysis of this or similarly processed samples may yield a more complete explanation to this observation, and provide a better understanding of how this microstructure forms during fast solidification velocities.

It is the Glory of God to give all things to us in the best of all possible manners. To study things therefore under the double notion of interest and treasure, is to study all things in the best of all possible manners. Because in studying so we enquire after God's Glory, and our own happiness. And indeed enter into the way that leadeth to all contentments, joys, and satisfactions, to all praises, triumphs and thanksgivings, to all virtues, beauties, adorations and graces, to all dominion, exaltation, wisdom, and glory, to all holiness, Union, and Communication with God, to all patience, and courage and blessedness, which it is impossible to meet any other way. So that to study objects for ostentation, vain knowledge or curiosity is fruitless impertinence, tho' God Himself and Angles be the object. But to study that which will oblige us to love Him, and feed us with nobility and goodness toward men, that is blessed and so is it to study that which will lead us to the Temple of Wisdom and seat us in the Throne of Glory.

-Thomas Traherne